CONTROL, STABILITY ANALYSIS AND GRID INTEGRATION OF WIND TURBINES

CHEN WANG

Supervised by Professor George Weiss

A thesis submitted to Imperial College London for the degree of

Doctor of Philosophy

Control & Power Research Group
Department of Electrical and Electronic Engineering
Imperial College London

March 2008

Statement of Originality

I hereby certify that the work presented in this thesis is my own work, and, where appropriate, contributions from other people whom have been acknowledged.

Chen Wang

15 March 2008, London

Abstract

In Chapters 2 and 3 of the thesis we propose a self-scheduled control method for a doubly-fed induction generator driven by a wind turbine (DFIGWT), whose rotor is connected to the power grid via two back-to-back PWM power converters. We design a controller for this system using the linear matrix inequality based approach to linear parameter varying (LPV) systems, which takes into account the nonlinear dynamics of the system. We propose a two-loop hierarchical control structure. The inner-loop current controller, which considers the synchronous speed and the generator rotor speed as a parameter vector, achieves robust tracking of the rotor current reference signals. The outer-loop electrical torque controller aims for wind energy capture maximization, grid frequency support and generates the reference rotor current. We perform a controller reduction for the inner-loop LPV controller, which is not doable by conventional model-reduction techniques, because the controller is parameter-dependent. In simulation, the reduced order controller has been tested on a nonlinear 4th order DFIG model with a two-mass model for the drive-train. Stability and high performances have been achieved over the entire operating range of the DFIGWT. More importantly, simulation results have demonstrated the capability and contribution of the proposed two-loop control systems to grid frequency support.

In Chapter 4 we investigate the integral input-to-state stability (iISS) property for passive nonlinear systems. We show that under mild assumptions, a passive nonlinear system which is globally asymptotically stable is also iISS. Moreover, the integral term from the definition of the iISS property has a very simple form (like an L^1 norm). These theoretical results will be useful for our stability analysis of wind turbine systems in Chapter 5.

In Chapter 5 we investigate the stability of a variable-speed wind turbine operating under low to medium wind speed. The turbine is controlled to capture as much wind energy as possible. We concentrate on the mechanical level of the turbine system, more

precisely on the drive-train with the standard quadratic generator torque controller. We consider both the one-mass and the two-mass models for the drive-train, with the inputs being the deviation of the active torque from an arbitrary positive nominal value and the tracking error of the generator torque. We show that the turbine system is input-to-state stable for the one-mass model and iISS for the two-mass model. Using our abstract results from Chapter 4, we identify the iISS gain of this system. We also propose an adaptive search algorithm for the optimal gain of the quadratic torque controller.

Acknowledgements

This thesis is a summary of my PhD research at Imperial College London, supervised by Professor George Weiss. I have been working on this project with Prof. Weiss since May 2004, when I was studying towards an MSc degree. Throughout my study at Imperial College, I have been learning from Prof. Weiss. As he once mentioned, PhD study is a kind of adventure, full of risks and uncertainties. Thanks to his inspiration and guidance, this journey is fruitful and means very much to me. I experienced the joyfulness when our first paper was accepted for publication, then comes the second, the third, etc. I also experienced the dilemma when something we proposed was theoretically nice but might not necessarily work very well in practice. Most of the time, we were struggling with ideas or simulations and could not make progress for days. Looking back, I feel that although we have eventually worked out many questions in this project, in real life there are always more questions than answers. Here let me convey my gratefulness and best wishes to Prof. Weiss. Thank you!

Then I would like to thank Miss Xia Wang for her support throughout my study in the UK. You have been extremely encouraging, especially since I began to think about future career. Do you remember those days when I was working at McD and struggling with life? Do you remember those times when I presented my papers in conferences and began to realize my strength and career ambition? You may forget last summer at LSE and this spring at FTC, but you would not forget the time we spent and the effort we made in pursuing a career in the UK, which I believe is life-changing.

I would like to thank Mr. Shaohua Tang, my old housemate and my “old brother”. You are my lighthouse, especially during those early days in the UK, when I felt confused and sometimes even depressed about the gap between education and career. Looking at your path to success, I can always feel the power of your philosophy of life.

My colleagues, Mr. Bayu Jayawardhana, Miss Xinxin Wang, Mr. Zhenhai Li, Ms. Chunmei Feng, etc. Thank you for your concerns on both my life and study in the UK. You are ones of those most talented and hard-working people I have ever met. Working with all of you at Imperial College is definitely a good memory.

In the end, to my beloved parents. You may not understand my PhD research, you could not imagine what I am doing everyday, you have not seen my face for the last three years, but I know from the bottom of my heart that you understand your son best. Your love and trust are my torches in darkness. Your smile is and will always be my biggest drive for success throughout my career!

To my parents

Contents

List of Figures

Chapter 1

Introduction

1.1 Backgrounds and motivations

Wind driven power generating units based on a doubly-fed induction generator (DFIG), as shown in Figure 1.1, have been widely recognized in industry as one of the most promising wind turbine configurations, especially for high power capacity off-shore wind farms. A large number of such wind farms are already in operation and more are planned or under construction (see [11] and [14]). The DFIG is a wound rotor asynchronous generator, whose stator is connected to the power grid (via a transformer). The rotor operates at a frequency depending on its speed, so that the power-flow between the rotor and the power grid must be channelled through back-to-back AC/DC and DC/AC converters. The rated power of the power converters defines the range of the variable speed (typically $\pm$ 30% around synchronous speed), see [8, 14, 21] and [42]. Control of the DFIG wind turbine (DFIGWT) is theoretically challenging for control engineers because the dynamical system, with a wide operating range, is highly nonlinear and the wind speed input is a rapidly changing random signal.

Linear parameter varying (LPV) systems are a special class of systems, which for every fixed value of the parameter vector $\theta(t) \in \mathbb{R}^s$ are linear time invariant (LTI) systems. We need to consider LPV systems where the state-space matrices depend on the vector of parameters $\theta(t)$ in an affine fashion. A state-space representation of an LPV system Σ is

$$\dot{x}(t) = \mathbf{A}(\theta(t))x(t) + \mathbf{B}(\theta(t))u(t), \tag{1.1.1}$$

$$y(t) = \mathbf{C}(\theta(t))x(t) + \mathbf{D}(\theta(t))u(t), \tag{1.1.2}$$

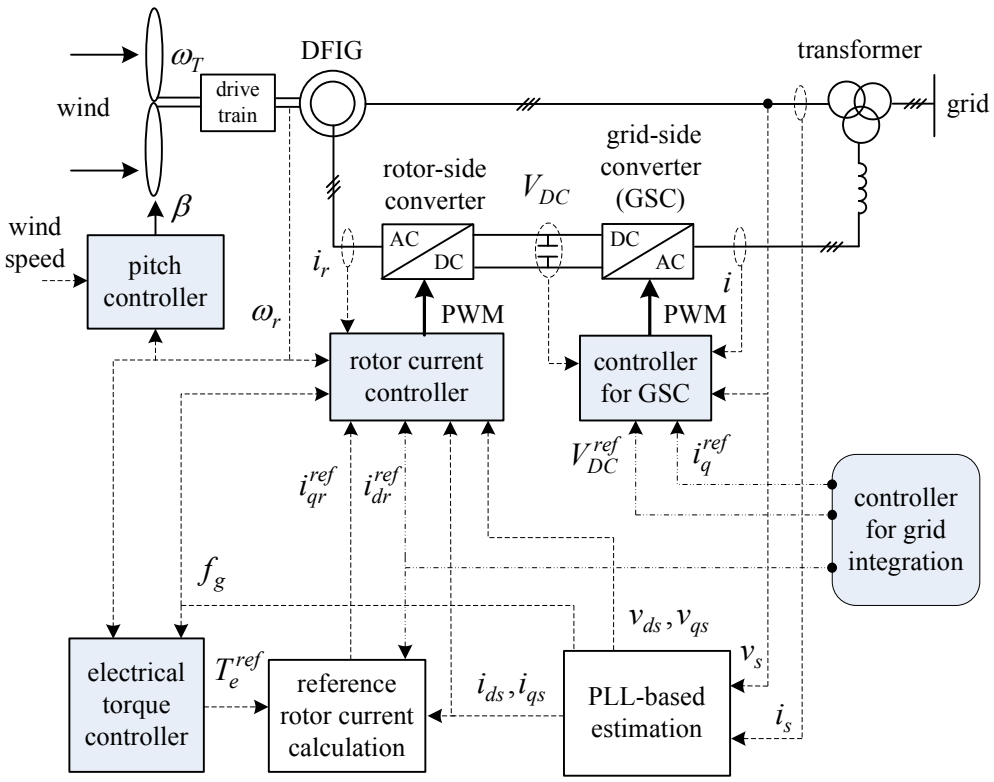

Figure 1.1: Control of a grid-connected wind driven DFIG with back-to-back converters for the rotor power. The block diagram used in the synthesis of the rotor current controller is shown in Figure 3.3. The block diagram of the electrical torque controller (which also does frequency support) is shown in Figure 3.1. The reference rotor current calculation is explained in Section 3.6.1. The phase-locked loop (PLL)-based estimation is shown in greater detail in Figure 3.5. The block labelled “controller for grid integration” controls the stator reactive power and the GSC reactive power.

where $x(t)$ is the state ($x(t) \in \mathbb{R}^n$), $u(t)$ is the input vector and $y(t)$ is the measured output vector. In this thesis, we only have to deal with LPV systems where measurements of $\theta(t)$ are available in real time. For LPV systems, a traditional control method is to design LTI controllers for several points θ, and then using an interpolation technique to obtain the control law over the entire operating range. The main drawback of this is a lack of high performance, of robustness, even of stability [7]. In the framework of LPV systems proposed by Apkarian *et al.* [4], Apkarian *et al.* [5] and Gahinet *et al.* [15], the controller synthesis problem is formulated as a convex optimization problem. After solving some linear matrix inequality (LMI) constraints, the so-called self-scheduled LPV controller is given by a simple linear interpolation and then stability and certain performance bounds are guaranteed along all possible trajectories of θ. A self-scheduled LPV controller can update itself online using parameter measurements, so that the changing plant dynamics are taken into account.

In Chapter 3, based on LPV control technique, we design an inner-loop current controller for the DFIG, which achieves robust tracking of reference rotor currents. We take both the synchronous speed and the generator rotor speed into the parameter vector to conduct the LPV design. This is doable in practice, as the measurement of the generator rotor speed can be obtained from a slower outer mechanical loop, while the measurement of the synchronous speed is available using a PLL-based estimation (see Figure 1.1). A good application of the LPV technique to the control of an induction motor can be found in [44].

The synthesized LPV controller has at least the same order as the plant and may have some unnecessary fast modes, which would complicate the hardware implementation [7]. Controller reduction for general LPV systems is an active research area, see Jaimoukha *et al.* [27]. We propose a crude controller reduction procedure for self-scheduled LPV controllers. Fast modes are truncated so that the reduced order controller is easy to implement on a digital signal processor (DSP).

In most countries, the nominal grid frequency is 50Hz. If the instantaneous demand is higher than the generation, the system frequency will fall. Conversely, if the instantaneous demand is lower than the generation, the frequency will rise. Under exceptional

circumstances, the system frequency can rise to 52Hz and fall as low as 47.0Hz. There are two main causes for the frequency drop: $i)$ loss of generation; $ii)$ increase in demand, for example due to cold or hot weather. The active power output from a generator needs to be controlled in response to the above situations, so that the grid frequency can be maintained within $\pm$ 0.5Hz around 50Hz (see [1]).

In the event of frequency drop, with traditional generation, the increase in the active power output of the generators is achieved through governor control. As the penetration of wind power in the electricity grid continues to increase in many countries, wind farms could potentially contribute to the frequency support, see Hughes $et\ al.$ [26], Hansen $et\ al.$ [22] and Morren $et\ al.$ [38]. Motivated by this new control task for wind turbines to provide grid support, in this thesis we design a novel frequency support controller, which is embedded in the electrical torque controller (see Figure 1.1 and see also our recent paper [58]). We take both the synchronous speed and the generator rotor speed into the parameter vector to improve the LPV design for the DFIG, so that the grid frequency variation is taken into account, and more importantly, the stability of the DFIG is guaranteed over the entire operating range of the wind turbine system.

The stability analysis of variable-speed wind turbines is another challenging task for control engineers because the dynamical system, with a wide operating range, is essentially nonlinear and the active torque (which depends on the wind speed as well as the turbine speed and the pitch angle) is a random signal. The turbine system has hierarchical control levels, see Figure 1.1. On the highest level (not shown in Figure 1.1), the supervisory control system decides when the turbine should start up and whether it should operate in region 2 (optimizing power capture under moderate wind speed) or in region 3 (maintaining constant power under high wind speed). The middle (mechanical) level control systems are responsible for generator torque control, pitch control and yaw control (the latter is not shown in Figure 1.1). The lowest (electrical) control level is in charge of rotor current control and DC-link voltage control, and this level is the fastest, see Johnson, Pao, Balas and Fingersh [31]. It is reasonable to assume that the generator with a good rotor current control system responds rapidly and accurately when tracking the reference torque produced by the torque controller. Then, the stability analysis of the mechanical

level does not depend on the details of the rotor current control. In this thesis, we focus on the stability analysis of the drive-train with the inputs being the deviation of the active torque from an arbitrary positive nominal value and the tracking error of the generator torque (see the main results in Chapter 5).

The stability analysis of the drive-train with the quadratic torque control law has been the main topic of the paper [31]. Our research (see our recent paper [57]) could be regarded as a continuation of their work. We consider the more accurate two-mass model for the drive-train, and we consider global asymptotic stability (GAS) as well as the relatively recent concepts known as input-to-state stability (ISS) and integral input-to-state stability (iISS). For the interpretation and importance of ISS and iISS, please refer to [3, 51].

By extracting and generalizing the abstract idea in the direct proof of [57], we investigate the iISS property for a broad class of passive nonlinear systems (see our recent paper [56]). Stability analysis often involves a big effort to search for a Lyapunov function. Our main result is meant to eliminate the need for finding a Lyapunov function satisfying the condition (4.1.3) (see Chapter 4), for passive systems. By combining our result with a recent result in Jayawardhana, Teel and Ryan [29], we can actually prove that under mild technical assumptions, a passive and GAS system satisfies the iISS type estimate with a very simple (L^1 norm type) integral term. We will illustrate the result by proving the iISS property (with a simple integral term) for the drive-train of a wind turbine, in Chapter 5.

In order for a variable speed wind turbine to maximize wind energy capture, the turbine aerodynamics need to be well known (see Subsection 2.3). Many control methods have been proposed to maximize the energy production in the presence of turbine uncertainties (see [6, 31, 35, 48]). We shall describe in Section 5.4 a simple adaptive algorithm that updates the gain of the quadratic torque control law. No prior knowledge of the turbine aerodynamics is required. This adaptive algorithm may be regarded as an alternative to the one proposed in [31]. The simulation results in Section 5.5 show that this adaptive algorithm together with the quadratic control law lead to a high efficiency in capturing the available wind power.

1.2 Contributions of the thesis

We mention below the contributions of the thesis which have been submitted as articles in journals or presented in conferences.

- We propose a self-scheduled control method for a DFIGWT, using the LMI based approach to LPV systems. We perform a controller reduction for the LPV controller, which is not doable by conventional model-reduction techniques, see [58, 60].

- We design a novel frequency support controller, which is embedded in the electrical torque controller. The electrical torque controller is capable of both wind energy capture maximization and primary grid frequency support, see [60].

- We investigate the iISS property for passive nonlinear systems. We show that under mild assumptions, a passive nonlinear system which is globally asymptotically stable is also iISS. Moreover, the integral term from the definition of the iISS property has a very simple form (like an L^1 norm). These theoretical results will be useful for our analysis of wind turbine systems, see [56, 59, 57, 61].

1.3 Structure of the thesis

Throughout the thesis, we assume that the readers have some basic understanding on vector control, robust control and stability for nonlinear systems.

Chapter 2 describes the wind turbine systems, which include wind speed characteristics, wind turbine aerodynamics and control strategies, generator modelling, drive-train dynamics and converter modelling. A brief introduction to the vector control of converters using PI control technique is also given.

In Chapter 3, we propose a two-loop control strategy for a DFIGWT using LPV techniques. We perform a controller reduction procedure for the inner loop LPV controller. We also propose a novel frequency support controller which can be embedded in the outer-loop electrical torque controller.

In Chapter 4, we investigate the iISS property for passive nonlinear systems. We show that under mild assumptions, a passive nonlinear system which is GAS is also iISS. Moreover, the integral term from the definition of the iISS property has a very simple form (like an L^1 norm).

In Chapter 5, we investigate the stability of the drive-train of a variable-speed wind turbine with quadratic torque control. The wind turbine is operating under low to medium wind speed. We show that the turbine system is ISS for the one-mass drive-train model and iISS for the two-mass drive-train model. Using our abstract results from Chapter 4, we identify the iISS gain of this system. In the end, we propose an adaptive search algorithm for the optimal gain of the quadratic torque controller.

Chapter 2

Wind turbine systems

2.1 Wind properties

The wind is movement of air masses with different speeds in all the regions of the atmosphere. These movements are very difficult to characterize due to the highly variable behavior both geographically and in time. This means that this variability persists over a very wide range of scales in time. On a long-term scale, days and hours, the wind will vary from site to site mostly dependent on the general climate and the physical geography of the region. Locally, the short-time behavior of the wind is affected by the surface conditions at the ground, such as trees, buildings, areas of water, etc. Then fluctuations in the flow, i.e. turbulence, are introduced as well. The effect of the ground roughness will then decrease as a function of height over the ground (see [55]).

2.1.1 Turbulence

Suppose the mean wind speed, $\bar{U}$, is typically determined as a 10 minute average value, then instantaneous wind speed U can be described as $\bar{U}$ plus a fluctuating wind component δ (see [55] and [45]).

$$U = \bar{U} + \delta. \tag{2.1.1}$$

The turbulence intensity, *TI*, is computed by

$$TI = \frac{\sigma_U}{U},$$

where σ_U denotes the standard deviation of the wind speed. This is also calculated over a time period of 10 minutes, with sampling frequency at least 1 Hz (see [45]). The ef-

Table 2.1: Parameters for calculating vertical profile of wind speed

Type of terrain	Roughness class	$h^r(m)$	a
Water areas	0	0.001	0.01
Open country, few surface features	1	0.12	0.12
Farmland with buildings and hedges	2	0.05	0.16
Farmland with many trees, forest and villages	3	0.3	0.28

fect of the friction at the ground, the roughness, will decrease as the elevation increases. The wind speed increases with increasing height as well which can be described by the following power exponent function

$$U(h) = U^{ref}\left(\frac{h}{h^r}\right)^a,$$

where $U(h)$ is the wind speed at height h above ground level, U^{ref} is the wind speed at the reference height h^r and a is the so-called Hellman exponent (see [24]) which depends on the roughness of the terrain. Some parameters for a and h^r for different type of terrain are shown in Table 2.1 (see [55]).

2.1.2 Wind speed model

As described in the previous section the characteristics of the wind will be affected by the factors such as turbulence and height above ground. In the model of the wind that is used for the simulations, following [45] and [43], the wind speed can be computed based on the frequency spectrum proposed by Kaimal given by

$$\mathbf{S}(f) = \left(\frac{0.4}{\log(h/h^r)}\right)^2 \frac{105h\bar{U}}{(1+33fh/\bar{U})^{5/3}},$$

where f is the frequency. This is then solved by the relation taken from the probability theory

$$Var[U(t)] \approx \int_0^{f_{cut}} \mathbf{S}(f)df, \tag{2.1.2}$$

where f_{cut} means the (upper) frequency at which to cut the spectrum. For values of f_{cut} in the range from 10 to 100 Hz, Equation (2.1.2) will, according to [43], give a very good

approximation. This is the description of the wind characteristics in one dimension which is used in this thesis. A simulated wind speed with low turbulence intensity can be seen in Figure 2.1.

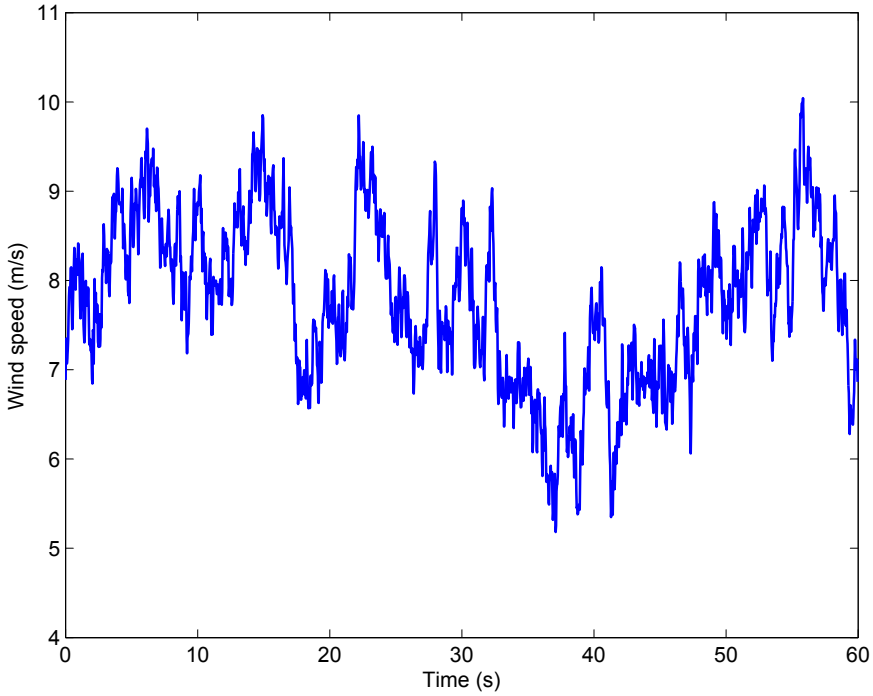

Figure 2.1: Simulated wind speed sampled at 30Hz and mean wind speed 8 m/s

2.2 Aerodynamics of horizontal-axis wind turbines

In this section, the background concepts on turbine aerodynamics are taken from Burton, Sharpe, Jenkins and Bossanyi [10] and Heier [24].

2.2.1 The actuator disc concept

The aerodynamic behavior of the wind turbine can be analyzed without any specific turbine design just by considering the energy extraction process. Actuator disc is introduced to carry out this task (see [10]).

Assumptions:

- The affected mass of air remains separates from the air which does not pass through the actuator disc;
- A boundary surface can be drawn containing the affected air mass and this boundary can be extended upstream as well as downstream forming a long stream-tube of circular cross section.

Because the air within the stream-tube slows down, but does not become compressed, the cross-sectional area of the stream-tube must expand to accommodate the slower moving air (see Figure 2.2).

As the air passes through the rotor disc, by design, there is a drop in static pressure such that, on leaving, the air is below the atmospheric level. The air then proceeds downstream with reduced speed and static pressure–this region of flow is called the *wake*.

The mass of air which passes through a given cross section of the stream-tube in the unit length of time is ρAU, where ρ denotes the air density, A the cross-sectional area and U the flow velocity. No air flows across the boundary and so the mass flow rate of the air flowing along the steam-tube will be the same for all stream-wise positions along the steam-tube,

$$\rho A_\infty U_\infty = \rho A_d U_d = \rho A_w U_w,$$

where the symbol ∞ refers to conditions far upstream, d refers to conditions at the disc and w refers to conditions in the far wake.

The actuator disc induced a velocity variation which must be superimposed on the free-stream velocity. The stream-wise component of this induced flow at the disc is given by $-aU_\infty$, where a is called the *axial flow induction factor*, or the *inflow factor*. At the disc, therefore, the net stream-wise velocity is

$$U_d = U_\infty(1 - a). \tag{2.2.1}$$

Momentum theory

The overall change in velocity of the air passing through the disc is, $U_\infty - U_w$. A rate of change of momentum, R_M, equals to the overall change of velocity times the mass flow

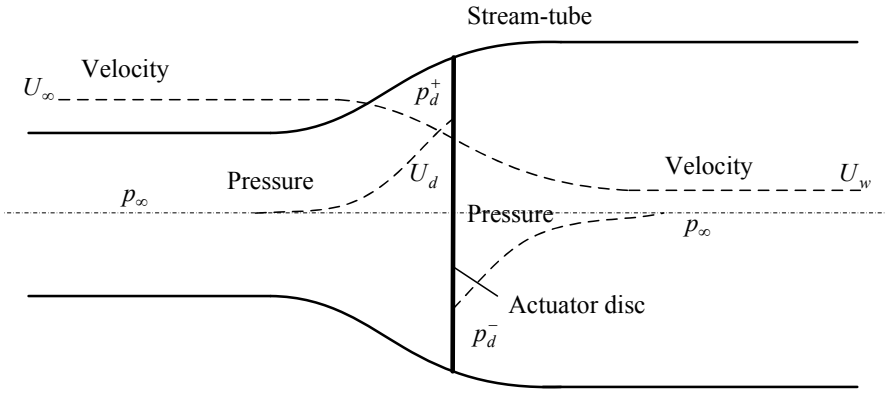

Figure 2.2: An energy extracting actuator disc and stream-tube.

rate:

$$R_M = (U_\infty - U_w)\rho A_d U_d.$$

The force causing this change of momentum comes entirely from the pressure difference across the actuator disc,

$$F = (p_d^+ - p_d^-)A_d = R_M. \tag{2.2.2}$$

where F denotes the force on the air. It can be shown that (see [10])

$$U_w = (1 - 2a)U_\infty. \tag{2.2.3}$$

Substituting (2.2.1) and (2.2.3) into (2.2.2), we obtain

$$F = 2\rho A_d U_\infty^2 a(1 - a).$$

Power coefficient

The power extracted from the air is given by

$$P_a = FU_d = 2\rho A_d U_\infty^3 a(1 - a)^2. \tag{2.2.4}$$

The *power coefficient* is then defined as

$$C_p = \frac{P_a}{0.5\rho A_d U_\infty^3} = 4a(1 - a)^2. \tag{2.2.5}$$

The maximum value of C_p occurs when

$$\frac{dC_p}{da} = 4(1 - a)(1 - 3a) = 0,$$

which gives a value of $a = \frac{1}{3}$ and the maximum achievable value of the power coefficient $C_{pBetz} = 0.593$. This maximum power coefficient is known as the Betz limit after Albert Betz, a German physicist and a pioneer of wind turbine technology. The Betz' law states that independent of the design of a wind turbine only 59.3% of the kinetic energy in the wind can be converted to mechanical energy. To date, no wind turbine has been designed which is capable of exceeding this limit. The limit is not caused by any deficiency in design, but because of the tube where the air is at the full free-stream velocity is smaller than the area of disc.

Using the concept of C_p, we rewrite (2.2.4):

$$P_a = 0.5\rho\pi R_w^2 C_p U_\infty^3, \tag{2.2.6}$$

where R_w is the blade length. The power coefficient C_p is a function of the *tip-speed ratio* (TSR) λ and *pitch angles* β as shown in Figure 2.3(b). If we denote by ω_T the turbine speed, then

$$\lambda = \frac{R_w \omega_T}{U_\infty}. \tag{2.2.7}$$

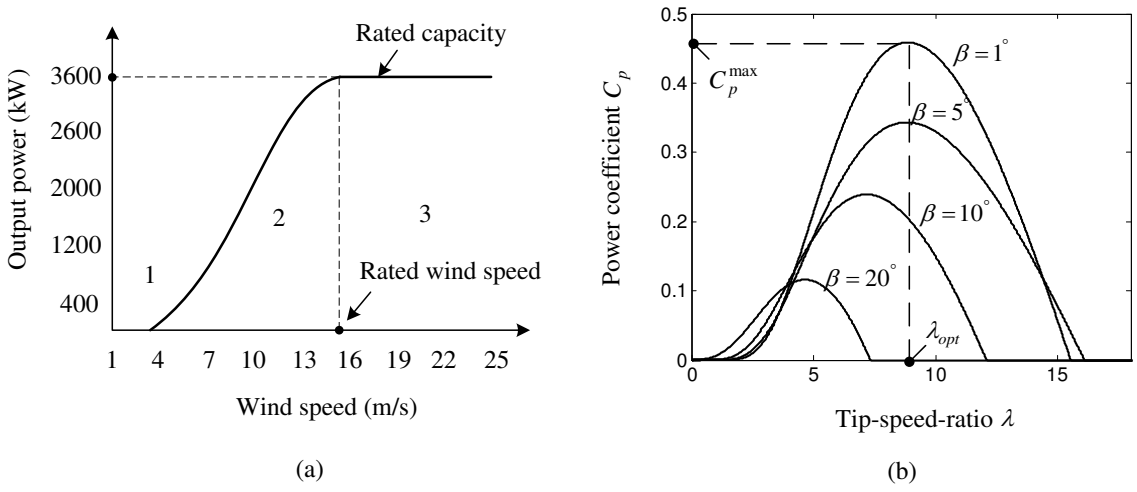

Figure 2.3: (a) Output power of a typical wind turbine operating in different wind speed regions, denoted by 1, 2 and 3 (taken from GE, see[17]). (b) Typical C_p curves for a wind turbine, as a function of λ and β.

The pitch angle is the angle of the rotation of the blades around their main axis, with respect to a reference position (see Figure 2.5 (a)). In region 2, the pitch angle is kept

constant, at an optimal value (1° in the example shown in Figure 2.3(b)). P_a can be maximized if the wind turbine is operating at maximum C_p.

To evaluate the C_p performance characteristic, there are two methods available

- data fields containing the family of curves derived from measurements or from calculation;
- analytical functions.

If the turbine characteristics or the data for plotting them are available then the data fields can be created by reading off the various values or entering them directly. These then form the basis for performance computation in system simulations. The validity of the results therefore will then be dictated by that of the data. When enough data are available, linear interpolation can be used to arrive at intermediate values.

To arrive at a complete data set for the operation of a turbine, it may however be necessary to extend the characteristics plot. By extending the characteristic curves for small, or even negative, or large angles and by supplementing incomplete characteristics, undefined operating states can be avoided. In this case, approximation of the C_p curves by non-linear analytical functions is quite useful to forecast those extreme situations. Following [24], a family of C_p curves can be generated by

$$C_p = c_1(c_2 - c_3\beta - c_4\beta^{1.5} - c_5)e^{-c_6}, \tag{2.2.8}$$

where $c_1 = 0.5$, $c_2 = \frac{116}{\lambda_i}$, $c_3 = 0.4$, $c_4 = 0$, $c_5 = 5$, $c_6 = \frac{21}{\lambda_i}$ and

$$\frac{1}{\lambda_i} = \frac{1}{\lambda + 0.08\beta} - \frac{0.035}{\beta^3 + 1}.$$

In practice, the C_p curves must be modified to obtain a close simulation of the machine in question. To manage this, however, demands a non-negligible investment of time and effort, even for those with long experience of performing such approximations

2.2.2 Rotor blade theory

Assume optimal operation which implies maximum power efficiency, and a is constant along each blade, we could take $a = \frac{1}{3}$, which will produce $C_p^{max} = C_{pBetz}$. For more

realistic C_p curves shown in Figure 2.3(b), if the pitch angle β is fixed to be its optimal value $\beta^{opt} = 1^\circ$, then the corresponding $C_p^{max} = 0.4587$ will produce a more realistic axial flow induction factor $a = 0.164$ (see (2.2.5)). Again we assume that a is constant along each blade, then for the segment with distance from root r (see Figure 2.4), we have

$$\begin{aligned} a' &= \frac{a(1-a)}{\lambda^2\mu^2}, \\ \tan\phi &= \frac{1-a}{\lambda\mu(1+a')}, \\ \alpha &= \phi - \beta, \end{aligned} \tag{2.2.9}$$

where $\mu = \frac{r}{R_w}$ is the non-dimensional radial position, α denotes the angle of attack (AoA), and a' is the tangential flow induction factor. Given Figure (2.6), once an AoA is available from (2.2.9), the corresponding lift coefficient C_l and drag coefficient C_d can be found using interpolation. Then we are able to calculate the blade forces (see Figure 2.5(b)).

$$\begin{aligned} V_{wr} &= \sqrt{U_\infty^2(1-a)^2 + \omega_T^2 r^2(1+a')^2}, \\ dF_L &= \frac{1}{2}\rho V_{wr}^2 c C_l dr, \\ dF_D &= \frac{1}{2}\rho V_{wr}^2 c C_d dr, \\ dF_{ax} &= dF_L\cos(\phi) + dF_D\sin(\phi), \\ dF_T &= dF_L\sin(\phi) - dF_D\cos(\phi), \end{aligned}$$

where V_{wr} is the relative wind speed at the blade, c is the chord, F_L is the lift force normal to the direction of V_{wr}, F_D is the drag force parallel to the direction of V_{wr}, F_{ax} is the axial force, and F_T is the torque generating force.

After some rearrangements and substitutions, we obtain

$$dF_{ax} = \frac{1}{2}\rho V_{wr}^2 N c(C_l\cos\phi + C_d\sin\phi)dr,$$

where N denotes the number of blades.

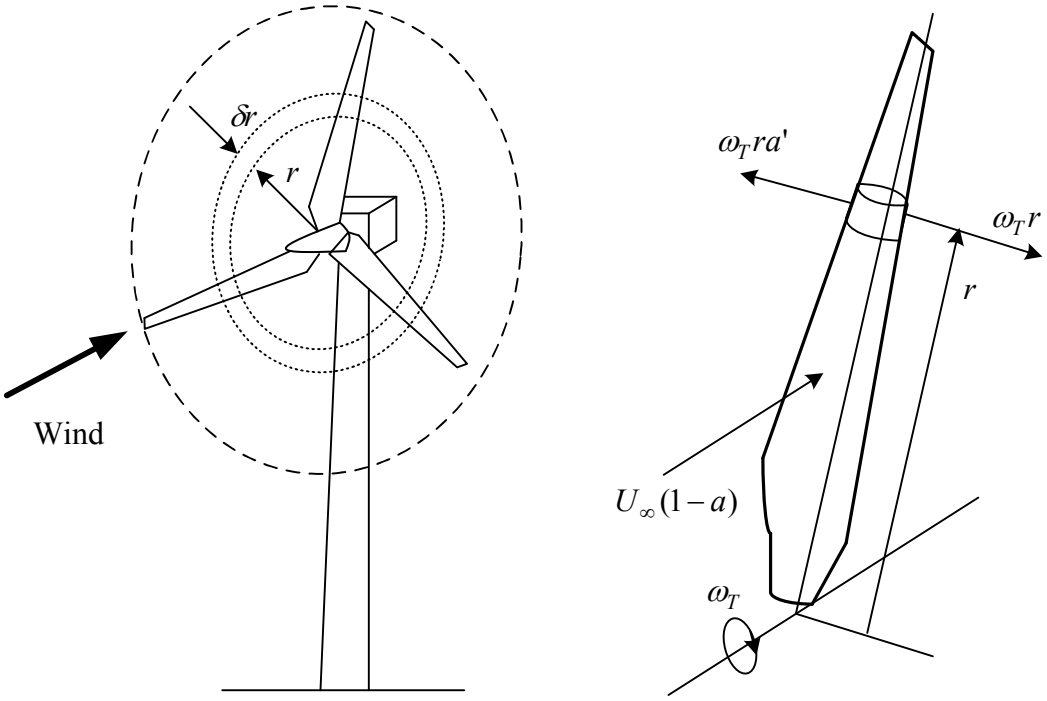

Figure 2.4: A blade element sweeps out an annular ring

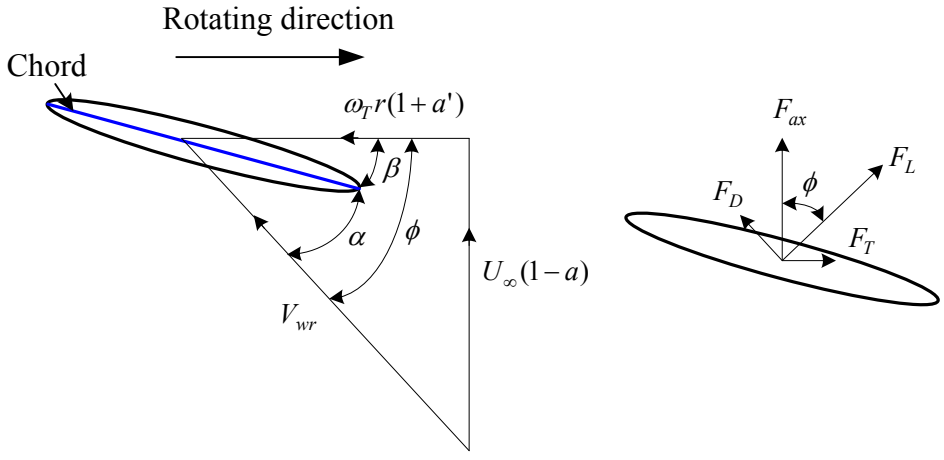

(a) Velocities (b) Forces

Figure 2.5: Blade element velocities and forces

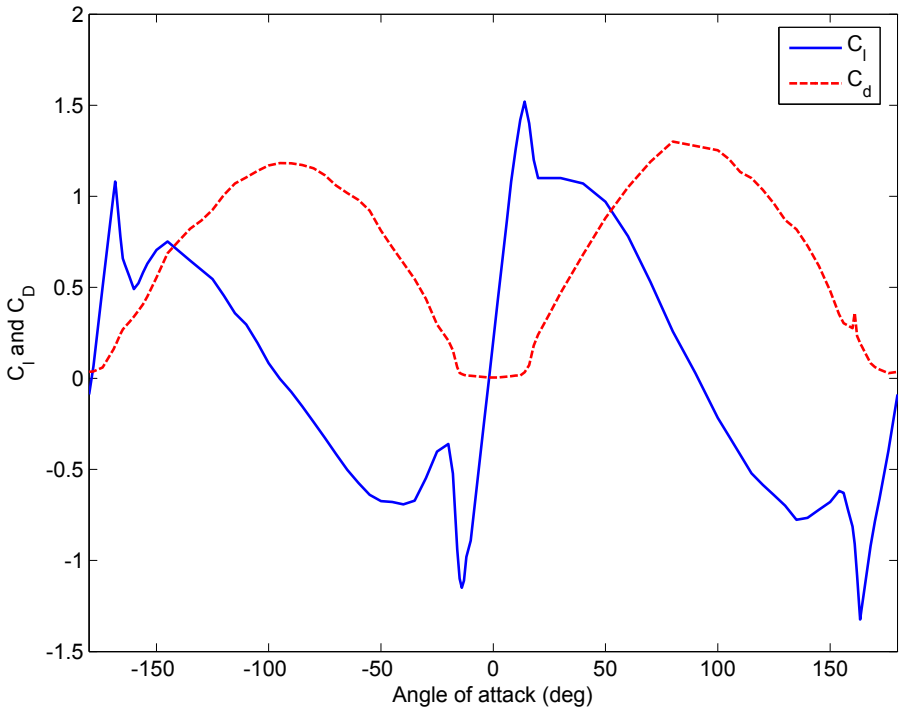

Figure 2.6: Lift coefficient and drag coefficient

2.3 Torque control in region 2

We give a short derivation of the quadratic torque control law that is usually employed when the wind is not too strong (region 2) and the objective is to maximize the output power of the turbine. Figure 2.3(a) shows the desired output power as a function of the wind speed.

As explained in [10] and [24], the available wind power is given by

$$P_{wind} = 0.5\rho\pi R_w^2 U_\infty^3, \tag{2.3.1}$$

and the power captured by the wind turbine is P_a, see (2.2.6).

The aerodynamic torque T_a at the turbine shaft is (neglecting losses in the drive-train)

$$T_a = 0.5\rho\pi R_w^3 C_t U_\infty^2, \tag{2.3.2}$$

where $C_t = \frac{C_p(\lambda,\beta)}{\lambda}$ is the torque coefficient. Figure 2.7 shows the Simulink model of the wind turbine.

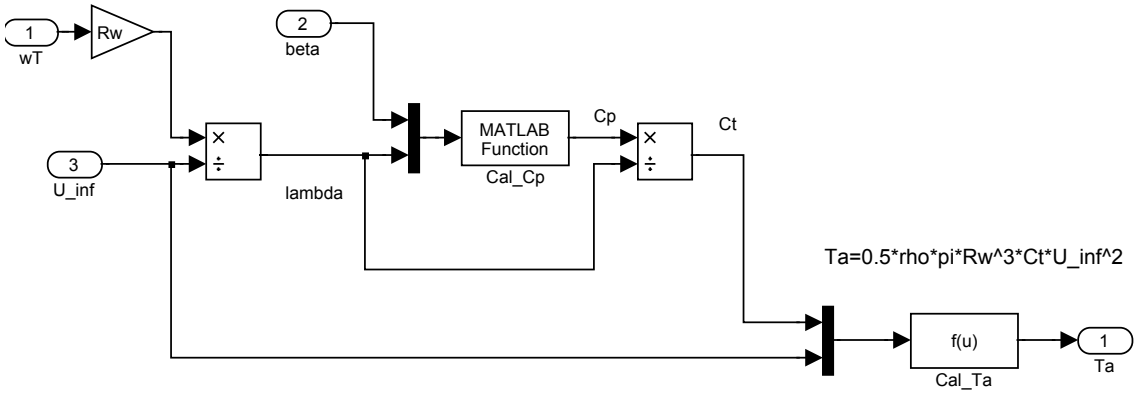

Figure 2.7: The Simulink model of the wind turbine. The 'Cal C_p' block is shown in (2.2.8). The 'Cal T_a' block is shown in (2.3.2).

The standard region 2 torque control scheme for a variable-speed wind turbine is to set

$$\begin{aligned} T_e^{ref} &= \frac{P_a^{max}}{\omega_m} = \frac{0.5\rho\pi R_w^2 C_p^{max} U_\infty^3}{\omega_m}, \\ &= \frac{0.5\rho\pi R_w^2 C_p^{max} (\frac{R_w \omega_T}{\lambda_{opt}})^3}{\omega_m} = \frac{0.5\rho\pi R_w^5 C_p^{max}}{\lambda_{opt}^3 n_g^3} \omega_m^2, \end{aligned}$$

where T_e^{ref} is the reference electrical torque, ω_m is the generator speed and n_g is the gearbox ratio (see [31, 42]). In this derivation, the meaning of P_a^{max}, C_p^{max} and λ_{opt} is easy to infer. Thus, to maximize P_a, we set

$$T_e^{ref} = K^{opt} \omega_m^2, \quad K^{opt} = \frac{0.5\rho\pi R_w^5 C_p^{max}}{\lambda_{opt}^3 n_g^3}. \tag{2.3.3}$$

Note that in steady state $\omega_m = n_g \omega_T$. Actually, the control law (2.3.3) is only applied when $\omega_m > 0$. In the rare instances when $\omega_m < 0$ (i.e. the turbine spins backwards), it is considered better not to apply any electrical torque, i.e. $T_e^{ref} = 0$, and wait until the speed reverses to $\omega_m > 0$ (this may need the intervention of the yaw controller), see [31].

The quadratic control law (2.3.3) requires the knowledge of K^{opt}, which may be supplied by the turbine manufacturer. In practice, however, K^{opt} may vary from turbine to turbine (even if they are meant to be equal) and it may also change during a turbine's life span. In our stability analysis (see Chapter 5) we assume that $T_e^{ref} = K\omega_m^2$, where $K > 0$ (not necessarily the optimal gain K^{opt}) is constant. In Section 5.4 we describe a simple adaptive search algorithm that updates K, to an estimate of K^{opt} (when the wind speed is in region 2).

Figure 2.9(a) shows the overall control system in region 2. In this diagram, the DFIG, the grid, the transformer, the two converters and the controllers directly attached to these converters have been packaged into one block.

2.4 Control strategies in region 3

A wind turbine is subject to many different modes of vibration. Figure 2.8 explains fore-aft vibrations and side-to-side vibrations of the tower. In addition, each blade can vibrate in two main directions and the low-speed drive-train (up to and including the gearbox) is subject to torsional vibrations (see [10, 9, 63]). The frequencies of vibration depend on the turbine, however typical frequencies are known, such as for example the first vibration frequency of 0.32Hz, for the tower of a 5MW turbine, with an average tower diameter of 6m and a 250 ton nacelle at 125m above the sea. The first vibration frequency of the drive-train of the same turbine is around 4.8Hz (see [33]). We cannot suppress all the vibrations, because we have only two control variables at our disposal: the electrical torque (through which we can indirectly control the turbine speed) and the rotor collective pitch (through which we can regulate aerodynamic torque, which regulates speed). We will investigate which vibrations it would be best to suppress. This depends on risk considerations (how damaging are the various vibrations to the structure) as well as on feasibility considerations.

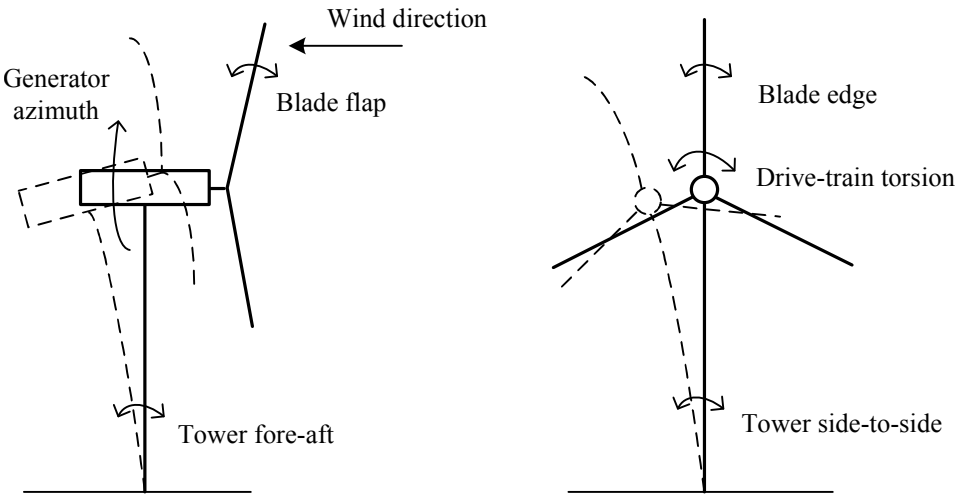

Figure 2.8: Assumed wind turbine model with 10 degree-of-freedom.

2.4.1 Control of tower fore-aft vibration

The 1^{st} tower fore-aft vibrational mode is poorly damped, exhibiting a strong resonant response even by a small amount of excitation which is naturally present in the wind (see [10]). Given the 1^{st} fore-aft mode of the wind turbine tower, we have (see [9])

$$M\ddot{x} + D_1\dot{x} + K_1 x = F_{ax}, \tag{2.4.1}$$

where M, D_1, and K_1 denote system mass, damping, and stiffness, respectively. Then the 1^{st} tower fore-aft mode frequency is $\omega_{fa1} = \sqrt{\frac{K_1}{M}}$ rad/s. The axial-force F_{ax} can be approximated by

$$F_{ax} = F_{ax}^{op} + \delta F_{ax}, \tag{2.4.2}$$

$$\delta F_{ax} \approx \frac{\partial F_{ax}}{\partial U_\infty}\delta U_\infty + \frac{\partial F_{ax}}{\partial \omega_T}\delta\omega_T + \frac{\partial F_{ax}}{\partial \beta}\delta\beta. \tag{2.4.3}$$

We take

$$\frac{\partial F_{ax}}{\partial \beta}\delta\beta = -D_{add1}\dot{x}, \tag{2.4.4}$$

$$\delta\beta = \frac{-D_{add1}}{\partial F_{ax}/\partial\beta}\dot{x}, \tag{2.4.5}$$

where F_{ax}^{op} is the axial force at an operating point, D_{add1} is the additional damping, and the prefix δ means a small deviation of a variable from its operating point. The tower velocity $\dot{x}$ can be calculated by integration of the tower acceleration measured by an accelerometer mounted in the nacelle.

If we take the state variables as x and $\dot{x}$, disturbances as F_{ax}^{op}, δU and $\delta\omega_T$, control input as $\delta\beta$,

$$\zeta = \begin{bmatrix} x \\ \dot{x} \end{bmatrix}, w = \begin{bmatrix} F_{ax}^{op} \\ \delta U \\ \delta\omega_T \end{bmatrix}, u = \delta\beta.$$

then the linearized state-space model can be written as

$$\dot{\zeta} = A\zeta + [B_1 \quad B_2 \quad B_3]w + B_4 u, \tag{2.4.6}$$

where

$$A = \begin{bmatrix} 0 & 1 \\ -\frac{K_1}{M} & -\frac{D_1}{M} \end{bmatrix}, \tag{2.4.7}$$

$$B = [B_1 \quad B_2 \quad B_3 \quad B_4] \tag{2.4.8}$$

$$= \begin{bmatrix} 0 & 0 & 0 & 0 \\ \frac{1}{M} & \frac{1}{M}\frac{\partial F_{ax}}{\partial U_\infty} & \frac{1}{M}\frac{\partial F_{ax}}{\partial \omega_T} & \frac{1}{M}\frac{\partial F_{ax}}{\partial \beta} \end{bmatrix}. \tag{2.4.9}$$

The damping D_1 is composed of structural damping and aerodynamic damping elements.

$$D_1 = D_{1struct} + D_{1aero}. \tag{2.4.10}$$

Given the structural damping ratio ξ_{s1}, the structural damping element can be computed as:

$$D_{1struct} = 2M\omega_{fa1}\xi_{s1}. \tag{2.4.11}$$

The aerodynamic damping is almost entirely provided by the turbine rotor, the damping ratio for the 1^{st} tower fore-aft mode can be computed approximately as

$$\xi_{a1} = \frac{\frac{1}{2}\rho N\omega_T \int_0^{R_w} \frac{dC_l}{d\alpha} rc(r)dr}{2M\omega_{fa1}}. \tag{2.4.12}$$

So the aerodynamic damping element is

$$D_{1aero} = 2M\omega_{fa1}\xi_{a1}. \tag{2.4.13}$$

For a detailed study of turbine structural dynamics, please refer to S. Suryanarayanan and A. Dixit [53].

2.4.2 Control of drive-train torsional vibration

The primary goal in region 3 (above the rated wind speed, see Figure 2.3(a)) is to maintain the generated power at the rated value. This is done by maintaining a constant electrical torque (using the rotor current controller and the rotor-side converter) and regulating the turbine speed by pitch control. Another important control objective is to increase the life span of the gearbox (and possibly other components) by suppressing the mechanical oscillations in the turbine shaft (see [9, 10, 63]). The overall control system in region 3 is shown in Figure 2.9(b).

In region 3, we try to keep the electrical torque of the generator constant, at the value T_e^{rated}. However, strong variations of the wind speed V_w may cause (lightly damped) oscillations in the drive-train. These oscillations can be very harmful to the gearbox, which is one of the most expensive yet fragile components in a wind turbine. Thus, it is desirable to reduce these oscillations. One method, which has been successfully adopted on many turbines, is to modify the generator torque. A small ripple δT_e at the drive-train

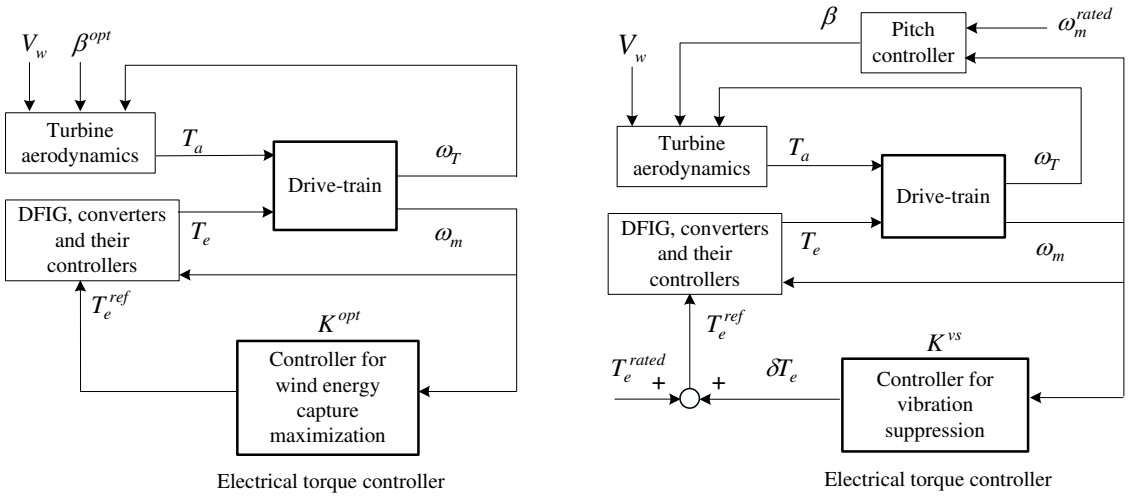

(a) Region 2 operation (wind in the normal range)

(b) Region 3 operation (strong wind)

Figure 2.9: Block diagrams for the control of the mechanical part of a wind turbine in both regions 2 and 3. Note that the pitch controller and the drive-train vibration controller K^{vs} are only functioning in region 3.

resonant frequency is added to T_e^{rated}, with its phase adjusted, to counteract the effect of the resonance and effectively increase the damping (see Figure 2.9(b)). A high-pass filter of the form

$$K^{vs}(s) = \frac{s}{s + \omega_h}, \tag{2.4.14}$$

acting on ω_m can be used to generate this ripple, see [9, 10]. The frequency ω_h should be less than the resonant frequency which is to be damped.

Based on internal model theory, the damping performance can be improved by adding a narrow-band filter to the high-pass filter. In this case, the electrical torque controller has the transfer function

$$K^{vs}(s) = k_h \frac{s}{s + \omega_h} + k_p \frac{s}{s^2 + \omega_p^2}, \tag{2.4.15}$$

where ω_p should also be close to the first drive-train torsion mode, while k_h and k_p are parameters to be chosen. This results in an infinite loop-gain at the frequency ω_p, so that the sensitivity of the feedback system is zero at this frequency.

2.5 Reference frame conversion

2.5.1 Transformation from a three phase to a stationary reference frame

A three phase signal with three quantities (s_a, s_b and s_c), such as voltage u, current i and flux ψ can be transformed to a two phase vector in the complex plane by:

$$\vec{s}_{\alpha\beta} = s_\alpha + j s_\beta = c(s_a e^{j0} + s_b e^{j\frac{2\pi}{3}} + s_c e^{j\frac{4\pi}{3}}).$$

or expressed by matrix

$$\begin{bmatrix} s_\alpha \\ s_\beta \\ s_0 \end{bmatrix} = \mathbf{T}_S \begin{bmatrix} s_a \\ s_b \\ s_c \end{bmatrix},$$

where

$$\mathbf{T}_S = c \begin{bmatrix} 1 & -\frac{1}{2} & -\frac{1}{2} \\ 0 & \frac{\sqrt{3}}{2} & -\frac{\sqrt{3}}{2} \\ \frac{\sqrt{2}}{2} & \frac{\sqrt{2}}{2} & \frac{\sqrt{2}}{2} \end{bmatrix},$$

and c is a constant. If we take $c = \sqrt{\frac{2}{3}}$, then $\mathbf{T}_S$ is *unitary*, which has the *energy-preserving* property: $\|x\| = \|\mathbf{T}_S x\|, \quad \forall x \in \mathbf{C^n}$. $n = 3$ for a three phase signal. In other words, the power of the system in abc-frame is the same as in the $\alpha\beta$-frame. The $\alpha\beta$-system is then called *power-invariant*. If we take $c = \frac{2}{3}$, then the modulus of the signal is maintained after transformation. This $\alpha\beta$-system is then called *non power-invariant*. See Figure 2.10 for a visualization of the abc to $\alpha\beta$ transformation.

2.5.2 Transformation from a stationary to a rotating reference frame

The $\alpha\beta$ to dq transformation can be written as:

$$\vec{s}_{dq} = s_d + j s_q = \vec{s}_{\alpha\beta} e^{-j\theta}$$

or expressed by matrix

$$\begin{bmatrix} s_d \\ s_q \\ s_0 \end{bmatrix} = \mathbf{T}_R \begin{bmatrix} s_\alpha \\ s_\beta \\ s_0 \end{bmatrix},$$

where

$$\mathbf{T}_R = \begin{bmatrix} \cos\theta & \sin\theta & 0 \\ -\sin\theta & \cos\theta & 0 \\ 0 & 0 & 1 \end{bmatrix}.$$

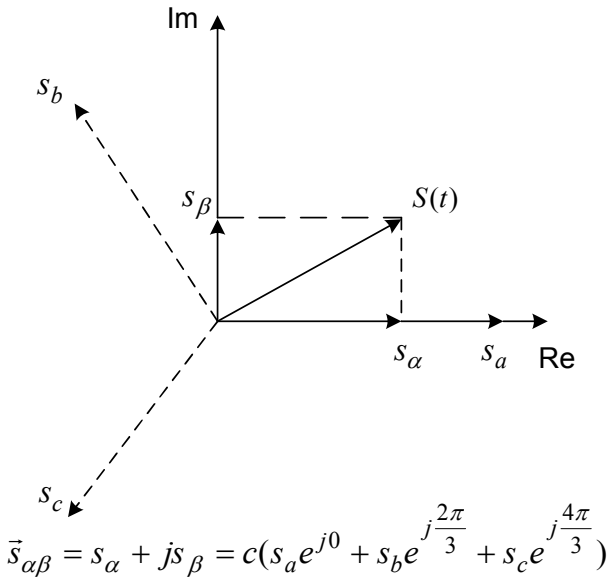

Figure 2.10: Transformation from abc to $\alpha\beta$-reference frame

$\mathbf{T}_R$ is *unitary*. Therefore energy-preserving property holds for dq transformation. See Figure 2.11 for a visualization of the $\alpha\beta$ to dq transformation.

Power-invariant transformation

Assume a sinusoidal symmetric three-phase supply voltage system with RMS value U, frequency ω_1 and phase shift $\frac{2\pi}{3}$ given by

$$\begin{aligned} u_a &= \sqrt{2}U\cos(\omega_1 t), \\ u_b &= \sqrt{2}U\cos(\omega_1 t - \frac{2\pi}{3}), \\ u_c &= \sqrt{2}U\cos(\omega_1 t - \frac{4\pi}{3}). \end{aligned}$$

The voltage space phasor in the $\alpha\beta$-reference frame is the following:

$$\begin{aligned} \vec{u}_{\alpha\beta} &= u_\alpha + ju_\beta = \sqrt{3}Ue^{j\omega_1 t}, \\ \vec{u}_{dq} &= \vec{u}_{\alpha\beta}e^{-j\theta} = \sqrt{3}Ue^{j(\theta_1-\theta)}. \end{aligned}$$

where $\omega_1 = d\theta_1/dt$.

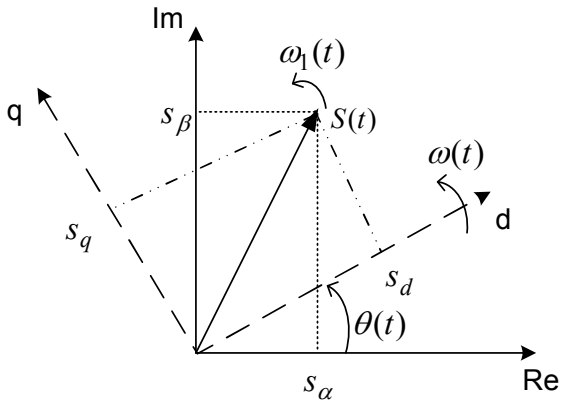

$$\vec{s}_{dq} = s_d + js_q = \vec{s}_{\alpha\beta} e^{-j\theta},$$
$$\omega = d\theta / dt.$$

Figure 2.11: Transformation from $\alpha\beta$ to dq-reference frame

The instantaneous active power, P, is given by

$$\begin{aligned} P &= v_a i_a + v_b i_b + v_c i_c = \mathbf{Re}(v_{\alpha\beta} i^*_{\alpha\beta}), \\ &= v_\alpha i_\alpha + v_\beta i_\beta, \\ &= v_d i_d + v_q i_q. \end{aligned}$$

The instantaneous reactive power, Q, is given by

$$\begin{aligned} Q &= \mathbf{Im}(v_{\alpha\beta} i^*_{\alpha\beta}) = -v_\alpha i_\beta + v_\beta i_\alpha, \\ &= -v_d i_q + v_q i_d. \end{aligned}$$

Non power-invariant transformation

The voltage space phasor in the $\alpha\beta$-reference frame is the following:

$$\vec{u}_{\alpha\beta} = u_\alpha + ju_\beta = \sqrt{2}Ue^{j\omega_1 t}, \tag{2.5.1}$$

$$\vec{u}_{dq} = \vec{u}_{\alpha\beta} e^{-j\theta} = \sqrt{2}Ue^{j(\theta_1 - \theta)}. \tag{2.5.2}$$

The instantaneous active power, P, is given by

$$\begin{aligned} P &= v_a i_a + v_b i_b + v_c i_c = \frac{3}{2}\mathbf{Re}(v_{\alpha\beta} i^*_{\alpha\beta}), \\ &= \frac{3}{2}(v_\alpha i_\alpha + v_\beta i_\beta), \\ &= \frac{3}{2}(v_d i_d + v_q i_q). \end{aligned}$$

The instantaneous reactive power, Q, is given by

$$\begin{aligned} Q &= \frac{3}{2}\mathbf{Im}(v_{\alpha\beta} i^*_{\alpha\beta}) = \frac{3}{2}(-v_\alpha i_\beta + v_\beta i_\alpha), \\ &= \frac{3}{2}(-v_d i_q + v_q i_d). \end{aligned}$$

In this thesis, we only consider the power-invariant transformation.

2.6 Wind-driven doubly-fed induction generator

2.6.1 Some typical features and advantages of the DFIG

Some typical features and merits of the wind-driven DFIG can be concluded as follows:

- Converters only need to handle approximately 30% of the total generator power, so we can use cheap converters to control a machine of high power capacity;
- Wind farms equipped with DFIG wind turbines are able to compensate or produce reactive power through power electronic converters, so there is no need to install capacitor banks as in the case of squirrel cage induction generators.
- Speed variation of 30% around synchronous speed can be obtained. This large speed variation range allows the DFIG to extract maximum energy from the wind for low wind speeds by optimizing the turbine speed and to minimize mechanical stresses on the turbine during wind gusts;
- It is possible to save on the safety margin of gear;
- In industry, DFIG wind turbine has been well developed by manufacturers, such as Vestas (V80–2MW) and GE wind (3.6s–3.6MW).

2.6.2 Power flow

Now we discuss more about the active and reactive powers of the DFIG.

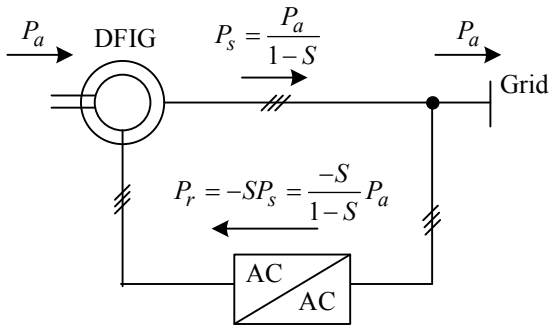

Figure 2.12: Power flow of a lossless DFIG wind turbine system

- Assume the power converter is lossless, then the total mechanical power P_a of the lossless DFIG system is simply the sum of stator power P_s and rotor power P_r:

$$P_a = P_s + P_r. \tag{2.6.1}$$

The active power from the rotor is proportional to the *slip*, S, of the generator:

$$S = \frac{\omega_s - \omega_r}{\omega_s}, \tag{2.6.2}$$

$$P_r = -SP_s, \tag{2.6.3}$$

where ω_s is the synchronous speed, ω_r is the generator rotor speed. Substituting equation (2.6.3) into equation (2.6.1)

$$P_a = (1 - S)P_s. \tag{2.6.4}$$

If the generator is running super-synchronously (called *super-synchronous mode*), it will feed electrical power to the grid through both the rotor and the stator. If the generator is running sub-synchronously (called *sub-synchronous mode*), the electrical power is only delivered into the rotor from the grid (see [8]).

- Assume the converter is able to control the power flow at the converter-supply side at any time so its reactive power is zero. This assumption is reasonable because the

converter rating is a maximum 30% of the generator rating and it is used primarily for supplying the active power of the rotor to the grid. Therefore, the reactive power exchanged between the DFIG and the grid is equal to the reactive power in the stator:

$$Q_{total} = Q_s$$

- The reactive power from the stator will be zero in case of a strong power system or when there is no requirement for the DFIG control ability of the voltage. In this case, the DFIG supplies only active power and is magnetized through the rotor, with the power factor of the DFIG close to unity. Otherwise, the reactive power set-point of the DFIG will be defined for the voltage control purpose (see [2]).

2.6.3 The 4th-order DFIG model

To investigate the dynamic modeling of the DFIG in power systems, we consider the following modeling issues, see [2]:

- Modeling of the DFIG itself using its physical state equations;
- Representation of its control systems for the decoupled control of the active and reactive powers.

For power system stability studies it is desirable to apply reduced models of the machine and the converter in order to relax the computation burden. The comparison between reduced models and more detailed models has been discussed in the literature (see [39] and [47]). The manufacturer Vestas has agreed that the 4th-order model of the DFIG, at least, is necessary for power stability investigation (see [2] and [39]). Therefore, with respect to the generator, the fifth order model is considered in this thesis. With respect to the converter, a classical approach is adopted, i.e. the converter is modeled as a simple gain in the controller designing phase. But a more elaborated converter model can be introduced in simulation to validate the control law [37].

State equations of the 4^{th} order DFIG model can be written as the following [54]:

$$\begin{aligned}
\Psi_{ds} &= L_s i_{ds} + L_m i_{dr}, \\
\Psi_{qs} &= L_s i_{qs} + L_m i_{qr}, \\
\Psi_{dr} &= L_r i_{dr} + L_m i_{ds}, \\
\Psi_{qr} &= L_r i_{qr} + L_m i_{qs}, \\
v_{ds} &= R_s i_{ds} - \omega_s \Psi_{qs} + \frac{d\Psi_{ds}}{dt}, \\
v_{qs} &= R_s i_{qs} + \omega_s \Psi_{ds} + \frac{d\Psi_{qs}}{dt}, \\
v_{dr} &= R_r i_{dr} + \frac{d\Psi_{dr}}{dt} - \omega_{sl} \Psi_{qr}, \\
v_{qr} &= R_r i_{qr} + \frac{d\Psi_{qr}}{dt} + \omega_{sl} \Psi_{dr}.
\end{aligned}$$

$$\begin{aligned}
T_e &= n_p \frac{L_m}{L_s} (\Psi_{qs} i_{dr} - \Psi_{ds} i_{qr}), \\
\omega_{sl} &= \omega_s - \omega_r, \\
S &= \frac{\omega_{sl}}{\omega_s}.
\end{aligned}$$

The Simulink model of the 4^{th} order DFIG is shown in Appendix B.

2.6.4 Modeling of DFIG in the stator-flux reference frame

To achieve a decoupled control between the stator active and reactive powers, we choose a *dq* representation of the DFIG, with the d-axis oriented along the stator-flux vector position. Since the stator is connected to the grid, we could make the following assumptions [54]:

- The stator resistance R_s can be $neglected$ (usually justified in machines with a rating over $10kW$);
- The stator magnetizing current space phasor: $\vec{i}_{ms} = |\vec{i}_{ms}| \angle \rho_s$. In the steady state, $|\vec{i}_{ms}| = constant$ and $\rho_s = constant$;
- Frequency of the power supply on the stator is constant, i.e. $\omega_s = constant$.

Under those assumptions, it implies that:

$$\begin{aligned}
\Psi_{ds} &= \Psi_s = L_m|\vec{i}_{ms}|, \\
\Psi_{qs} &= L_s i_{qs} + L_m i_{qr} = 0, \\
\Psi_{dr} &= \frac{L_m^2}{L_s}|\vec{i}_{ms}| + \sigma L_r i_{dr}, \\
\Psi_{qr} &= \sigma L_r i_{qr}, \\
|\vec{i}_{ms}| &= \frac{|\vec{v}_s|}{\omega_s L_m},
\end{aligned}$$

where $\sigma = 1 - \frac{L_m^2}{L_s L_r}$, and $|\vec{v}_s| = \sqrt{3}V_s$. V_s is the RMS of the stator-voltage space phasor in the stationary reference frame, $\vec{v}_s = \sqrt{3}V_s e^{j\omega_s t}$.

After some substitutions, the stator and rotor voltages can be written as:

$$v_{ds} = R_s i_{ds} - \omega_s \Psi_{qs} + \frac{d\Psi_{ds}}{dt} \approx 0, \tag{2.6.5}$$

$$v_{qs} = R_s i_{qs} + \omega_s \Psi_{ds} + \frac{d\Psi_{qs}}{dt} \approx \omega_s \Psi_{ds} = |\vec{v}_s|, \tag{2.6.6}$$

$$\begin{aligned}
v_{dr} &= R_r i_{dr} + \sigma L_r \frac{di_{dr}}{dt} - \omega_{sl}\sigma L_r i_{qr}, \\
v_{qr} &= R_r i_{qr} + \sigma L_r \frac{di_{qr}}{dt} + \omega_{sl}(\frac{L_m^2}{L_s}|\vec{i}_{ms}| + \sigma L_r i_{dr}).
\end{aligned}$$

$$T_e = -n_p \frac{L_m^2}{L_s}|\vec{i}_{ms}| i_{qr}. \tag{2.6.7}$$

Voltages v_{dr} and v_{qr} obtained from the controller will be used to control the rotor voltages through a rotor side PWM converter. We rewrite the stator active and reactive powers equations as:

$$P_s = v_{ds} i_{ds} + v_{qs} i_{qs} = -|\vec{v}_s|\frac{L_m}{L_s} i_{qr}, \tag{2.6.8}$$

$$Q_s = -v_{ds} i_{qs} + v_{qs} i_{ds} = -\frac{|\vec{v}_s| L_m}{L_s} i_{dr} + \frac{|\vec{v}_s|^2}{\omega_s L_s}. \tag{2.6.9}$$

From equations (2.6.7), (2.6.8) and (2.6.9), it can be seen that the electromagnetic torque T_e and then the active power P_s only depends on the q-axis rotor current i_{qr}. The reactive power Q_s only depends on the rotor excitation current i_{dr}. Therefore, the decoupled control of active and reactive powers has been achieved in the stator-flux reference frame.

From (2.6.5) and (2.6.6), it can be seen that if the rotor resistance R_s is neglected, the stator-flux orientation is equivalent to the grid-voltage orientation in steady state. We will introduce the grid-voltage orientation in section 2.7.1.

2.7 Modeling and control of the grid-side converter

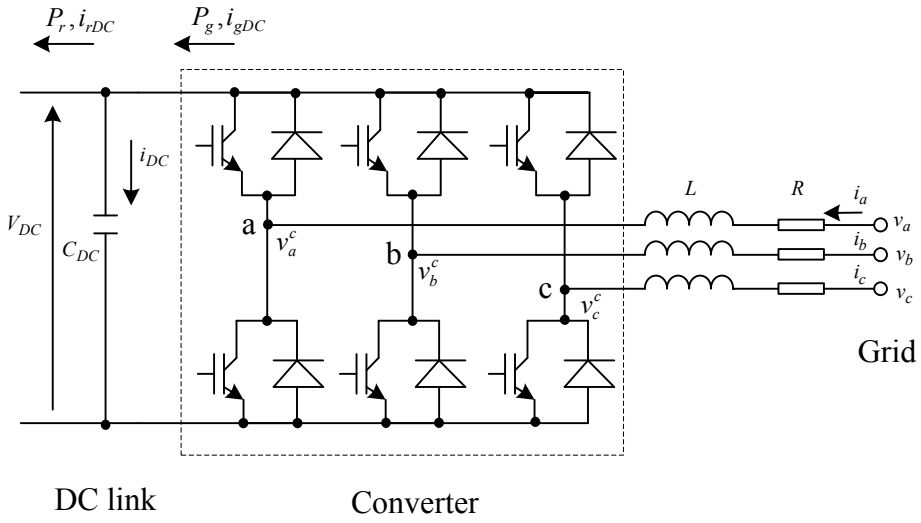

Figure 2.13: Grid-side converter

Figure 2.13 is a schematic diagram of the grid-side converter. The voltage equation across the inductors is

$$\begin{bmatrix} v_a \\ v_b \\ v_c \end{bmatrix} = R \begin{bmatrix} i_a \\ i_b \\ i_c \end{bmatrix} + L\frac{d}{dt} \begin{bmatrix} i_a \\ i_b \\ i_c \end{bmatrix} + \begin{bmatrix} v_a^c \\ v_b^c \\ v_c^c \end{bmatrix}. \tag{2.7.1}$$

Apply the abc-dq transformation to (2.7.1) , we obtain the following voltage equations in the dq frame rotating at grid voltage frequency ω_1:

$$v_d = Ri_d + L\frac{di_d}{dt} - \omega_1 L i_q + v_d^c, \tag{2.7.2}$$

$$v_q = Ri_q + L\frac{di_q}{dt} + \omega_1 L i_d + v_q^c. \tag{2.7.3}$$

We take the state variables x, external input variables w and controller output u to be the following:

$$x = \begin{bmatrix} i_d \\ i_q \end{bmatrix}, w = \begin{bmatrix} v_d \\ v_q \end{bmatrix}, u = \begin{bmatrix} v_d^c \\ v_q^c \end{bmatrix}.$$

The measured outputs are $y = \begin{bmatrix} i_d & i_q \end{bmatrix}^T$.

The state-space equations are

$$\begin{aligned} \dot{x} &= A_g x + B_{g1} w + B_{g2} u, \\ y &= C_g x, \end{aligned}$$

where

$$\begin{aligned} A_g &= \begin{bmatrix} -\frac{R}{L} & \omega_1 \\ -\omega_1 & -\frac{R}{L} \end{bmatrix}, \\ \begin{bmatrix} B_{g1} & B_{g2} \end{bmatrix} &= \left[\begin{array}{cc:cc} \frac{1}{L} & 0 & -\frac{1}{L} & 0 \\ 0 & \frac{1}{L} & 0 & -\frac{1}{L} \end{array}\right], \\ C_g &= \begin{bmatrix} 1 & 0 \\ 0 & 1 \end{bmatrix}. \end{aligned}$$

The active and reactive powers are

$$P_g = v_d i_d + v_q i_q, \tag{2.7.4}$$

$$Q_g = -v_d i_q + v_q i_d. \tag{2.7.5}$$

DC-link model

We assume the back-to-back converter is lossless and neglect the losses in the inductor resistance, then the DC-link is modeled as

$$P_{DC} = V_{DC} i_{DC}, \tag{2.7.6}$$

$$P_g = V_{DC} i_{gDC}, \tag{2.7.7}$$

$$P_r = V_{DC} i_{rDC}, \tag{2.7.8}$$

$$P_{DC} = P_g - P_r, \tag{2.7.9}$$

$$i_{DC} = i_{gDC} - i_{rDC}, \tag{2.7.10}$$

$$i_{DC} = C_{DC} \frac{dV_{DC}}{dt}. \tag{2.7.11}$$

Apply Laplace transforms to (2.7.11)

$$\hat{V}_{DC}(s) = \frac{1}{C_{DC} s} \hat{i}_{DC}(s).$$

2.7.1 Vector control of the grid-side converter

The control objective of the grid-side converter is to maintain constant DC-link voltage regardless of the changing rotor power. Vector control has been applied to enable decoupled control of the active and reactive powers flowing between the grid and the grid-side converter (see [42]). The rotating reference frame is aligned with the grid voltage, so from equation (2.5.2), we have $\theta = \theta_1$:

$$\vec{v}_{dq} = \vec{v}_{\alpha\beta} e^{-j\theta_1} = \sqrt{3} V e^{j(\theta_1 - \theta_1)} = \sqrt{3} V.$$

And we obtain

$$\begin{aligned} v_d &= \sqrt{3} V = |\vec{v}|, \\ v_q &= 0. \end{aligned}$$

The angle position of the grid voltage is computed as

$$\theta_1 = \int \omega_1 dt = tan^{-1} \frac{v_\beta}{v_\alpha},$$

where v_α and v_β are the stationary components of the grid voltage.

Then we rewrite the active and reactive power equations (2.7.4) and (2.7.5):

$$\begin{aligned} P_g &= |\vec{v}| i_d, \\ Q_g &= -|\vec{v}| i_q. \end{aligned}$$

Now it can be seen clearly that active and reactive powers are proportional to d-axis current component i_d and q-axis current component i_q respectively. Therefore we can achieve the decoupled control of the active and reactive powers through i_d and i_q.

We assume that harmonics due to the switching can be neglected, and the grid-side converter and the inductor resistance are lossless, then based on the DC-link model (2.7.6)-(2.7.11), we have

$$\begin{aligned} P_g &= V_{DC} i_{gDC} = |\vec{v}| i_d, \\ |\vec{v}| &= \frac{m_1}{2} V_{DC}, \\ i_{gDC} &= \frac{m_1}{2} i_d, \\ C_{DC} \frac{dV_{DC}}{dt} &= \frac{m_1}{2} i_d - i_{rDC}, \end{aligned} \tag{2.7.12}$$

where m_1 is the modulation depth of the grid-side PWM converter. We now consider i_{rDC} as distance, and apply Laplace transforms to (2.7.12), then we can obtain the transfer function from i_d to V_{DC}:

$$\hat{V}_{DC}(s) = \frac{m_1}{2C_{DC}s}\hat{i}_d(s).$$

The DC-link voltage controller, of PI type, has been used to guarantee constant DC-link voltage and generate reference d-axis current component i_d^{ref} to the inner control loop. We set $i_q^{ref} = 0$, because we want the grid-side reactive power to be zero. We define

$$\begin{aligned} \tilde{v}_d &= Ri_d + L\frac{di_d}{dt}, \\ \tilde{v}_q &= Ri_q + L\frac{di_q}{dt}. \end{aligned}$$

Then from the voltage equations (2.7.2) and (2.7.3), the reference converter voltages are

$$\begin{aligned} v_d^{cref} &= -\tilde{v}_d + (\omega_1 L i_q + v_d), \\ v_d^{cref} &= -\tilde{v}_q - \omega_1 L i_d, \end{aligned}$$

where $\tilde{v}_d$ and $\tilde{v}_q$ are the outputs of the inner PI current controllers.

The whole vector control scheme for the grid-side converter is shown in Figure 2.14.

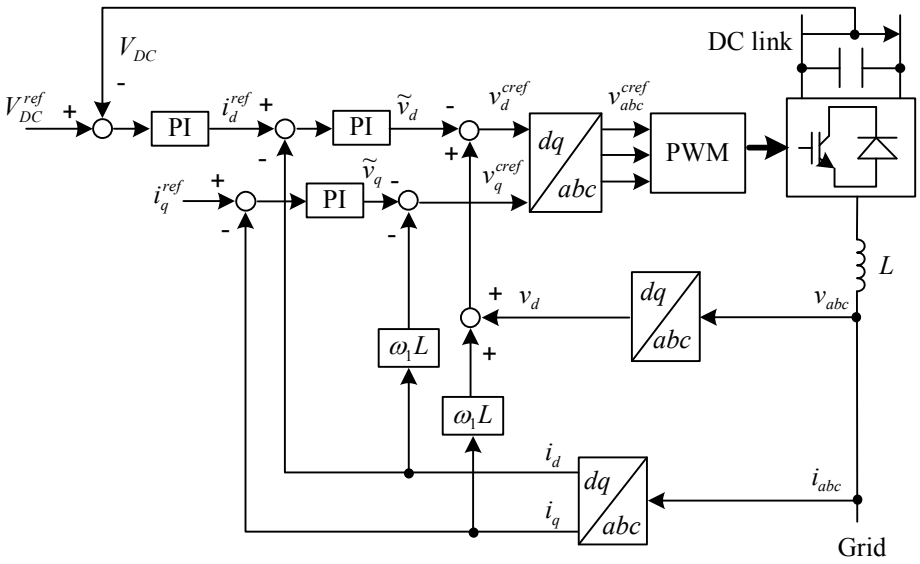

Figure 2.14: Vector control of the grid-side converter.

2.8 Modelling the drive-train dynamics

When considering mechanical models of the wind turbine, drive-train dynamics have the first priority compared with the other parts of the wind turbine. The reason, generally speaking, is that engineers would like to emphasize those parts of the dynamic structure of the wind turbine that contribute to grid integration (see [23] and [20]). Another point we need to bear in mind is that the parameters of the wind turbine system is highly concentrated, which means that the elements of the model do not necessarily have direct correspondence with the physical elements in the system (see [7]).

The rotor blades in a wind turbine are very large with lots of weight and create a significant moment of inertia into the system, especially in comparison to the generator. This inertia behaves like an inductor in an electrical circuit, storing energy when the turbine accelerates and restoring it during deceleration. It also accordingly prevents fast variations of the rotor speed on the turbine shaft, meaning that it acts like a low-pass filter (see [45] and [41]). The turbine rotor's moment of inertia is much larger than that of the generator.

2.8.1 The one-mass drive-train model

In the literature, a typical one-mass drive-train model (see Figure 2.15) consists of the inertia of both the turbine and the generator. The large turbine inertia J_T corresponds to the blades and the hub, and the small inertia J_G represents the induction generator. The equations are

$$\begin{aligned} \dot{\omega}_m &= \frac{1}{J}(T_t - T_e - b\omega_m), \\ J &= \frac{1}{n_g^2}J_T + J_G, \\ T_t &= \frac{1}{n_g}T_a, \\ \omega_m &= n_g\omega_T, \end{aligned} \tag{2.8.1}$$

where $J > 0$ is the total inertia, $b \geq 0$ is the damping coefficient, T_e is the electrical torque from the generator, T_t is the active torque from the turbine (referred to the generator side) and n_g is the gearbox ratio. We remark that in steady state (when $\dot{\omega}_m = 0$) we have the

power balance $T_a\omega_T = T_t\omega_m = T_e\omega_m + b\omega_m^2$, where $T_e\omega_m$ is the generator power and $b\omega_m^2$ is the power loss due to friction.

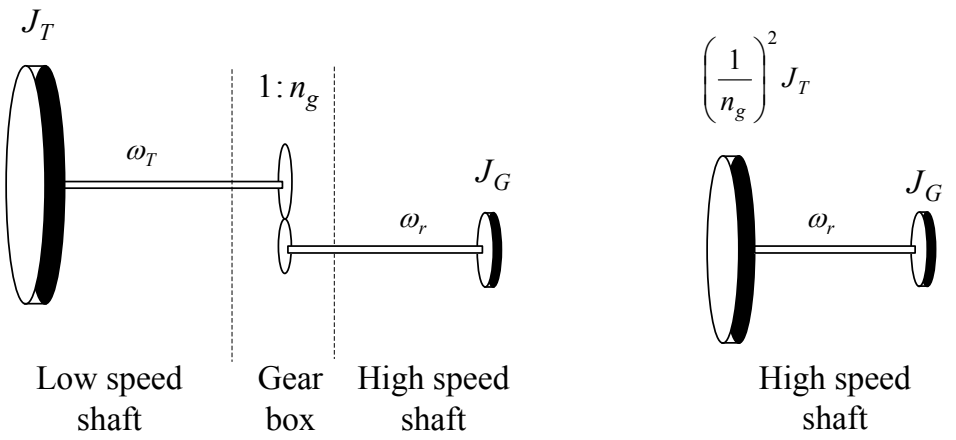

Figure 2.15: (a): A one mass model for the drive-train; (b): Another representation of the one mass model with parameters referred to the high-speed shaft.

2.8.2 The two-mass drive-train model

A two-mass drive-train model (see Figure 2.16) is often used when analysing the interaction of the wind turbine with the grid, because, due to its torsional vibrations, the drive-train has a significant influence on the power fluctuations (see [20, 36]). Torque control can help to dampen these mechanical oscillations both in region 2 (where the quadratic control law (2.3.3) has a dampening effect) and in region 3 (see Section 2.4.2).

Denoting the turbine rotor angle by θ_T and the generator rotor angle by θ_m, the equa-

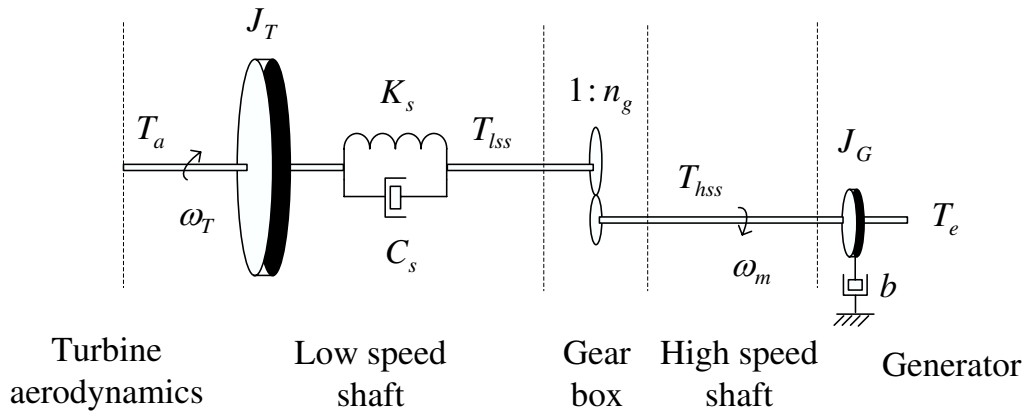

Figure 2.16: The two-mass drive-train model with gearbox.

tions are

$$\begin{aligned}
\dot{\theta}_T &= \omega_T, \\
\dot{\theta}_m &= \omega_m, \\
\theta_k &= \theta_T - \frac{\theta_m}{n_g}, \\
\dot{\omega}_T &= \frac{1}{J_T}(T_a - T_{lss}), \\
\dot{\omega}_m &= \frac{1}{J_G}(T_{hss} - T_e - b\omega_m), \\
T_{lss} &= K_s\theta_k + C_s\dot{\theta}_k, \\
&= K_s\theta_k + C_s\omega_T - \frac{C_s\omega_m}{n_g}, \\
&= n_g T_{hss}.
\end{aligned}$$

Here $K_s > 0$ is the torsional stiffness of the low speed shaft, $C_s \geq 0$ is the torsional damping of the low speed shaft, T_{lss} is the low speed shaft torque and T_{hss} is the high speed shaft torque. We remark that in steady state (when $\dot{\omega}_T = \dot{\omega}_m = 0$), we have again the power balance $T_a\omega_T = T_e\omega_m + b\omega_m^2$.

We take the state variables x, the external input variables w (disturbances) and the control input u as follows:

$$x = \begin{bmatrix} \theta_k \\ \omega_T \\ \omega_m \end{bmatrix}, \quad w = T_a, \quad u = -T_e.$$

The output variables are ω_m and ω_T, so that $y = \begin{bmatrix} \omega_T & \omega_m \end{bmatrix}^T$.

Then the $3rd$ order state-space representation is

$$\begin{aligned} \dot{x} &= Ax + B_1 w + B_2 u, \\ y &= Cx + D_1 w + D_2 u, \end{aligned} \tag{2.8.2}$$

where

$$\begin{aligned} A &= \begin{bmatrix} 0 & 1 & -\frac{1}{n_g} \\ -\frac{K_s}{J_T} & -\frac{C_s}{J_T} & \frac{C_s}{J_T n_g} \\ \frac{K_s}{J_G n_g} & \frac{C_s}{J_G n_g} & -\frac{C_s}{J_G n_g^2} - \frac{b}{J_G} \end{bmatrix}, \\ B &= \begin{bmatrix} B_1 & B_2 \end{bmatrix} = \left[\begin{array}{c|c} 0 & 0 \\ \frac{1}{J_T} & 0 \\ 0 & \frac{1}{J_G} \end{array}\right], \\ C &= \begin{bmatrix} C_1 \\ C_2 \end{bmatrix} = \left[\begin{array}{ccc} 0 & 1 & 0 \\ \hline 0 & 0 & 1 \end{array}\right], \\ D &= \begin{bmatrix} D_1 & D_2 \end{bmatrix} = \left[\begin{array}{c|c} 0 & 0 \\ 0 & 0 \end{array}\right]. \end{aligned}$$

Chapter 3

LPV control of a DFIGWT with primary grid frequency support

3.1 LPV systems

A state-space representation of a linear parameter varying (LPV) system Σ is

$$\dot{x}(t) = \mathbf{A}(\theta(t))x(t) + \mathbf{B}(\theta(t))u(t), \tag{3.1.1}$$

$$y(t) = \mathbf{C}(\theta(t))x(t) + \mathbf{D}(\theta(t))u(t). \tag{3.1.2}$$

where x is the state ($x \in \mathbb{R}^n$), u is the input vector and y is the measured output vector. In this thesis, we only have to deal with LPV systems where measurements of $\theta(t)$ are available in real time.

The following well-known result is called the bounded real lemma (BRL) and it can be found in [19] and [64].

Theorem 3.1.1. *Given a continuous-time LTI system (not necessarily minimal) with transfer function $G(s) = D + C(sI - A)^{-1}B$, the following statements are equivalent:*

- *A is stable and $\|D + C(sI - A)^{-1}B\|_\infty < \gamma$,*
- *there exists a positive definite solution X to the matrix inequality:*

$$\mathcal{B}^s_{[A,B,C,D]} := \begin{bmatrix} A^TX + XA & XB & C^T \\ B^TX & -\gamma I & D^T \\ C & D & -\gamma I \end{bmatrix} < 0,$$

where $\mathcal{B}^s_{[A,B,C,D]}$ is also called the BRL map.

The BRL can be extend to LPV systems so that sufficient conditions can be given for the transfer function of Σ at any fixed θ to have an induced L^2-norm (see definition 3.1.2) bounded by $\gamma > 0$.

Notation: $L^2[0,\infty)$ denotes the set of measurable, square integrable functions of t, $t > 0$, with norm $\|f\|_{L^2} = (\int_0^\infty |f(t)|^2 dt)^{\frac{1}{2}}$. By abuse of notation, we will also use the same notation for the space of vector-valued square integrable signals.

Definition 3.1.1. Let $\Theta \subset \mathbb{R}^s$ be a compact set of possible parameter vectors. The LPV system Σ from (3.1.1) and (3.1.2) has *quadratic $\mathcal{H}^\infty$ performance* $\gamma > 0$ if there exists a matrix $X > 0$ such that

$$\begin{bmatrix} \mathbf{A}(\theta)^T X + X\mathbf{A}(\theta) & X\mathbf{B}(\theta) & \mathbf{C}(\theta)^T \\ \mathbf{B}(\theta)^T X & -\gamma I & \mathbf{D}(\theta)^T \\ \mathbf{C}(\theta) & \mathbf{D}(\theta) & -\gamma I \end{bmatrix} < 0 \tag{3.1.3}$$

for all $\theta \in \Theta$ (see [5]).

Remark 3.1.1. The LMI (3.1.3) implies, by multiplying the matrix from the left with $z^T = [x(t)^T u(t)^T \frac{1}{\gamma} y(t)^T]$ and then multiplying it from the right with z, that

$$\frac{d}{dt}\langle Xx(t), x(t)\rangle \leq \gamma \|u(t)\|^2 - \frac{1}{\gamma}\|y(t)\|^2. \tag{3.1.4}$$

If the initial state of Σ is zero, we obtain that $\|y\|_{L^2} \leq \gamma \|u\|_{L^2}$, and this is true for any measurable function $\theta : [0,\infty) \to \Theta$.

Proof: we omit θ for simplicity, so that we write $\mathbf{A}$ instead of $\mathbf{A}(\theta)$, and similarly for $\mathbf{B}(\theta)$, $\mathbf{C}(\theta)$ and $\mathbf{D}(\theta)$. Firstly, let's compute $\frac{d}{dt}\langle Xx, x\rangle$, where $X > 0, X^T = X$.

$$\begin{aligned} \frac{d}{dt}\langle Xx, x\rangle &= \langle X(\mathbf{A}x + \mathbf{B}u), x\rangle + \langle Xx, \mathbf{A}x + \mathbf{B}u\rangle \\ &= \langle X\mathbf{A}x, x\rangle + \langle X\mathbf{B}u, x\rangle + \langle \mathbf{A}^T Xx, x\rangle + \langle x, X\mathbf{B}u\rangle \\ &= \langle (\mathbf{A}^T X + X\mathbf{A})x, x\rangle + 2Re\langle X\mathbf{B}u, x\rangle. \end{aligned} \tag{3.1.5}$$

Then let's calculate the following inner product:

$$\begin{aligned}
&\left\langle \begin{bmatrix} \mathbf{A}^TX + X\mathbf{A} & X\mathbf{B} & \mathbf{C}^T \\ \mathbf{B}^TX & -\gamma I & \mathbf{D}^T \\ \mathbf{C} & \mathbf{D} & -\gamma I \end{bmatrix} \begin{bmatrix} x \\ u \\ \frac{1}{\gamma}y \end{bmatrix}, \begin{bmatrix} x \\ u \\ \frac{1}{\gamma}y \end{bmatrix} \right\rangle &\leq 0, \\
\Leftrightarrow &\left\langle \begin{bmatrix} (\mathbf{A}^TX + X\mathbf{A})x + X\mathbf{B}u + \mathbf{C}^Ty\frac{1}{\gamma} \\ \mathbf{B}^TXx - \gamma u + \mathbf{D}^Ty\frac{1}{\gamma} \\ \mathbf{C}x + \mathbf{D}u - \gamma y\frac{1}{\gamma} \end{bmatrix}, \begin{bmatrix} x \\ u \\ \frac{1}{\gamma}y \end{bmatrix} \right\rangle &\leq 0, \\
&\Leftrightarrow \langle(\mathbf{A}^TX + X\mathbf{A})x, x\rangle + \langle X\mathbf{B}u, x\rangle + \frac{1}{\gamma}\langle y, \mathbf{C}x\rangle \\
&\qquad + \langle \mathbf{B}^TXx, u\rangle - \gamma\langle u, u\rangle + \frac{1}{\gamma}\langle y, \mathbf{D}u\rangle \\
&\qquad + \frac{1}{\gamma}\langle y, y\rangle - \frac{1}{\gamma}\langle y, y\rangle &\leq 0, \\
&\qquad (substituted \quad by (3.1.5)) \\
&\Leftrightarrow \frac{d}{dt}\langle Xx, x\rangle - \gamma\langle u, u\rangle + \frac{1}{\gamma}\langle y, y\rangle &\leq 0.
\end{aligned}$$

Rearrange the above inequality, we obtain (3.1.4).

If $X > 0, \frac{1}{\gamma} > 0$ and $(\mathbf{A}, \mathbf{C})$ observable, then the system is stable in L^2 sense (see definition 3.1.2). Indeed, taking $u = 0$, $\frac{d}{dt}\langle Xx(t), x(t)\rangle \leq -\frac{1}{\gamma}\|y\|^2$. Assuming that the initial state of Σ is 0, we integrate (3.1.4) from 0 to ∞ on both sides:

$$\begin{aligned}
\langle Xx(t), x(t)\rangle|_0^\infty &\leq \gamma\|u\|_{L^2}^2 - \frac{1}{\gamma}\|y\|_{L^2}^2, \\
\Leftrightarrow \|y\|_{L^2} &\leq \gamma\|u\|_{L^2}.
\end{aligned}$$

We conclude that the LMI (3.1.3) is true for any measurable function $\theta : [0, \infty) \to \Theta$. Therefore, even as θ changes and no matter how fast it changes, we always have (3.1.4).

□

Definition 3.1.2 (*Induced* L^2*-norm*). For each $\theta \in \Theta$, let G_θ be the transfer function of the stable system obtained by taking $\theta(t) = \theta$ in (3.1.1) and (3.1.2). The induced L^2-norm of the family $G = (G_\theta)$ is defined by

$$\|G\| = \sup_{\theta\in\Theta} \|G_\theta\|_\infty,$$

where $\|G_\theta\|_\infty = \sup_{Re(s)>0} \|G_\theta(s)\|$.

It follows from *Remark* 3.1.1 that, if Σ has *quadratic $\mathcal{H}^\infty$ performance* $\gamma > 0$, then $\|G\| \leq \gamma$.

The following definitions and theorems are taken from [5].

Definition 3.1.3 (*Matrix polytope*). A *matrix polytope* is defined as the convex hull of a finite number of matrices N_i with the same dimensions.

$$Co\{N_i, \quad i = 1, ..., r\} := \{\sum_{i=1}^{r} \alpha_i N_i : \quad \alpha_i \geq 0, \quad \sum_{i=1}^{r} \alpha_i = 1\}. \tag{3.1.6}$$

Definition 3.1.4 (*Polytopic LPV systems*). An LPV system is called *ploytopic* when it can be represented by state-space matrices $A(\theta)$, $B(\theta)$, $C(\theta)$ and $D(\theta)$, where the parameter vector $\theta(t)$ ranges over a fixed polytope Θ of vertices $\theta_1, \theta_2, ..., \theta_r$, that is

$$\theta(t) \in \Theta := Co\{\theta_i, \quad i = 1, ..., r\}. \tag{3.1.7}$$

The dependence of $A(\cdot)$, $B(\cdot)$, $C(\cdot)$ and $D(\cdot)$ on $\theta(t)$ is affine.

Theorem 3.1.2 (*Vertex property*). *Consider a polytopic LPV plant described by the* ***G*** *with*

$$\begin{pmatrix} A(\theta) & B(\theta) \\ C(\theta) & D(\theta) \end{pmatrix} \in \mathcal{P} := Co\left\{ \begin{pmatrix} A_i & B_i \\ C_i & D_i \end{pmatrix}, \quad i = 1, 2, ..., r \right\},$$

The following statements are equivalent:

- *there exists a matrix $X > 0$ such that, for all $\begin{pmatrix} A(\theta) & B(\theta) \\ C(\theta) & D(\theta) \end{pmatrix} \in \mathcal{P}$,*

$$\mathcal{B}^s_{[A(\theta),B(\theta),C(\theta),D(\theta)]}(X, \gamma) < 0. \tag{3.1.8}$$

- *there exists $X > 0$ satisfying the set of LMIs*

$$\mathcal{B}^s_{[A_i,B_i,C_i,D_i]}(X, \gamma) < 0, \quad i = 1, 2, ..., r. \tag{3.1.9}$$

The following definition and theorem can be found in [4], [13] and [46].

Definition 3.1.5 (*LMI Region*). A subset $\mathcal{D}$ of complex plane is called an *LMI region* if there exist a symmetric matrix $\lambda = [\lambda_{ik}]_{1 \leq i,k \leq m} \in \mathbf{R}^{m \times m}$ and a fixed real matrix $\mu = [\mu_{ik}]_{1 \leq i,k \leq m} \in \mathbf{R}^{m \times m}$ such that

$$\mathcal{D} = \{z \in \mathbf{C} : [\lambda_{ik} + z\mu_{ik} + \bar{z}\mu_{ki}]_{1 \leq i,k \leq m} < 0\}$$

Note that LMI regions are convex and symmetric with respect to the real axis. Special cases include vertical strips, disks, horizontal strips, conic sectors, ellipsoids, domains bordered by parabolas and their arbitrary intersections.

Theorem 3.1.3 ($\mathcal{D}$-stable). *The matrix A has all its eigenvalues in the LMI region $\mathcal{D} = \{z \in \mathbf{C} : [\lambda_{ik} + z\mu_{ik} + \bar{z}\mu_{ki}]_{1\leq i,k\leq m} < 0\}$, ($A$ is then called $\mathcal{D}$-stable), if and only if there exists a symmetric matrix $X > 0$ such that*

$$[\lambda_{ik}X + \mu_{ik}A^T X + \mu_{ki}XA]_{1\leq i,k\leq m} < 0,$$

where "< 0" stands for negative definite.

3.2 Computation of the self-scheduled LPV controller

Consider an open-loop LPV system **P** described by

$$\begin{aligned}
\dot{x}(t) &= \mathbf{A}(\theta(t))x(t) + \mathbf{B}_1(\theta(t))w(t) + \mathbf{B}_2(\theta(t))u(t),\\
z(t) &= \mathbf{C}_1(\theta(t))x(t) + \mathbf{D}_{11}(\theta(t))w(t) + \mathbf{D}_{12}(\theta(t))u(t),\\
y(t) &= \mathbf{C}_2(\theta(t))x(t) + \mathbf{D}_{21}(\theta(t))w(t),
\end{aligned}$$

where y denotes the measured outputs, z the controlled outputs , w the reference and disturbance inputs and u the control inputs. The LPV synthesis problem consists in finding a controller $K(\cdot)$ described by

$$\begin{aligned}
\dot{x}_k(t) &= \mathbf{A}_K(\theta(t))x_k(t) + \mathbf{B}_K(\theta(t))y(t),\\
u(t) &= \mathbf{C}_K(\theta(t))x_k(t),
\end{aligned}$$

such that the closed-loop system (with input w and output z) satisfies (3.1.3) for any measurable function $\theta : [0, \infty) \to \Theta$.

The computation of the LPV controller described below (also used in this thesis) could potentially have some conservatism in the case of slow parametric variations. In [16], a less conservative LMI-based technique has been proposed, which is an extension of the notions of quadratic stability and performance where the fixed quadratic Lyapunov function is replaced by a Lyapunov function with affine dependence on the uncertain parameters.

A self-scheduled controller implies that the controller can update itself online by incorporating the parameter measurements $\theta(t)$, so that the real-time plant dynamics can be taken into account. Then stability and certain performances bounds are guaranteed along all the trajectories of $\theta(t)$.

We assume that the parameter dependence of the plant **P** is affine and Θ is a polytope with vertices $\theta_j, j = 1, 2, ..., r$. According to the results in [4] and [5], one LPV controller $K(\cdot)$ can be computed through the following steps:

- *Offline computations*: compute the vertex controllers $K_j = (A_{K_j}, B_{K_j}, C_{K_j}, 0)$, $(1 \leq j \leq r)$ as follows:

  i. Solve the following set of LMIs

$$\begin{bmatrix} X\mathbf{A}_j + \hat{B}_{K_j}\mathbf{C}_{2_j} + \star & \star & \star & \star \\ \hat{A}_{K_j}^T + \mathbf{A}_j & \mathbf{A}_j Y + \mathbf{B}_{2_j}\hat{C}_{K_j} + \star & \star & \star \\ (X\mathbf{B}_{1_j} + \hat{B}_{K_j}\mathbf{D}_{21_j})^T & \mathbf{B}_{1_j}^T & -\gamma I & \star \\ \mathbf{C}_{1_j} & \mathbf{C}_{1_j} Y + \mathbf{D}_{12_j}\hat{C}_{K_j} & \mathbf{D}_{11_j} & -\gamma I \end{bmatrix} < 0, \tag{3.2.1}$$

  together with

$$\begin{bmatrix} X & I \\ I & Y \end{bmatrix} > 0, \tag{3.2.2}$$

  where $\star$ denotes terms whose expressions follow from the requirement that the matrix is self-adjoint. This step gives $(\hat{A}_{K_j}, \hat{B}_{K_j}, \hat{C}_{K_j})$ and symmetric matrices X and Y.

  ii. Solve for N, M based on the singular value decomposition (SVD) of $I - XY$

$$I - XY = NM^T. \tag{3.2.3}$$

  iii. Compute the A_{K_j},B_{K_j} and C_{K_j} with

$$A_{K_j} = N^{-1}(\hat{A}_{K_j} - X\mathbf{A}_j Y - \hat{B}_{K_j}\mathbf{C}_{2_j} Y - X\mathbf{B}_{2_j}\hat{C}_{K_j})M^{-T}, \tag{3.2.4}$$

$$B_{K_j} = N^{-1}\hat{B}_{K_j}, \tag{3.2.5}$$

$$C_{K_j} = \hat{C}_{K_j} M^{-T}. \tag{3.2.6}$$

- *Online computations*:

i. Measure $\theta(t)$ and compute its *convex decomposition*:

$$\theta(t) = \alpha_1\theta_1 + \alpha_2\theta_2 + ... + \alpha_r\theta_r, \tag{3.2.7}$$

where $\sum_{j=1}^{r} \alpha_j = 1$, $\alpha_j \geq 0$. Note that $\alpha_1, ..., \alpha_r$ are functions of θ.

ii. Compute the state-space matrices of the controller $K(\cdot)$ as a *convex combination* of the vertex controllers:

$$\left[\begin{array}{cc} \mathbf{A}_K & \mathbf{B}_K \\ \mathbf{C}_K & 0 \end{array} \right](\theta) = \sum_{j=1}^{r} \alpha_j \left[\begin{array}{cc} A_{K_j} & B_{K_j} \\ C_{K_j} & 0 \end{array} \right]. \tag{3.2.8}$$

Note that the online computations (3.2.7) and (3.2.8) are very cheap.

3.3 Controller design with pole placement constraints

The resulting controller from Section 3.2 may have some poles whose real parts are far from the imaginary axis. Those poles, the so called *fast modes*, would complicate the hardware implementation of the controller (see [7]). This drawback can be fixed by confining the closed-loop poles of the underlying vertex LTI systems (at fixed θ) to a certain region $\mathcal{D} \in \mathbf{C}$. The LMIs (3.2.1) and (3.2.2) must then be complemented with

$$\left[\lambda_{ik} \left[\begin{array}{cc} X & I \\ I & Y \end{array} \right] + \mu_{ik}\mathbf{T} + \mu_{ki}\mathbf{T}^T \right]_{1 \leq i,k \leq m} < 0,$$

where

$$\mathbf{T} = \left[\begin{array}{cc} A_jY + B_{2_j}\hat{C}_{K_j} & A_j \\ \hat{A}_{K_j} & XA_j + \hat{B}_{K_j}C_{2_j} \end{array} \right].$$

The data λ_{ik} and μ_{ik} defines the geometry of the region $\mathcal{D}$. For example, if we want the region $\mathcal{D}$ to be the plane where $Res < -10$, we simply choose $\lambda = 20$ and $\mu = 1$. Then the new controller state-space matrices $\mathbf{A}_K$, $\mathbf{B}_K$ and $\mathbf{C}_K$ can be obtained with the computations of (3.2.3)-(3.2.8).

3.4 Controller reduction based on the truncation of fast modes

The design procedure from Section 3.2 gives a self-scheduled LPV controller of the same order as the plant. However, often some of the modes are stable and very high compared

to the frequency range of interest. In this case, these modes should be eliminated from the controller by model reduction. Very sophisticated model-reduction techniques are known for individual LTI systems, see for example [18] and [64]. For LPV systems these techniques are not practical, because they would require us to perform the model reduction at each individual point $\theta \in \Theta$. Here we propose a model-reduction procedure which can be applied to self-scheduled LPV controllers and only requires the designer to compute a reduced controller in each vertex of Θ.

To simplify the notation of vertex controllers, we write A_j instead of A_{K_j}, and similarly for B_j and C_j.

Controller reduction procedure: Assume that the matrices for $K_j(j = 1, ..., r)$ can be partitioned compatibly using a transformation matrix T (the same for all vertices):

$$\breve{K}_j \stackrel{s}{=} \left[\begin{array}{c|c} T^{-1}A_jT & T^{-1}B_j \\ \hline C_jT & 0 \end{array}\right] = \left[\begin{array}{cc|c} A_{j11} & A_{j12} & B_{j1} \\ A_{j21} & A_{j22} & B_{j2} \\ \hline C_{j1} & C_{j2} & 0 \end{array}\right], \tag{3.4.1}$$

where all of the eigenvalues of A_{j22} are large compared to the frequency range of interest. Then we rewrite the LPV controller from (3.2.8) in the new coordinates:

$$\left[\begin{array}{cc|c} \mathbf{A}_{K11} & \mathbf{A}_{K12} & \mathbf{B}_{K1} \\ \mathbf{A}_{K21} & \mathbf{A}_{K22} & \mathbf{B}_{K2} \\ \hline \mathbf{C}_{K1} & \mathbf{C}_{K2} & 0 \end{array}\right](\theta) = \sum_{j=1}^{r} \alpha_j \breve{K}_j. \tag{3.4.2}$$

The reduced order controller $K^r = (\tilde{A}, \tilde{B}, \tilde{C}, \tilde{D})$ is computed as follows:

$$\tilde{A} = \mathbf{A}_{K11} - \mathbf{A}_{K12}\mathbf{A}_{K22}^{-1}\mathbf{A}_{K21}, \tag{3.4.3}$$

$$\tilde{B} = \mathbf{B}_{K1} - \mathbf{A}_{K12}\mathbf{A}_{K22}^{-1}\mathbf{B}_{K2}, \tag{3.4.4}$$

$$\tilde{C} = \mathbf{C}_{K1} - \mathbf{C}_{K2}\mathbf{A}_{K22}^{-1}\mathbf{A}_{K21}, \tag{3.4.5}$$

$$\tilde{D} = -\mathbf{C}_{K2}\mathbf{A}_{K22}^{-1}\mathbf{B}_{K2}. \tag{3.4.6}$$

Justification: We omit the subscript K for simplicity. Consider the transfer function $K(s)$ of the controller for any fixed θ. For small $|s|$ (in the frequency range of interest), $A_{22} - sI \approx A_{22}$. Based on Schur's formula (see [64]), we have the following approxima-

tion: Define $\mathcal{A} = \begin{bmatrix} A_{11} & A_{12} \\ A_{21} & A_{22} \end{bmatrix}$, $\tilde{A} = A_{11} - A_{12}A_{22}^{-1}A_{21}$ and $\mathcal{S} = \tilde{A} - sI$, then

$$\begin{aligned} &(\mathcal{A} - sI)^{-1} \\ &\approx \begin{bmatrix} \mathcal{S}^{-1} & -\mathcal{S}^{-1}A_{12}A_{22}^{-1} \\ -A_{22}^{-1}A_{21}\mathcal{S}^{-1} & A_{22}^{-1} + A_{22}^{-1}A_{21}\mathcal{S}^{-1}A_{12}A_{22}^{-1} \end{bmatrix}, \\ &= \begin{bmatrix} I \\ -A_{22}^{-1}A_{21} \end{bmatrix} \mathcal{S}^{-1} \begin{bmatrix} I & -A_{12}A_{22}^{-1} \end{bmatrix} + \begin{bmatrix} 0 & 0 \\ 0 & A_{22}^{-1} \end{bmatrix}. \end{aligned} \tag{3.4.7}$$

For any fixed θ, the transfer function of the controller

$$K(s) = -\begin{bmatrix} C_1 & C_2 \end{bmatrix} (\mathcal{A} - sI)^{-1} \begin{bmatrix} B_1 \\ B_2 \end{bmatrix}, \tag{3.4.8}$$

can be approximated, according to (3.4.7), by

$$K^r(s) = \tilde{C}(sI - \tilde{A})^{-1}\tilde{B} + \tilde{D}. \tag{3.4.9}$$

□

3.5 LPV model for the DFIG

Based on a $4th$ order nonlinear DFIG model (see Vas [54] or Section 2.6.3), we take the state variables x as the stator and rotor currents in the dq frame. The external input variables w (disturbances and references) are stator voltages and reference rotor currents, also in the dq frame. The controller output u consists of rotor voltages. Thus

$$x = \begin{bmatrix} i_{ds} \\ i_{qs} \\ i_{dr} \\ i_{qr} \end{bmatrix}, \quad w = \begin{bmatrix} v_{ds} \\ v_{qs} \\ i_{dr}^{ref} \\ i_{qr}^{ref} \end{bmatrix}, \quad u = \begin{bmatrix} v_{dr} \\ v_{qr} \end{bmatrix}.$$

The controlled outputs and measured outputs are

$$z = \begin{bmatrix} e_{idr} \\ e_{iqr} \end{bmatrix}, \qquad y = \begin{bmatrix} i_{ds} \\ i_{qs} \\ i_{dr} \\ i_{qr} \end{bmatrix},$$

where e_{idr} = i_{dr}^{ref} - i_{dr} and e_{iqr} = i_{qr}^{ref} - i_{qr}.

Recalling the structure of the open-loop LPV system $\mathbf{P}$ described in Section 3.2, we choose the parameter vector $\theta = \begin{bmatrix} \omega_s & \omega_r \end{bmatrix}^T$, where ω_s is the synchronous speed and ω_r

is the generator electrical angular speed. Note that $\omega_s = 2\pi f_g/n_p$, where f_g is the grid frequency and n_p is the number of pole pairs. Then the state-space equations of the DFIG model are

$$\begin{aligned} \dot{x} &= (A_0 + \omega_s A_1 + \omega_r A_2)x + B_1 w + B_2 u, \\ z &= C_1 x + D_{11} w + D_{12} u, \\ y &= C_2 x + D_{21} w + D_{22} u, \end{aligned} \tag{3.5.1}$$

where

$$A_0 = \begin{bmatrix} -aL_rR_s & 0 & aL_mR_r & 0 \\ 0 & -aL_rR_s & 0 & aL_mR_r \\ aL_mR_s & 0 & -aL_sR_r & 0 \\ 0 & aL_mR_s & 0 & -aL_sR_r \end{bmatrix},$$

$$A_1 = \begin{bmatrix} 0 & 1 & 0 & 0 \\ -1 & 0 & 0 & 0 \\ 0 & 0 & 0 & 1 \\ 0 & 0 & -1 & 0 \end{bmatrix},$$

$$A_2 = \begin{bmatrix} 0 & aL_m^2 & 0 & aL_rL_m \\ -aL_m^2 & 0 & -aL_rL_m & 0 \\ 0 & -aL_sL_m & 0 & -aL_sL_r \\ aL_sL_m & 0 & aL_sL_r & 0 \end{bmatrix},$$

$$B_1 = \begin{bmatrix} aL_r & 0 & 0 & 0 \\ 0 & aL_r & 0 & 0 \\ -aL_m & 0 & 0 & 0 \\ 0 & -aL_m & 0 & 0 \end{bmatrix},$$

$$B_2 = \begin{bmatrix} -aL_m & 0 \\ 0 & -aL_m \\ aL_s & 0 \\ 0 & aL_s \end{bmatrix},$$

$$\begin{bmatrix} C_1 \\ C_2 \end{bmatrix} = \left[\begin{array}{cccc} 0 & 0 & -1 & 0 \\ 0 & 0 & 0 & -1 \\ \hline \multicolumn{4}{c}{\mathbf{I}_{4\times4}} \end{array}\right],$$

$$\begin{bmatrix} D_{11} & D_{12} \\ D_{21} & D_{22} \end{bmatrix} = \left[\begin{array}{cccc:c} 0 & 0 & 1 & 0 & \mathbf{0}_{2\times2} \\ 0 & 0 & 0 & 1 & \\ \hdashline \multicolumn{4}{c:}{\mathbf{0}_{4\times4}} & \mathbf{0}_{4\times2} \end{array}\right].$$

We define $a = \frac{1}{L_sL_r - L_m^2}$.

Note that the above state-space model (3.5.1) is obtained based on the complete 4th-order DFIG model described in Section 2.6.3. Whereas the purpose of presenting a DFIG

model in the stator-flux reference frame in Section 2.6.4 is to show that decoupled control of stator active and reactive powers can be achieved by rotor current control, which explains the motivation of adding i_{dr}^{ref} and i_{qr}^{ref} to the external input vector w.

3.6 Two-loop control systems design

As shown in Figure 1.1, there are basically two control loops embedded hierarchically in the control systems for the DFIGWT, namely the inner current control loop and the outer electrical torque control loop. In the inner loop, the control of the grid-side converter will not be discussed in this paper, but the detailed description can be found in Pena *et al.* [42].

3.6.1 Electrical torque control with frequency support

Quadratic torque controller

We assume that the C_p curves are known based on field measurements. In the lower to medium wind speed region (or region 2), the control objective is to maximize energy production, which can be achieved by $i)$ keeping the pitch angle β to be the optimal value corresponding to the maximum possible C_p^{max} and $ii)$ controlling the generator rotor speed such that $\lambda = \lambda_{opt}$. In this paper, we adopt the standard quadratic torque control method, see [42] and Johnson *et al.* [31].

The primary goal in region 3 (above the rated wind speed, see Figure 2.3(a)) is to maintain the generated power at the rated value. This is done by maintaining a constant electrical torque (using the rotor current controller and the rotor-side converter) and regulating the turbine speed by pitch control. Therefore the reference electrical torque u_1 over both regions 2 and 3 is

$$u_1 = \begin{cases} K^{opt}\omega_r^2 & region\ 2, \\ T_e^{rated} & region\ 3, \end{cases} \tag{3.6.1}$$

where $K^{opt} = \frac{1}{2}\frac{\rho\pi R_w^5 C_p^{max}}{\lambda_{opt}^3 n_g^3 n_p^2}$, see (2.3.3).

Frequency support controller

With conventional generation, in terms of time horizon, power/frequency control is classified as primary (less than 30 seconds after a major frequency drop), secondary (30 seconds to 30 minutes) and tertiary, see Kundur [34]. Wind turbines are able to contribute to the primary control by releasing the stored kinetic energy over the critical first few seconds following loss of network generation. A wind farm can also contribute to the secondary control, when the power/frequency reference is imposed by the system operator at any time. See [22] for a detailed description of different control functions in modern wind farms, such as balance control, delta control, power ramp rate limiter and active frequency control. In this paper, the proposed frequency support controller has been designed and tested to meet the primary control requirement. However, it can also be easily extended for the secondary control purpose.

When the deviation of the grid frequency f_g from the nominal value 50Hz is beyond $\pm 1\%$, a wind turbine needs to produce more or less active power in order to compensate for the deviant behavior in f_g. This can be achieved by a step change in the reference torque u_2, produced by the proportional controller P as shown in Figure 3.1. This step signal u_2 will be added to the output of the quadratic torque controller u_1. Then the overall control signal $u_3 = u_1 + u_2$ will be injected into the speed protection block, which is essentially a switch, deciding whether u_1 or u_3 will be the reference electrical torque T_e^{ref} based on the value of ω_r.

Speed protection block: Suppose that $f_g \leq$49.5Hz has been detected. Then the frequency support controller generates a positive step signal u_2 and T_e^{ref} is set to be u_3 to extract the kinetic energy stored in the turbine blades. The generator speed ω_r will then decrease following this sudden excess demand of active power, but before it would drop below a minimal allowable value, T_e^{ref} will be switched back to u_1. This will prevent reaching near standstill from where it would take a long time to return to normal operation (because of low C_p).

Suppose that f_g is oscillating around 49.5Hz, a relay block would then be needed to prevent u_2 from oscillating accordingly. The on/off behavior of the relay1 block is shown in Figure 3.2. The grid frequency can rise to 52Hz and fall as low as 47Hz under

exceptional circumstances. Suppose that f_g <47Hz has been detected, then the wind turbine would have to be shut down. The relay2 block (see Figure 3.2) has been used to prevent oscillations in the shut down signal r_2.

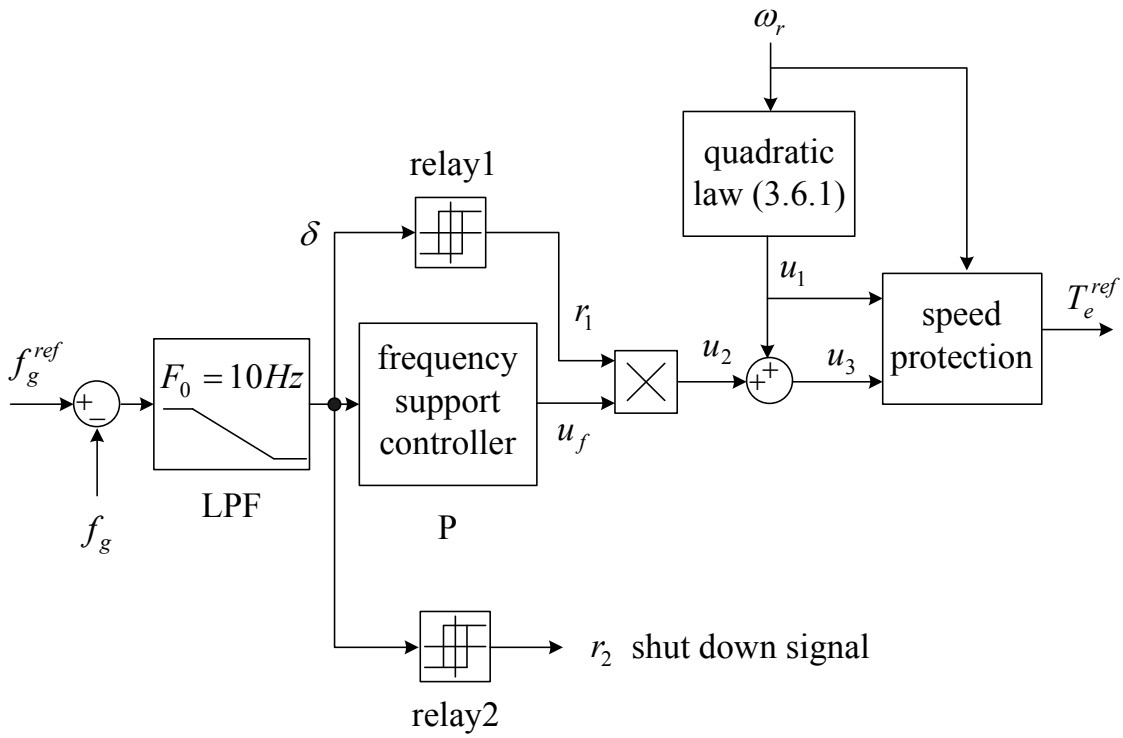

Figure 3.1: Block diagram of the electrical torque controller. The quadratic torque controller has been shown in (3.6.1). The speed protection block is essentially a switch. When ω_r drops below the lower bound, $T_e^{ref} = u_1$, otherwise $T_e^{ref} = u_3$. LPF stands for low pass filter. The on/off states of the relay blocks are shown in Figure 3.2.

Reference rotor current calculation

A widely-recognized vector control scheme for DFIG is under the stator-flux reference frame, where a decoupled control between the electrical torque and the rotor excitation current is obtained, see [42] and [54], and it can be shown that the electrical torque is proportional to the q-component of the rotor current:

$$\begin{aligned} T_e &= -n_p \frac{L_m^2}{L_s} |\vec{i}_{ms}| i_{qr}, \\ |\vec{i}_{ms}| &= \frac{|\vec{v}_s|}{\omega_s L_m}, \end{aligned} \tag{3.6.2}$$

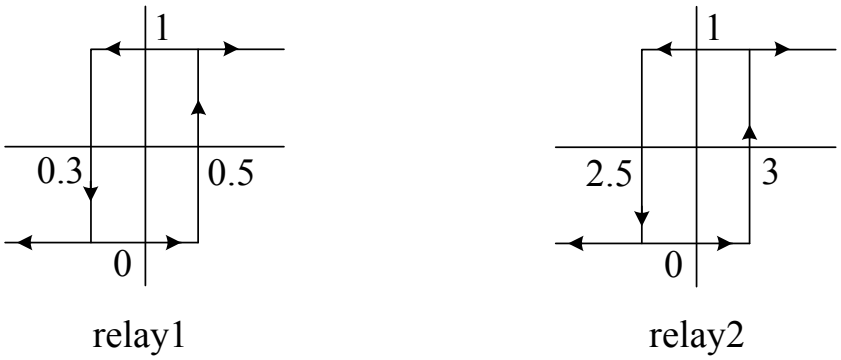

Figure 3.2: The specification of the relay blocks from Figure 3.1. The horizontal axis is the filtered frequency deviation signal δ. The relay1 block is used to prevent oscillations in u_2. The relay2 block is used to prevent oscillations in the shut down signal r_2.

where i_{ms} is the stator magnetizing current. One of the key assumptions of this decoupling is that the grid frequency f_g has to be constant, i.e. the synchronous speed ω_s is constant. Therefore we know that (3.6.2) would not be true when f_g changes. Here we derive a more accurate reference rotor current calculation which can be used regardless of the variation of f_g. Recall that the electrical torque is:

$$T_e = n_p L_m (i_{qs} i_{dr} - i_{ds} i_{qr}). \tag{3.6.3}$$

We assume that $i_{dr} = i_{dr}^{ref}$. This is a valid assumption, because i_{dr}^{ref} should be given by an outer-loop controller for grid integration (see Figure 1.1), which is much slower compared to the inner electrical control loop. Therefore, rearrange (3.6.3), we have

$$i_{qr}^{ref} = \frac{c i_{qs} i_{dr}^{ref} - T_e^{ref}}{c i_{ds}}, \tag{3.6.4}$$

where $c = \frac{3}{2} n_p L_m$ and the stator currents (i_{ds}, i_{qs}) are measurable. Once T_e^{ref} is known (see Figure 3.1), we can easily compute i_{qr}^{ref} using (3.6.4) and send it to the inner-loop LPV current controller.

3.6.2 Self-scheduled LPV current control loop

Based on the LPV model of the DFIG shown in Section 3.5 and the 4 vertexes defined by the upper and lower bounds of ω_s and ω_r, we denote the A matrix at these vertexes by

$$\begin{aligned}
\tilde{A}_1 &= A_0 + \omega_s^{min} A_1 + \omega_r^{min} A_2, \\
\tilde{A}_2 &= A_0 + \omega_s^{max} A_1 + \omega_r^{min} A_2, \\
\tilde{A}_3 &= A_0 + \omega_s^{min} A_1 + \omega_r^{max} A_2, \\
\tilde{A}_4 &= A_0 + \omega_s^{max} A_1 + \omega_r^{max} A_2.
\end{aligned}$$

At these 4 vertexes, the extended plant $\widetilde{\mathbf{P}}$, shown in Figure 3.3, can be represented (see Appendix A.1) as

$$\widetilde{\mathbf{P}}_j = \left[\begin{array}{ccc|c:c} \tilde{A}_j & 0 & 0 & B_1 & B_2 \\ B_w C_1 & A_w & 0 & B_w D_{11} & B_w D_{12} \\ 0 & 0 & A_u & 0 & B_u \\ \hline D_w C_1 & C_w & 0 & D_w D_{11} & D_w D_{12} \\ 0 & 0 & C_u & 0 & D_u \\ \hdashline C_1 & 0 & 0 & D_{11} & D_{12} \\ C_2 & 0 & 0 & D_{21} & D_{22} \end{array}\right], j = 1, ..., 4. \tag{3.6.5}$$

Once a measurement of $\omega_s(t)$ and $\omega_r(t)$ is available at time t, after performing the convex decomposition (3.2.7), we have that the LPV form of the extended plant admits the following polytopic state-space representation:

$$\widetilde{\mathbf{P}}(t) = \alpha_1 \widetilde{\mathbf{P}}_1 + \alpha_2 \widetilde{\mathbf{P}}_2 + \alpha_3 \widetilde{\mathbf{P}}_3 + \alpha_4 \widetilde{\mathbf{P}}_4,$$

where $\sum_{j=1}^{4} \alpha_j = 1$, $\alpha_j \geq 0$.

The filters W_1 and W_u are used to shape the output sensitivity function $\mathbf{T}_{zw}$ as (3.6.6) (the transfer function from w to z for any fixed $\theta = \left[\begin{array}{cc} \omega_s & \omega_r \end{array}\right]^T$, see Appendix A.2) and the control effort respectively.

$$\mathbf{T}_{zw} = \left[\begin{array}{cc|c} A_0 + \omega_s A_1 + \omega_r A_2 & B_2 \mathbf{C}_K & B_1 \\ \mathbf{B}_{K1} C_1 + \mathbf{B}_{K2} C_2 & \mathbf{A}_K + (\mathbf{B}_{K1} D_{12} + \mathbf{B}_{K2} D_{22}) \mathbf{C}_K & \mathbf{B}_{K1} D_{11} + \mathbf{B}_{K2} D_{21} \\ \hline C_1 & D_{12} \mathbf{C}_K & D_{11} \end{array}\right]. \tag{3.6.6}$$

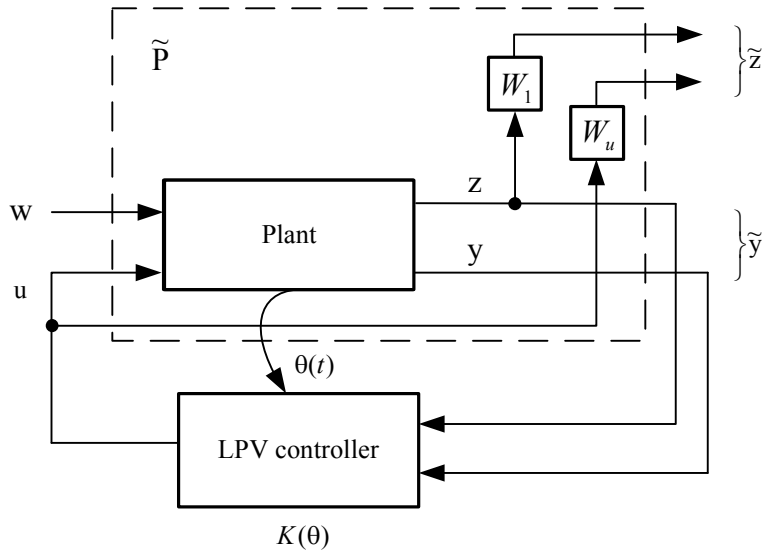

Figure 3.3: Formulation of the LPV control problem. This block diagram represents the extended plant $\widetilde{\mathbf{P}}$ for the LPV controller synthesis, which consists of the original LPV model of the DFIG (3.5.1) together with the filters W_1 and W_u. The parameter vector $\theta = [\omega_s \quad \omega_r]^T$.

1. ***Robust tracking requirements-$\mathcal{S}$***

   For robust tracking, we need to consider the sensitivity $\mathcal{S}$ (here $\mathbf{T}_{zw}$) of the system such that:

$$\bar{\sigma}(W_1(j\omega)\mathbf{T}_{zw}(j\omega)) < 1, \forall\omega \tag{3.6.7}$$

   W_1(s) is a stable minimum phase low-pass filter:

$$W_1(s) = \begin{bmatrix} w_1(s) & 0 \\ 0 & w_1(s) \end{bmatrix} = \begin{bmatrix} \frac{k_l}{s+\omega_l} & 0 \\ 0 & \frac{k_l}{s+\omega_l} \end{bmatrix}.$$

2. ***Control effort requirements-$K\mathcal{S}$***

   To implement a controller in practice, its bandwidth should not be too high. Otherwise, it may lead to energy consumption and high cost [28]. To make sure a limited bandwidth, we require:

$$\bar{\sigma}(W_u(j\omega)K(j\omega)\mathcal{S}(j\omega)) < 1, \forall\omega \tag{3.6.8}$$

where K denotes the controller, $W_u(s)$ is a stable minimum phase high-pass filter

$$W_u(s) = \begin{bmatrix} w_u(s) & 0 \\ 0 & w_u(s) \end{bmatrix} = \begin{bmatrix} \frac{k_h s}{s+\omega_h} & 0 \\ 0 & \frac{k_h s}{s+\omega_h} \end{bmatrix}.$$

The closed-loop system should not be sensitive to the high frequency components in the reference rotor currents, so ω_l should not be too large. We choose $\omega_l = 100rad/s$. The bandwidth of the LPV controller is limited by ω_h. We take $\omega_h = 100rad/s$. The parameters k_l and k_h are chosen based on trial and error. The larger the k_l, the smaller the current tracking errors. But a very large k_l would cause spikes in the rotor voltages. So we take $k_l = 4 \times 10^4$. The smaller the k_h, the better the current tracking performance. But if k_h is too small, the controller design algorithm would tend to neglect the existence of the filter W_u. So we take $k_h = 10^{-3}$.

3.7 Simulation results

The simulations have been carried out using Matlab/Simulink. The reduced order LPV controller has been tested on a nonlinear $4th$ order DFIG model (described in Section 2.6.3) with a two mass drive-train (see Section 2.8.2). As shown in Figure 3.4, the Simulink implementation of the LPV controller is based on a time varying state-space block, which is available online from the Mathworks. This block takes two kinds of inputs, namely, the system input and the gain matrix. The former consists of the rotor current tracking errors (e_{idr}, e_{iqr}), stator and rotor currents ($i_{ds}, i_{qs}, i_{dr}, i_{qr}$). The latter contains the system matrices of the reduced controller. The calculation of these system matrices has been shown in Sections 3.2 and 3.4. Here we provide a more detailed description:

Offline: the *Robust Control Toolbox* in Matlab has been used to solve the LMIs (3.2.1) and (3.2.2). Alternatively, the Matlab routine ***hinfgs*** may be used to compute the vertex controllers $K_j (j = 1, ..., 4)$.

Online: to compute the reduced controller K^r at time t when a measurement $\theta(t) = \begin{bmatrix} \omega_s(t) & \omega_r(t) \end{bmatrix}^T$ is available, we need to partition the realization for K_j compatibly as (3.4.1) using a transformation matrix T (the same for all of the 4 vertices). This T matrix

can be obtained by applying the Schur decomposition to the A matrix of any K_j. After we obtain the new vertex controllers $\breve{K}_j$, combining α_j from the convex decomposition block, we are able to perform convex combination (3.4.2) and compute the system matrices $(\tilde{A}, \tilde{B}, \tilde{C}, \tilde{D})$ of K^r (see Section 3.4). Here $j = 1, ..., 4$. Note that the outputs of the controller reduction block are $(\tilde{A}, \tilde{B}, \tilde{C}, \tilde{D})$, which are the gain matrices to be sent to the time varying state-space block.

The quadratic $\mathcal{H}^\infty$ performance of the closed-loop system is $\gamma = 0.1738$. After controller reduction, for intermediate values of $\alpha(t) \in (0, 1)$, the poles of the reduced controller will be very close to the slow modes of the vertex controllers.

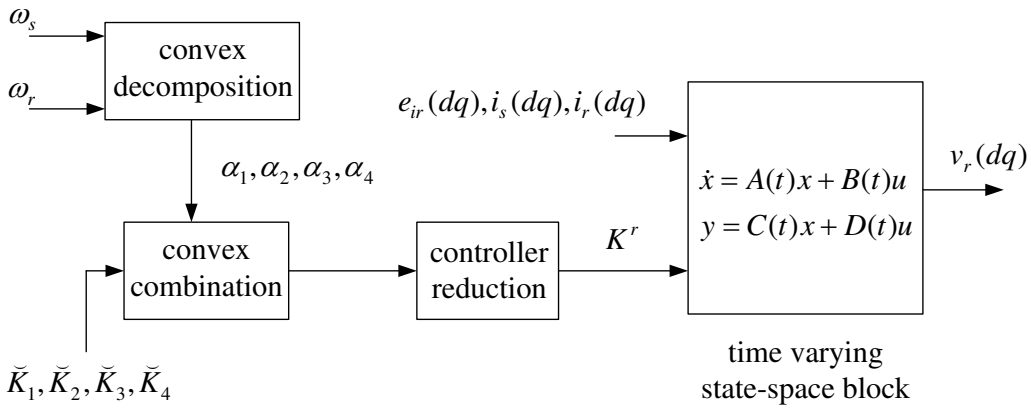

Figure 3.4: The Simulink implementation of the LPV controller, including the controller reduction procedure shown in Section 3.4. Based on the measurements of ω_s and ω_r, the self-scheduled LPV controller is being updated online, in real-time.

The nominal physical parameters of a $6MW$ wind turbine can be seen in Table 3.1. The voltage supply has been modelled by a 3-phase programmable source. This block is used to generate a frequency dip, while keeping constant amplitude (see Figure 3.6). A 3-phase PLL block has been used to measure the grid frequency f_g. The abc to dq block is used for transforming the voltage signal from abc to dq frame, see Figure 3.5. In the stator-flux reference frame, assuming that ω_s is constant and the stator resistance R_s is negligible, we approximately have $v_{ds} = 0$ and $v_{qs} = |v_s|$. Figure 3.5 corresponds to this simplified situation.

The proportional gain k_p of the frequency support controller (see Figure 3.1) is tuned based on the amount of power output needed for grid support. But at the same time, it

Table 3.1: Nominal physical parameters of a $6MW$ wind turbine

Description	Parameter	Value
Rated turbine power		$6MW$
Stator resistance	R_s	0.0022Ω
Rotor resistance	R_r	0.0018Ω
Stator inductance	L_s	$3mH$
Rotor inductance	L_r	$2.9mH$
Mutual inductance	L_m	$2.9mH$
Pole pairs	n_p	3
Stator voltage	v_s	$690V$(RMS)
Grid frequency	f_g^{ref}	50Hz
Turbine inertia	J_T	$2.225 \cdot 10^7 kgm^2$
Generator inertia	J_G	$600kgm^2$
Torsional stiffness	K_s	$7.5 \cdot 10^8 Nm/rad$
Torsional damping	C_s	$100Nms/rad$
Damping coefficient	b	$0kgm^2/s$
Gearbox ratio	n_g	21.64
Blade length	R_w	$55m$
Air density	ρ	$1.225kg/m^3$

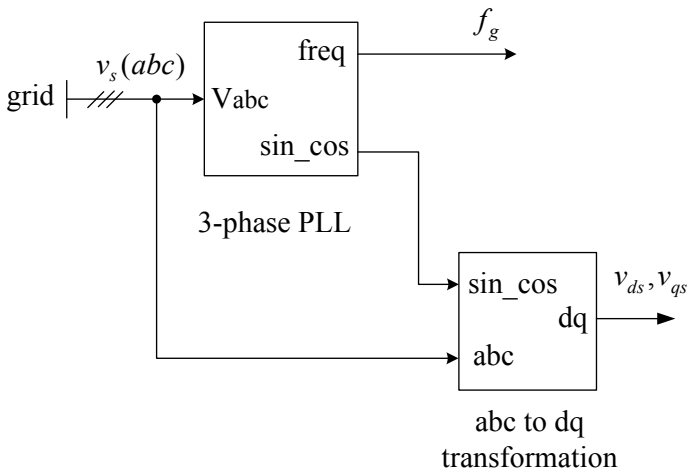

Figure 3.5: The Simulink model of a simplified version of the PLL-based estimation of f_g, v_{ds} and v_{qs} (these are expressed in the stator-flux reference frame). In this simplified version, it is assumed that $R_s = 0$ and ω_s is constant. A 3-phase programmable source has been used to generate the grid voltage with a frequency dip, while keeping constant amplitude.

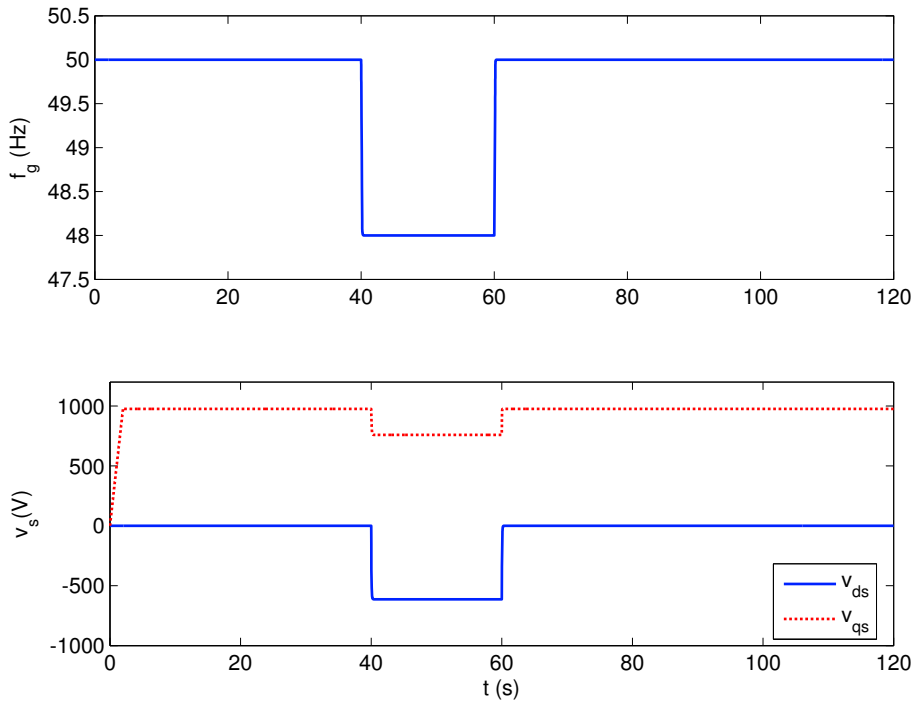

Figure 3.6: The grid frequency f_g and the stator voltages v_{ds}, v_{qs}. At $t = 40s$, the frequency f_g drops from 50Hz to 48Hz and recovers at $t = 60s$.

should be confined by the physical constraints of the turbine system. A large k_p would result in a large reference torque once a grid frequency drop is detected, meaning that a large amount of electrical power output is demanded in a very short-term frame. This could potentially damage the turbine shaft and/or the converters if the sudden demand of active power is too much. Here we choose $k_p = 10^4$.

We assume that the average wind speed is $10m/s$, where $\omega_r = \omega_s$ in the steady state. The first set of simulation results is based on a constant wind speed, equal to $12m/s$. The turbine behavior and the DFIG behavior are shown in Figures 3.7, 3.8 and 3.9. The power coefficient C_p has been maintained to be around its maximal value $C_p^{max} = 0.4587$ in the steady state, which implies that we have achieved the control objective of wind energy capture maximization. The stator active and reactive powers depend on i_{qr} and i_{dr} respectively in the stator-flux reference frame. i_{dr}^{ref} should be given by the outer-loop controller for grid integration. Here we take $i_{dr}^{ref} = 0$. It can be seen clearly from Figure 3.9 that good current tracking performance has been achieved. The second set of simulation results is based on a more realistic random wind speed, shown in Figures 3.10, 3.11 and 3.12. The wind speed along the turbine axis (see Figure 3.10) has been generated based on the frequency spectrum proposed by Kaimal (see [52]).

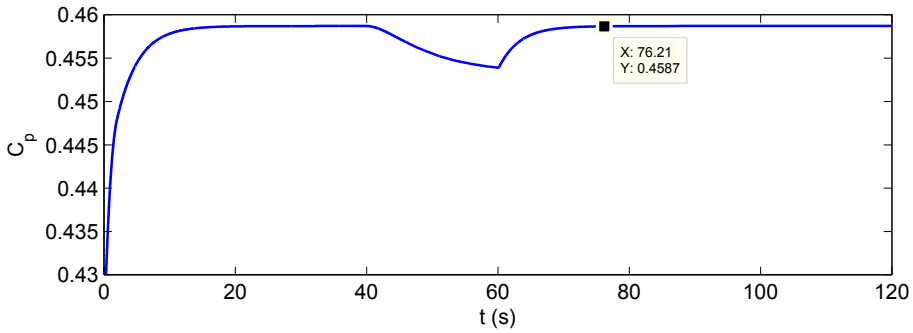

Figure 3.7: The plot of C_p assuming constant wind speed and a grid frequency drop of 2Hz between $t = 40s$ and $t = 60s$. From $40s$ to $60s$, C_p is decreasing due to the frequency support controller. After $60s$, C_p recovers to its maximum value $C_p^{max} = 0.4587$ within $15s$.

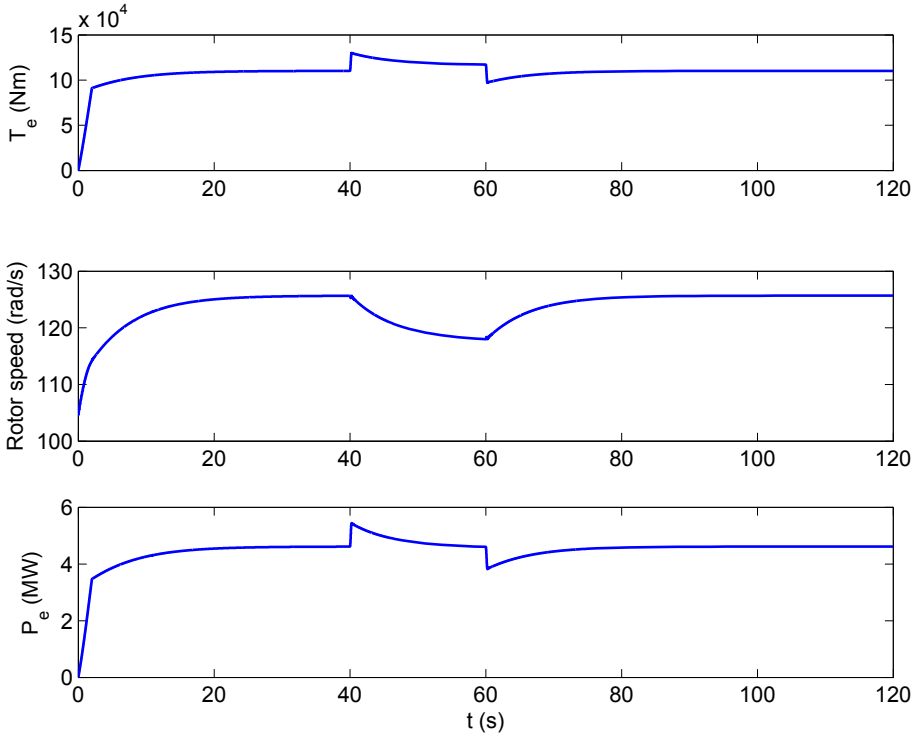

Figure 3.8: Electrical torque T_e, generator rotor speed ω_r and electrical power output P_e under constant wind speed. The difference between T_e^{ref} and T_e is visually not distinguishable at the scale of the plot. At $t = 40s$, there is a sudden increase in T_e, which is due to the frequency support controller. The additional power output between $40s$ and $60s$ demonstrates the contribution of the wind turbine to grid frequency support.

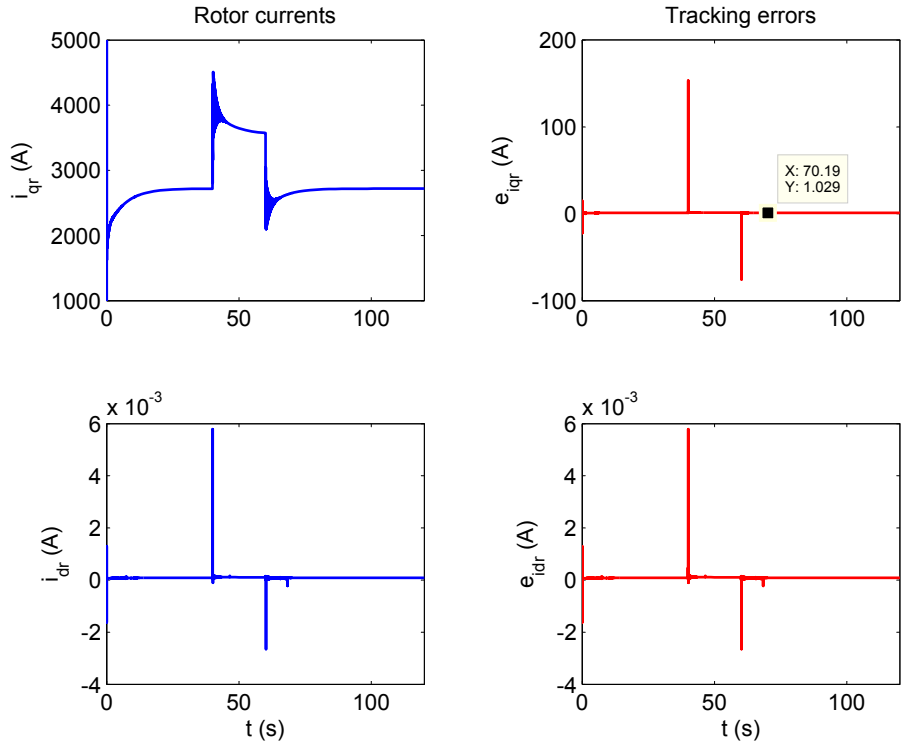

Figure 3.9: DFIG rotor current tracking under constant wind speed. The spikes in the tracking errors at $40s$ and $60s$ are due to the frequency support controller. In the steady state, it can be seen that e_{iqr} is around 1 A, which is very small compared to i_{qr} (more than 2000A).

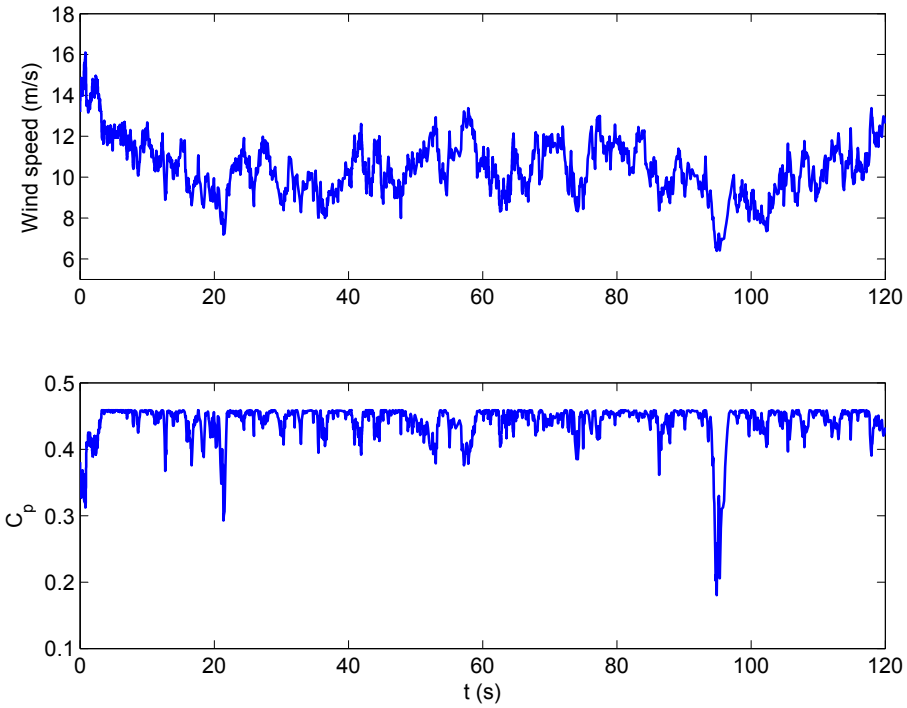

Figure 3.10: A more realistic random wind speed and the plot of C_p. After the first few seconds, the wind speed is in the range $[6, 14]m/s$, representing the low to medium wind speed region (or region 2). From $40s$ to $60s$, C_p drops in response to the wind speed and the frequency support controller.

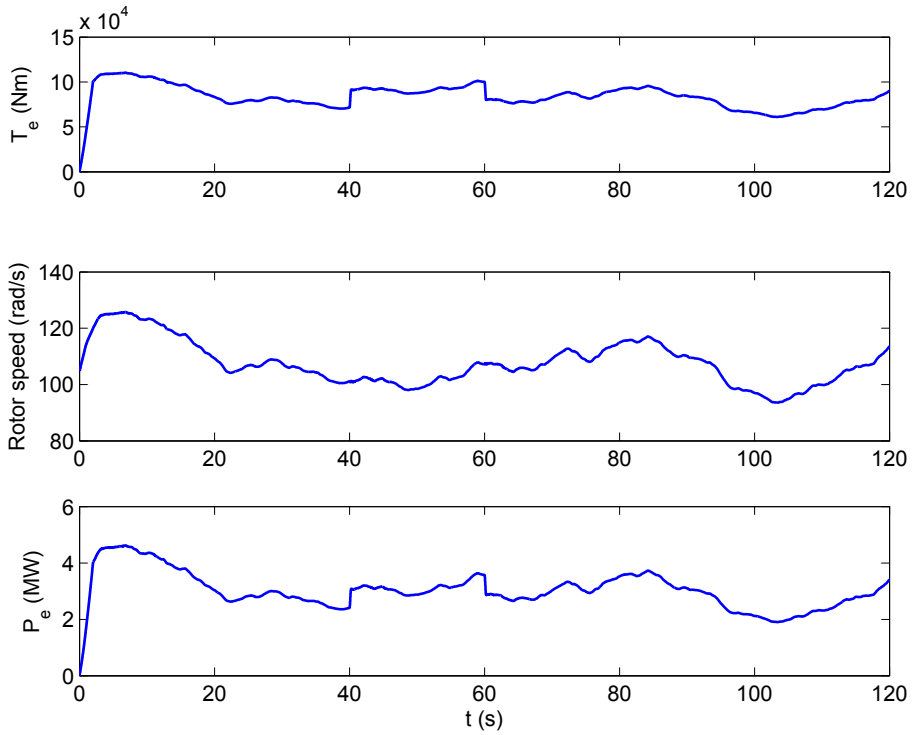

Figure 3.11: Electrical torque T_e, generator rotor speed ω_r and electrical power output P_e under random wind speed. The difference between T_e^{ref} and T_e is visually not distinguishable at the scale of the plot. At $t = 40s$, there is a sudden increase in T_e, which is due to the frequency support controller. The additional power output between $40s$ and $60s$ demonstrates the contribution of the wind turbine to grid frequency support.

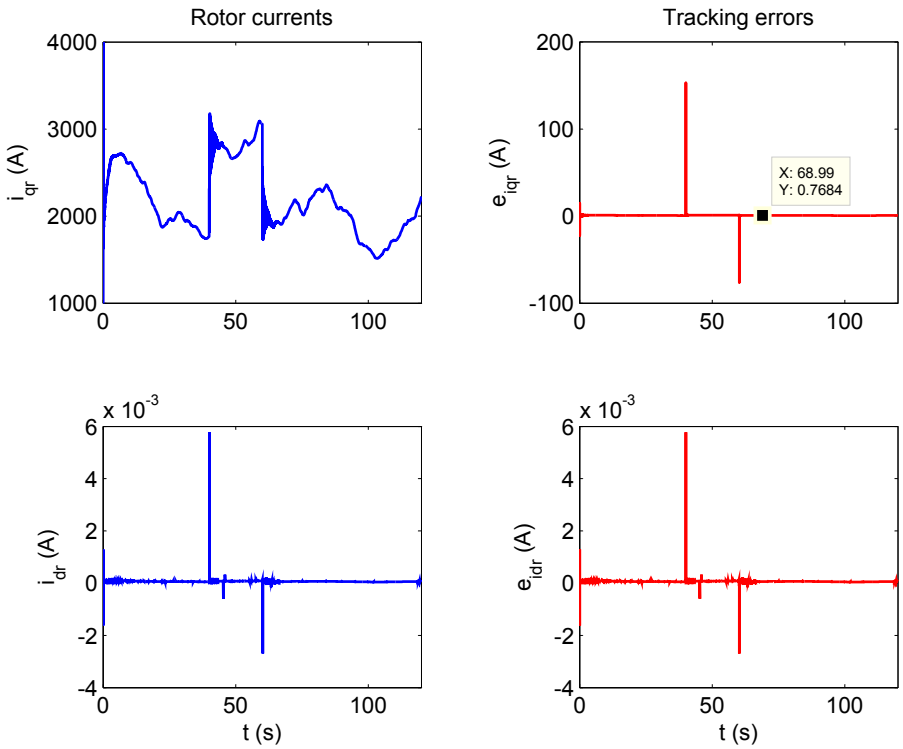

Figure 3.12: DFIG rotor current tracking under random wind speed. The spikes in the tracking errors at $40s$ and $60s$ are due to the frequency support controller. It can be seen that $e_{iqr} < 1A$ at around $70s$, which is very small compared to i_{qr} (more than 2000A).

Chapter 4

The iISS property for passive nonlinear systems

4.1 Background concepts

The concept of passivity is important in control theory because 1) it is a property shared by many physical systems; 2) it is related to stability (see Moylan [40], Hill and Moylan [25], Byrnes, Isidori and Willems [12]). Consider a dynamical system **S** described by the state equations

$$\begin{aligned} \dot{x} &= f(x,u), \\ y &= h(x,u), \end{aligned} \tag{4.1.1}$$

where $f : \mathbb{R}^n \times \mathbb{R}^m \to \mathbb{R}^n$ is locally Lipschitz continuous and $h : \mathbb{R}^n \times \mathbb{R}^m \to \mathbb{R}^m$ is continuous. Here $x(t)$ is the state at time t, which is in $\mathbb{R}^n$, u is the input signal and y is the output signal. Under these assumptions, for every initial state $x(0)$ and for every bounded input signal u, (4.1.1) has a unique solution on some time interval $[0, \epsilon)$, with $\epsilon > 0$. **S** is said to be *passive* if there exists a continuously differentiable *storage function* or *Hamiltonian* $H : \mathbb{R}^n \to [0, \infty)$ such that

$$\dot{H} \leq u^T y, \quad \text{where} \quad \dot{H} = \frac{\partial H}{\partial x} f(x,u),$$

for all $(x,u) \in \mathbb{R}^n \times \mathbb{R}^m$. To investigate the Lyapunov stability of the equilibrium points of **S** corresponding to $u = 0$ we may use H as a Lyapunov function (see Willems [62] or Khalil [32]).

The notion of input-to-state stability (ISS), as introduced in Sontag [49], implies that $f(x,0) = 0$ iff $x = 0$ and for any initial state, if the input becomes uniformly very small after some time, then also the state becomes uniformly very small after some time (see Sontag [51]). A strictly weaker variant of ISS is the concept of integral input-to-state stability (iISS), where the uniform smallness of the input is replaced by the smallness of a certain integral depending on the input, see Angeli, Sontag and Wang [3]. The formal definition of iISS is given below.

In this Chapter, we investigate the iISS property of passive nonlinear systems. In our main result (stated in Section 4.2), we show that under mild assumptions, a passive nonlinear system which is globally asymptotically stable (GAS) is also iISS. Stability analysis often involves a big effort to search for a Lyapunov function. Our main result is meant to eliminate the need for finding a Lyapunov function satisfying the condition (4.1.3) below, for passive systems. By combining our result with a recent result in Jayawardhana, Teel and Ryan [29], we can actually prove that under mild technical assumptions, a passive and GAS system satisfies the iISS type estimate with a very simple (L^1 norm type) integral term. We will illustrate the result by proving the iISS property (with a simple integral term) for the drive-train of a wind turbine, in Chapter 5.

For the remainder of this section, we recall the background about the iISS property following [3].

A function $V : \mathbb{R}^n \to [0,\infty)$ is called *positive definite* if $V(x) = 0$ iff $x = 0$. V is called *proper* if $V(x) \to \infty$ when $||x|| \to \infty$. Recall that a continuous function $\alpha : [0,a) \to [0,\infty)$ is said to belong to the class $\mathcal{K}$ if it is strictly increasing and $\alpha(0) = 0$. Such a function α is said to belong to the class $\mathcal{K}_\infty$ if $a = \infty$ and $\alpha(r) \to \infty$ as $r \to \infty$. A continuous function $\beta : [0,a) \times [0,\infty) \to [0,\infty)$ is said to belong to the class $\mathcal{KL}$ if, for each fixed s, the mapping $\beta(r,s)$ belongs to the class $\mathcal{K}$ with respect to r and, for each fixed r, the mapping $\beta(r,s)$ is decreasing with respect to s and $\beta(r,s) \to 0$ as $s \to \infty$.

Consider the system described by (4.1.1). Given any measurable and bounded control u and any $\xi \in \mathbb{R}^n$, there is a unique solution of the initial value problem $\dot{x} = f(x,u),\ x(0) = \xi$. This solution (or state trajectory) is defined on some maximal interval of the type $[0,\delta)$, and it is denoted by $x(\cdot,\xi,u)$.

Definition 4.1.1. The system described by (4.1.1) is *integral input-to-state stable* (iISS) if there exist a class $\mathcal{K}_\infty$ function α, a class $\mathcal{KL}$ function β and a class $\mathcal{K}$ function γ such that for every $\xi \in \mathbb{R}^n$ and for every measurable and bounded function u, the state trajectory $x(t, \xi, u)$ is defined for all $t \geq 0$, and

$$\alpha(||x(t, \xi, u)||) \leq \beta(||\xi||,\ t) + \int_0^t \gamma(||u(\tau)||)d\tau \quad \forall t \geq 0. \tag{4.1.2}$$

The function γ is called the *iISS gain* of the system described by (4.1.1). If the input u is such that $\int_0^\infty \gamma(||u(\tau)||)d\tau < \infty$, then the iISS estimate in (4.1.2) also implies the converging-state property: $x(t, \xi, u) \to 0$ as $t \to \infty$. However, if the system is iISS and u is only bounded, then the state trajectory $x(\cdot, \xi, u)$ may be unbounded.

Note that if the system described by (4.1.1) is iISS, then this system has a unique equilibrium point at zero ($f(x, 0) = 0$ iff $x = 0$) and the system is *globally asymptotically stable* (GAS), which means that it is Lyapunov stable, the trajectories $x(t, \xi, 0)$ are defined for all $t \geq 0$ and tend to zero (as $t \to \infty$).

Definition 4.1.2. The system described by (4.1.1) is *zero-output dissipative*, if there exists a continuously differentiable proper and positive definite function V, and a class $\mathcal{K}$ function σ, such that

$$\frac{\partial V}{\partial x} f(x, u) \leq \sigma(||u||) \qquad \forall (x, u) \in \mathbb{R}^n \times \mathbb{R}^m. \tag{4.1.3}$$

Theorem 4.1.1. *The system described by (4.1.1) is iISS if and only if it is GAS and zero-output dissipative.*

This follows from [3, Theorem 1] together with [3, Remark II.3].

In the following theorem, a technical assumption on f and σ has to be imposed (see [29, Theorem 3.1]):

(A) There exists a class $\mathcal{K}$ function σ and for every compact set $L \subset \mathbb{R}^n$, there exists $l > 0$ such that,

$$\|f(x, u)\| \leq l(1 + \sigma(\|u\|)) \quad \forall (x, u) \in L \times \mathbb{R}^m. \tag{4.1.4}$$

Theorem 4.1.2. *Assume that the system described by (4.1.1) satisfies (**A**), is GAS and zero-output dissipative with the same function σ in (4.1.3) and (4.1.4). Then for every $\xi \in \mathbb{R}^n$ and for every measurable and bounded function $u : [0, \infty) \to \mathbb{R}^m$, the state trajectory $x(t, \xi, u)$ (which is defined for all $t \geq 0$ according to Theorem 4.1.1) satisfies (4.1.2) with $\gamma = \sigma$.*

This recent result on the iISS gain is due to Jayawardhana, Teel and Ryan [29]. In particular, it follows that if $\int_0^\infty \sigma(||u(\tau)||)d\tau < \infty$, then $x(t, \xi, u) \to 0$ as $t \to \infty$.

4.2 The iISS property for passive nonlinear systems

Consider the system Σ described by

$$\begin{aligned} \dot{x} &= f(x, u), \\ y &= h(x), \end{aligned} \tag{4.2.1}$$

where $f : \mathbb{R}^n \times \mathbb{R}^m \to \mathbb{R}^n$ is locally Lipschitz and $h : \mathbb{R}^n \to \mathbb{R}^m$ is continuous.

Our main results are the following:

Theorem 4.2.1. *We assume that Σ is passive and GAS, with the storage function H. Denote*

$$c(r) = \sup_{\|x\| \leq r} \|h(x)\|.$$

We assume that there exist $\alpha,\ k > 0$ and $R \geq 0$ such that

$$H(x) \geq k\|x\|^\alpha \ \text{ for } \ \|x\| \geq R \tag{4.2.2}$$

and

$$\int_0^\infty \frac{d\theta}{c(\theta^{\frac{1}{\alpha}}) + 1} = \infty. \tag{4.2.3}$$

Then the system described by (4.2.1) is zero-output dissipative with $\sigma(r) = r$, and hence it is iISS.

Proof: Define $\lambda_0 = kR^\alpha \geq 0$, then obviously $c(R) = c((\frac{\lambda_0}{k})^{\frac{1}{\alpha}})$.

Choose the Lyapunov function $V(x) = F(H(x))$, where

$$F'(\lambda) = \begin{cases} \frac{1}{c(R)+1} & when \quad \lambda < \lambda_0, \\ \frac{1}{c((\frac{\lambda}{k})^{\frac{1}{\alpha}})+1} & when \quad \lambda \geq \lambda_0, \end{cases} \qquad \forall \lambda \geq 0.$$

It is easy to see that $F'(\lambda)$ is a non-increasing continuous function of λ (see Figure 4.1). We remark that in the region of $\mathbb{R}^n$ where $H(x) \leq \lambda_0$, we have $F(\lambda) = \frac{\lambda}{c(R)+1}$, so that $V(x) = \frac{H(x)}{c(R)+1}$.

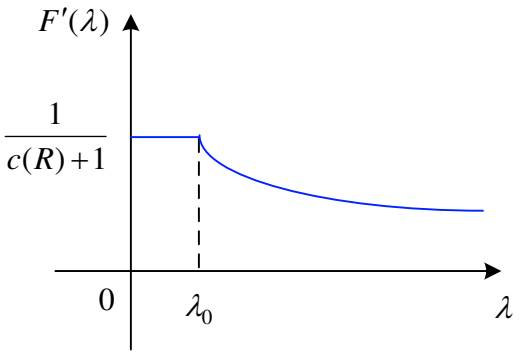

Figure 4.1: The function $F'(\lambda)$, which is a non-increasing continuous function of λ. In this figure we have assumed that $\lambda_0 > 0$.

We want to show that (4.2.1) with V satisfy (4.1.3). We have to consider two cases depending on $\|x\|$.

- Assume that $x \in \mathbb{R}^n$ with $\|x\| < R$ (case 1). Using the passivity of Σ and the Cauchy-Schwarz inequality, we obtain

$$\begin{aligned} \dot{V} &= F'(H(x))\dot{H} \\ &\leq \frac{1}{c(R)+1} \cdot u^T y \\ &\leq \frac{1}{c(R)+1} \cdot \|h(x)\| \cdot \|u\| \\ &\leq \frac{1}{c(R)+1} \cdot c(\|x\|) \cdot \|u\|. \end{aligned}$$

  Since $c(r)$ is a non-decreasing function of $r \in [0, \infty)$, $\|x\| < R$ implies that $c(\|x\|) \leq c(R)$. Using this inequality, we have

$$\dot{V} \leq \|u\|.$$

- Now assume that $x \in \mathbb{R}^n$ with $\|x\| \geq R$ (case 2). Then $k\|x\|^\alpha \geq kR^\alpha = \lambda_0$, so that $F'(k\|x\|^\alpha) = \frac{1}{c(\|x\|)+1}$. Using the assumption (4.2.2) and the fact that F' is

non-increasing, we have

$$F'(H(x)) \leq F'(k\|x\|^\alpha).$$

This implies, using again the passivity of Σ and the Cauchy-Schwarz inequality,

$$\begin{aligned}
\dot{V} &= F'(H(x))\dot{H} \\
&\leq F'(k\|x\|^\alpha) \cdot u^T y \\
&\leq \frac{1}{c(\|x\|)+1} \cdot \|h(x)\| \cdot \|u\| \\
&\leq \frac{1}{c(\|x\|)+1} \cdot c(\|x\|) \cdot \|u\| \\
&\leq \|u\|.
\end{aligned}$$

Thus we have proved that $\dot{V} \leq \|u\|$ for all $x \in \mathbb{R}^n$. This implies that (4.2.1) is zero-output dissipative.

Now we show that V is proper. We have

$$\int_0^\infty F'(\lambda)d\lambda = \infty. \tag{4.2.4}$$

Indeed, using (4.2.3), we have

$$\begin{aligned}
\int_0^\infty F'(\lambda)d\lambda &\geq \int_{\lambda_0}^\infty F'(\lambda)d\lambda \\
&= k\int_{\frac{\lambda_0}{k}}^\infty \frac{d\theta}{c(\theta^{\frac{1}{\alpha}})+1} = \infty.
\end{aligned}$$

Since H is proper (this follows from (4.2.2)), we have

$$\lim_{\|x\|\to\infty} V(x) = \lim_{H\to\infty} F(H) = \lim_{H\to\infty} \int_0^H F'(\lambda)d\lambda = \infty.$$

(We have used (4.2.4).) Since Σ is GAS, applying Theorem 4.1.1 we conclude that Σ is iISS. □

Remark 4.2.1. If the output y of the system Σ is a linear function of the state x, i.e. $h(x) = Cx$, where C is a matrix of matching dimensions, then $c(r) = \|C\|r$ and then (4.2.3) holds for every $\alpha \geq 1$.

Remark 4.2.2. If there exist $k_1 > 0$ and $r_0 \geq 0$ such that

$$c(r) \leq k_1 r^{\alpha} \qquad \forall r \geq r_0, \tag{4.2.5}$$

then it follows that (4.2.3) holds.

Theorem 4.2.2. *We assume that Σ is passive, GAS and satisfies (4.2.2) and (4.2.3). We also assume that f satisfies (**A**). Then for every $\xi \in \mathbb{R}^n$ and for every measurable and bounded function $u : [0, \infty) \to \mathbb{R}^m$, Σ has a unique state trajectory $x(\cdot, \xi, u)$ defined on $[0, \infty)$, and this satisfies*

$$\alpha(\|x(t, \xi, u)\|) \leq \beta(||\xi||, t) + \int_0^t \|u(\tau)\| d\tau \qquad \forall t \in [0, \infty), \tag{4.2.6}$$

where $\alpha \in \mathcal{K}_\infty$ and $\beta \in \mathcal{KL}$ are independent of ξ and u.

Note that (4.2.6) means that Σ is iISS, with the iISS gain $\gamma(r) = r$.

Proof: Recall from Theorem 4.2.1 that the system described by (4.2.1) is zero-output dissipative with $\sigma(\|u\|) = \|u\|$. Applying Theorems 4.1.1 and 4.1.2, we see that this system is iISS, with the iISS gain $\gamma(\|u\|) = \|u\|$. □

Remark 4.2.3. After seeing Theorem 4.2.2, it is tempting to conjecture that if Σ satisfies the assumptions in this theorem, then it has state trajectories for every $\xi \in \mathbb{R}^n$ and every $u \in L^1[0, \infty)$. However, this is not correct, as can be seen from Example 7.2 in Jayawardhana and Weiss [30]. The existence of global solutions is guaranteed only for bounded and measurable inputs.

4.3 Examples

Example 1: (A counter-example due to Bayu Jayawardhana). We consider the following system S, which is passive and GAS, but not iISS:

$$\begin{aligned} \dot{x}_1 &= -x_1 - (2+u)^2 x_2, \\ \dot{x}_2 &= (2+u)^2 x_1 + (1-x_2)^2 u, \\ y &= x_2 (1-x_2)^2. \end{aligned}$$

Choosing the storage function $H = \frac{1}{2}(x_1^2 + x_2^2)$, we have

$$\begin{aligned}
\dot{H} &= x_1\dot{x}_1 + x_2\dot{x}_2 \\
&= x_1[-x_1 - (2+u)^2 x_2] + x_2[(2+u)^2 x_1 + (1-x_2)^2 u] \\
&= -x_1^2 + uy \\
&\leq uy.
\end{aligned}$$

Hence S is passive.

If the control input $u = 0$, then S can be written as

$$\begin{aligned}
\dot{x}_1 &= -x_1 - 4x_2, \\
\dot{x}_2 &= 4x_1, \\
y &= x_2(1-x_2)^2,
\end{aligned}$$

so that the ordinary differential equation (ODE) describing the state trajectories is linear. The unique equilibrium point of this system is $\bar{x} = 0$. Clearly, for $u = 0$, S is GAS.

Now we choose the following control input

$$u(t) = \begin{cases} -2 & t \in [0,1), \\ 0 & else. \end{cases}$$

Then on the time interval $t \in [0,1)$, S can be written as

$$\begin{aligned}
\dot{x}_1 &= -x_1, \\
\dot{x}_2 &= -2(1-x_2)^2, \\
y &= x_2(1-x_2)^2.
\end{aligned} \tag{4.3.1}$$

If the initial state is such that $x_2(0) = 0.5$, then the solution of the ODE (4.3.1) is

$$x_2(t) = \frac{2t-1}{2(t-1)}.$$

We see that $x_2(t)$ blows up as $t \to 1$. Hence S is not iISS. Note that (4.2.2) holds with $\alpha \leq 2$ but (4.2.3) does not hold for any such α, because $c(r) \geq r^3$.

Example 2: In Chapter 5, we illustrate the main result (Theorem 4.2.2) by proving that the drive-train of a wind turbine with quadratic torque control is iISS, see Theorem 5.3.4.

Chapter 5

Stability analysis of the drive-train of a wind turbine with quadratic torque control

5.1 Background concepts

Here, the material concerning passivity and ISS is taken from Khalil [32].

Consider the dynamical system S described by the state-space model

$$\begin{aligned} \dot{x} &= f(x,u), \\ y &= h(x,u), \end{aligned} \tag{5.1.1}$$

where $f : \mathcal{R}^n \times \mathcal{R}^m \to \mathcal{R}^n$ and $h : \mathcal{R}^n \times \mathcal{R}^m \to \mathcal{R}^m$ are continuous,

$$f(0,0) = 0, \quad h(0,0) = 0.$$

Further technical assumptions are needed if we want to ensure that (5.1.1) has unique solutions (see for example [30, 50]). We will not deal with these technicalities, but always assume that our ODEs have unique solutions on some open interval.

Recall that a square matrix-valued transfer function G is called *positive-real* if $G(\bar{s}) = \bar{G}(s)$ and $G(s) + G(s)^* \geq 0$ for all complex s with $Re\, s > 0$.

Lemma 5.1.1 (Positive Real Lemma). *Let A, B, C, D be real matrixes of matching dimensions so that the transfer function $G(s) = C(sI - A)^{-1}B + D$ is defined and its values are square matrices. Assume that (A, B) is controllable and (A, C) is observable.*

Then $G(s)$ is positive-real if and only if there exist matrices $P = P^T$, L and W such that

$$\begin{aligned} PA + A^T P &= -L^T L, \\ PB &= C^T - L^T W, \\ W^T W &= D + D^T. \end{aligned}$$

Lemma 5.1.2. *The linear time-invariant minimal system*

$$\begin{aligned} \dot{x} &= Ax + Bu, \\ y &= Cx + Du, \end{aligned}$$

with $G(s) = C(sI - A)^{-1}B + D$ is passive if and only if $G(s)$ is positive-real.

Definition 5.1.1. The system described by (5.1.1) is said to be *input-to-state stable (ISS)* if there exist a class $\mathcal{KL}$ function β and a class $\mathcal{K}$ function γ such that for any initial state $x(0)$ and any essentially bounded and measurable input function u, the solution $x(t)$ exists for all $t \geq 0$ and satisfies

$$||x(t)|| \leq \beta(||x(0)||,\ t) + \gamma(||u||_{L^\infty[0,\,t]}).$$

A function $V : \mathcal{R}^n \to [0, \infty)$ is called *positive definite* if $V(x) = 0$ iff $x = 0$. V is called *proper* if $V(x) \to \infty$ when $||x|| \to \infty$.

Theorem 5.1.3. *Let $V : \mathcal{R}^n \to \mathcal{R}$ be a continuously differentiable function such that*

$$\alpha_1(||x||) \leq V(x) \leq \alpha_2(||x||) \quad \forall x \ \in \mathcal{R}^n, \tag{5.1.2}$$

$$\frac{\partial V}{\partial x} f(x, u) \leq -W(x), \tag{5.1.3}$$

for all $(x, u) \in \mathcal{R}^n \times \mathcal{R}^m$ such that $||x|| \geq \rho(||u||) > 0$, where α_1, α_2 are of class $\mathcal{K}_\infty$, ρ is of class $\mathcal{K}$, and $W : \mathcal{R}^n \to [0, \infty)$ is positive definite. Then the system **S** *is ISS with $\gamma = \alpha_1^{-1} \circ \alpha_2 \circ \rho$.*

5.2 Stability analysis based on the one-mass drive-train model

For the turbine operating in region 2, we generate the reference electrical torque given by the standard quadratic torque control law, as explained in Subsection 2.3:

$$T_e^{ref} = \begin{cases} 0 & when \quad \omega_m < 0, \\ K\omega_m^2 & when \quad \omega_m \geq 0, \end{cases} \tag{5.2.1}$$

where $K > 0$. We introduce

$$d_u = T_e^{ref} - T_e, \tag{5.2.2}$$

which is proportional to the q-component tracking error of the current controller. We have mentioned that a good current controller leads to fast and accurate tracking of the rotor current references, and hence to accurate tracking of the electrical torque reference T_e^{ref}. Thus when analyzing the much slower mechanical system (the drive-train), it is reasonable to assume that d_u is small.

Proposition 5.2.1. *Consider the closed-loop wind turbine system* $\mathbf{S}_1$ *described by (2.8.1) and (5.2.1), with* $b \geq 0$, $d_u = 0$ *and with input* T_t *and output* ω_m. *Take* $T_t = c > 0$ *(a constant). Then this system is GAS with respect to the equilibrium point*

$$\bar{\omega}_m = \frac{\sqrt{b^2 + 4cK} - b}{2K}. \tag{5.2.3}$$

(Note that the stability is not due to the damping coefficient b, and it is true also for $b = 0$.)

Proof: The system $\mathbf{S}_1$ can be written as

$$\dot{\omega}_m = \begin{cases} \frac{1}{J}(c - b\omega_m) & when \quad \omega_m < 0, \\ \frac{1}{J}(c - K\omega_m^2 - b\omega_m) & when \quad \omega_m \geq 0. \end{cases} \tag{5.2.4}$$

In the region $\omega_m \geq 0$ we have the unique equilibrium point $\bar{\omega}_m$, which is the positive solution of the equation

$$0 = \frac{1}{J}(c - K\bar{\omega}_m^2 - b\bar{\omega}_m). \tag{5.2.5}$$

In the region $\omega_m < 0$ there is no equilibrium point. The equilibrium point $\bar{\omega}_m$ is attractive (locally stable), a fact that is easily seen by linearizing (5.2.4). In fact,

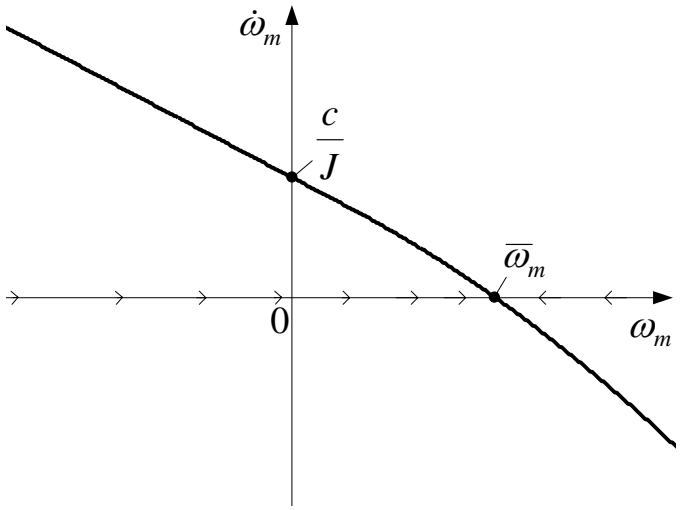

Figure 5.1: The dynamics and the equilibrium point $\bar{\omega}_m$ for the one-mass drive-train model.

this equilibrium point is GAS as can be seen in Figure 5.1. Formally, we may use $V(\omega_m) = \frac{1}{2}(\omega_m - \bar{\omega}_m)^2$ as a Lyapunov function, check that $\dot{V} < 0$ for $\omega_m \neq \bar{\omega}_m$ and use one of Lyapunov's stability theorems (see [32, Theorem 4.2]). □

Theorem 5.2.2. *Consider the closed-loop wind turbine system* $\mathbf{S}_1$ *described by (2.8.1), (5.2.1) and (5.2.2), with* $b > 0$*, where* $T_t = c + d_w$*,* $c > 0$ *is a constant and* d_u*,* d_w *are disturbance signals. We regard this system with input* $d = [d_w \ d_u]^T$ *and state* $\zeta = \omega_m - \bar{\omega}_m$*, where* $\bar{\omega}_m$ *is defined in (5.2.3). Then this system is ISS, more precisely*

$$||\zeta(t)|| \leq \beta(||\zeta(0)||, t) + \frac{2\sqrt{2}}{b}||d||_{L^\infty[0,\,t]}, \tag{5.2.6}$$

for all $t > 0$*, where* β *is a function of class* $\mathcal{KL}$*.*

Proof: Choose the Lyapunov function $V = \frac{1}{2}\zeta^2$. In the region $\omega_m \geq 0$, $\mathbf{S}_1$ can be written as

$$\dot{\omega}_m = \frac{1}{J}(c + d_w - K\omega_m^2 + d_u - b\omega_m).$$

Using (5.2.5), we obtain that in this region

$$\begin{aligned}\dot{\zeta} &= \frac{1}{J}(c + d_w - K\omega_m^2 + d_u - b\omega_m) \\ &= \frac{1}{J}\left[\ c + d_w + d_u - K(\zeta + \bar{\omega}_m)^2 - b(\zeta + \bar{\omega}_m)\ \right] \\ &= \frac{1}{J}(d_w + d_u) - \frac{K}{J}\zeta^2 - \frac{1}{J}\zeta(b + 2K\bar{\omega}_m).\end{aligned}$$

Since $\dot{V} = \zeta\dot{\zeta}$, we obtain

$$\dot{V} = -\frac{K}{J}\zeta^3 - \frac{1}{J}\zeta^2(b + 2K\bar{\omega}_m) + \frac{1}{J}\zeta(d_w + d_u). \tag{5.2.7}$$

We need the following inequality:

$$-\frac{K}{J}\zeta^3 - \frac{1}{J}\zeta^2(b + 2K\bar{\omega}_m) \leq -\frac{b}{J}\zeta^2 \quad \forall\zeta \in [-\bar{\omega}_m, \infty). \tag{5.2.8}$$

This holds because it reduces to

$$\frac{K}{J}\zeta^2(\zeta + 2\bar{\omega}_m) \geq 0 \quad \forall\zeta \in [-\bar{\omega}_m, \infty).$$

Substituting the inequality (5.2.8) into (5.2.7), we obtain

$$\begin{aligned}\dot{V} &\leq -\frac{b}{J}\zeta^2 + \frac{1}{J}\zeta(d_w + d_u) \\ &\leq -\frac{b}{2J}|\zeta|^2 - \frac{b}{2J}|\zeta|^2 + \frac{\sqrt{2}}{J}|\zeta| \cdot ||d|| \\ &\leq -\frac{b}{2J}|\zeta|^2 \quad \forall|\zeta| \geq \frac{2\sqrt{2}}{b}||d||.\end{aligned}$$

We conclude that in the region $\omega_m \geq 0$ (i.e. $\zeta \geq -\bar{\omega}_m$), the inequality

$$\dot{V} \leq -\frac{b}{2J}|\zeta|^2$$

holds for all d satisfying $||d|| \leq \frac{b}{2\sqrt{2}}|\zeta|$. Thus, (5.1.3) holds with

$$W(\zeta) = \frac{b}{2J}|\zeta|^2 \quad and \quad \rho(r) = \frac{2\sqrt{2}}{b}r.$$

In the region $\omega_m < 0$ the system $\mathbf{S}_1$ can be written as

$$\dot{\omega}_m = \frac{1}{J}(c + d_w + d_u - b\omega_m).$$

Take again $\zeta = \omega_m - \bar{\omega}_m$ (so that $\zeta \leq -\bar{\omega}_m$). Using (5.2.5), we obtain that in this region

$$\begin{aligned}\dot{\zeta} &= \frac{1}{J}(c + d_w + d_u - b\bar{\omega}_m - b\zeta) \\ &= \frac{1}{J}(K\bar{\omega}_m^2 + d_w + d_u - b\zeta).\end{aligned}$$

Assuming that $||d|| \leq \frac{b}{2\sqrt{2}}|\zeta|$, we have

$$\begin{aligned}\dot{V} &= \frac{1}{J}\zeta(K\bar{\omega}_m^2 + d_w + d_u - b\zeta) \\ &= \frac{1}{J}|\zeta|(-K\bar{\omega}_m^2 - d_w - d_u - b|\zeta|) \\ &\leq \frac{1}{J}|\zeta|(\sqrt{2}||d|| - b|\zeta|) \\ &\leq -\frac{b}{2J}|\zeta|^2.\end{aligned}$$

Thus (5.1.3) holds in this region (with the same W and ρ).

The Lyapunov function $V = \frac{1}{2}\zeta^2$ satisfies (5.1.2) with $\alpha_1(r) = \alpha_2(r) = \frac{1}{2}r^2$. We apply Theorem 5.1.3, where $(\alpha_1^{-1} \circ \alpha_2)(r) = r$, so that $\gamma(r) = \frac{2\sqrt{2}}{b}r$. We conclude that the system $\mathbf{S}_1$ is ISS with this $\gamma(r)$, so that (5.2.6) holds. □

Remark 5.2.1. If the damping coefficient $b = 0$, then we lose the ISS property, because for $\omega_m < 0$, a negative T_t will accelerate the turbine so that $\omega_T \to -\infty$. This would not happen in practice, because the yaw controller (ignored in our analysis) would reverse the turbine leading to $T_t > 0$.

5.3 Stability analysis based on the two-mass drive-train model

Proposition 5.3.1. *Consider the linear drive-train system* $\mathbf{S}_1$*, described by the matrices* (A, B, C, D) *from (2.8.2), with input* $u = [T_a,\ -T_e]^T$*, state* $x = [\theta_k,\ \omega_T,\ \omega_m]^T$ *and output* $y = [\omega_T,\ \omega_m]^T$*. Then this system is passive with the storage function* $H(x) = x^T P x$*, where*

$$P = \begin{bmatrix} K_s & 0 & 0 \\ 0 & J_T & 0 \\ 0 & 0 & J_G \end{bmatrix}. \tag{5.3.1}$$

Proof: For the two-mass drive-train model (2.8.2), it can be checked that (A, B) is controllable and (A, C) is observable. If we choose a positive definite matrix P (5.3.1), then it can been shown that

$$\begin{aligned} PA + A^T P &= -Q \\ &= -\begin{bmatrix} 0 & 0 & 0 \\ 0 & 2C_s & -\frac{2C_s}{n_g} \\ 0 & -\frac{2C_s}{n_g} & \frac{2C_s}{n_g^2} + 2b \end{bmatrix}, \\ PB &= C^T, \\ D + D^T &= 0. \end{aligned} \tag{5.3.2}$$

The matrix Q is positive semi-definite. We take $L = \sqrt{Q}$ and $W = 0$, then according to Lemmas 5.1.1 and 5.1.2, the system (A, B, C, D) is passive. □

Proposition 5.3.2. *Consider the closed-loop wind turbine system* $\mathbf{S}_2$ *described by (2.8.2), (5.2.1) and (5.2.2). We regard this system with input* $d = [T_a,\ d_u]^T$*, state* $x = [\theta_k,\ \omega_T,\ \omega_m]^T$ *and output* $y = [\omega_T,\ \omega_m]^T$*. Then this system is passive with the same storage function* H *as in Proposition 5.3.1.*

Proof: From Proposition 5.3.1, we see that $\mathbf{S}_1$ is passive. Choose the same storage function H, we have

$$\begin{aligned} \dot{H} &\leq u^T y \\ &= \begin{bmatrix} T_a \\ d_u - T_e^{ref} \end{bmatrix}^T \begin{bmatrix} y_1 \\ y_2 \end{bmatrix} \\ &= \begin{bmatrix} T_a \\ d_u \end{bmatrix}^T \begin{bmatrix} y_1 \\ y_2 \end{bmatrix} - T_e^{ref} y_2. \end{aligned}$$

We see from (5.2.1) that the term $T_e^{ref} y_2 \geq 0$ only exists when $y_2 = \omega_m \geq 0$. Hence we have

$$\dot{H} \leq \begin{bmatrix} d_1 \\ d_2 \end{bmatrix}^T \begin{bmatrix} y_1 \\ y_2 \end{bmatrix}.$$

Thus, $\mathbf{S}_2$ is passive. □

Proposition 5.3.3. *Consider the closed-loop system* $\mathbf{S}_2$ *formed by the drive-train (2.8.2) with the feedback law (5.2.1), with* $d_u = T_e^{ref} - T_e = 0$ *and with* $T_a = n_g c > 0$ *(a constant). Then this system is GAS with respect to the equilibrium point*

$$\bar{x} = \begin{bmatrix} \bar{x}_1 \\ \bar{x}_2 \\ \bar{x}_3 \end{bmatrix} = \begin{bmatrix} \frac{n_g c}{K_s} \\ \frac{\sqrt{b^2+4cK}-b}{2Kn_g} \\ \frac{\sqrt{b^2+4cK}-b}{2K} \end{bmatrix}. \tag{5.3.3}$$

Note that T_a is the aerodynamic torque (see (2.3.2)) and c is the active torque referred to the high speed shaft, as in Proposition 5.2.1.

Proof: The closed-loop system $\mathbf{S}_2$ with $T_a = n_g c$ can be written as

$$\dot{x} = \begin{cases} Ax + B_1 n_g c & when \quad \omega_m < 0, \\ Ax + B_1 n_g c + B_2(-Kx_3^2) & when \quad \omega_m \geq 0. \end{cases}$$

In the region $\omega_m \geq 0$ we have a unique equilibrium point $\bar{x}$, which is the positive solution of the equation

$$0 = A\bar{x} + B_1 n_g c + B_2(-K\bar{x}_3^2). \tag{5.3.4}$$

In the region $\omega_m < 0$ there is no equilibrium point.

Take $\zeta = x - \bar{x}$ and choose the Lyapunov function $V = \frac{1}{2}\zeta^T P \zeta$. In the region $\omega_m \geq 0$ (or $\zeta_3 \geq -\bar{x}_3$), using (5.3.5), we obtain

$$\begin{aligned} \dot{\zeta} &= Ax + B_1 n_g c + B_2(-Kx_3^2) \\ &= A(\zeta + \bar{x}) + B_1 n_g c - B_2 K(\zeta_3 + \bar{x}_3)^2 \\ &= A\zeta - B_2 K(\zeta_3^2 + 2\bar{x}_3\zeta_3). \end{aligned}$$

Since $\dot{V} = \zeta^T P \dot{\zeta}$, we obtain

$$\dot{V} = \frac{1}{2}\zeta^T(PA + A^T P)\zeta - K(\zeta_3^3 + 2\bar{x}_3\zeta_3^2).$$

We know from (5.3.2) that $PA + A^T P \leq 0$, hence

$$\begin{aligned} \dot{V} &\leq -K(\zeta_3^3 + 2\bar{x}_3\zeta_3^2) \\ &\leq 0 \quad \forall \zeta_3 \in [-\bar{x}_3, \infty). \end{aligned}$$

In the region $\omega_m < 0$ (or $\zeta_3 < -\bar{x}_3$), also using (5.3.5), we obtain

$$\begin{aligned}\dot{\zeta} &= Ax + B_1 n_g c \\ &= A(\zeta + \bar{x}) + B_1 n_g c \\ &= A\zeta + B_2 K \bar{x}_3^2.\end{aligned}$$

Choosing the same Lyapunov function, we obtain

$$\begin{aligned}\dot{V} &= \frac{1}{2}\zeta^T(PA + A^T P)\zeta + K\bar{x}_3^2\zeta_3 \\ &\leq K\bar{x}_3^2\zeta_3 \\ &< 0 \quad \forall \zeta_3 \in (-\infty, -\bar{x}_3).\end{aligned}$$

Using again one of Lyapunov's stability theorems (see [32, Theorem 4.2]), we conclude that the equilibrium point $\bar{x}$ is GAS. □

Now we shall consider the closed-loop system $\mathbf{S}_2$ consisting of the two-mass model of the drive-train, described by the matrices A, B, C, D from (2.8.2), with the quadratic torque control (5.2.1), with a torque tracking error d_u as in (5.2.2) and with an aerodynamic torque $T_a = n_g c + d_w$, where $n_g c$ is a "steady state" value and d_w is the deviation of T_a from this value, see Figure 5.2. Our main result is the following:

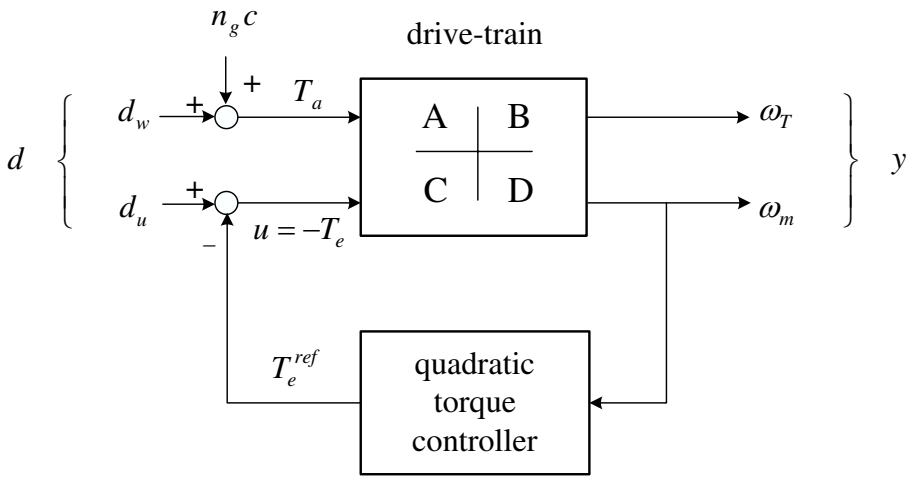

Figure 5.2: The (linear passive) two-mass drive-train from (2.8.2) with the quadratic torque controller from (5.2.1). This closed-loop system is called $\mathbf{S}_2$ in Theorem 5.3.4.

Theorem 5.3.4. *Consider the closed-loop wind turbine system* $\mathbf{S}_2$ *described by (2.8.2), (5.2.1) and (5.2.2), where* $T_a = n_g c + d_w$, $c > 0$ *is a constant and* d_u, d_w *are disturbance signals. We regard this system with input* $d = [d_w,\ d_u]^T$, *state* $\zeta = x - \bar{x}$, *where* $\bar{x}$ *is given in (5.3.3) and output* $y = [\zeta_2,\ \zeta_3]^T$. *Then this system is iISS, more precisely*

$$\alpha(\|\zeta(t)\|) \leq \beta(||\zeta(0)||, t) + \int_0^t \|d(\tau)\| d\tau,$$

for all $t > 0$, *where* $\alpha \in \mathcal{K}_\infty$ *and* $\beta \in \mathcal{KL}$.

Proof: We know from Proposition 5.3.2 that the closed-loop turbine system $\mathbf{S}_2$ is passive. We also know from Proposition 5.3.3 that $\mathbf{S}_2$ is GAS with respect to $\bar{x}$, which is the positive solution of the equation

$$0 = A\bar{x} + B_1 n_g c + B_2(-K\bar{x}_3^2). \tag{5.3.5}$$

In the region $\omega_m < 0$ there is no equilibrium point.

In the region $\omega_m \geq 0$ (or $\zeta_3 \geq -\bar{x}_3$), using (5.3.5) we obtain

$$\begin{aligned}
\dot{\zeta} &= Ax + B_1(n_g c + d_w) + B_2(-Kx_3^2 + d_u) \\
&= A(\zeta + \bar{x}) + B_1(n_g c + d_w) - B_2 K(\zeta_3 + \bar{x}_3)^2 + B_2 d_u \\
&= A\zeta + B_1 d_w + B_2 d_u - B_2 K(\zeta_3^2 + 2\bar{x}_3\zeta_3).
\end{aligned}$$

In the region $\omega_m < 0$ (or $\zeta_3 \leq -\bar{x}_3$), using (5.3.5), we obtain

$$\begin{aligned}
\dot{\zeta} &= A(\zeta + \bar{x}) + B_1(n_g c + d_w) + B_2 d_u \\
&= A\zeta + B_1 d_w + B_2 d_u + B_2 K\bar{x}_3^2.
\end{aligned}$$

In both regions $\omega_m \geq 0$ and $\omega_m < 0$, since $\dot{\zeta}$ depends on the input d linearly, we can easily see that the condition (**A**) in Theorem 4.1.2 holds.

Choose the storage function $H(\zeta) = \zeta^T P \zeta$, where P is the positive definite matrix shown in (5.3.1). Let λ_{min} denote the smallest eigenvalue of P (i.e. the smallest of K_s, J_T and J_G). Then $H(\zeta) \geq \lambda_{min}||\zeta||^2$. Hence, (4.2.2) holds for $\alpha = 2$ and $k = \lambda_{min}$.

Since the output of $\mathbf{S}_2$ depends on the state ζ linearly, i.e. $y = C\zeta$, we may choose $c(r) = \|C\| r = r$. Then it can be shown easily that (4.2.3) holds (see Remark 4.2.1).

Applying Theorem 4.2.2, we conclude that (4.2.6) holds. □

We remark that a direct proof of this theorem has been given in our paper [57], where we chose the Lyapunov function

$$V(\zeta) = \frac{\frac{1}{2}\zeta^T P \zeta}{\sqrt{1 + \frac{1}{2}\zeta^T P \zeta}}$$

and showed that $\mathbf{S}_2$ with V satisfy (4.1.3).

5.4 Adaptive torque control

For the turbine operating in region 2, we propose the following adaptive torque controller, which is very similar to the standard quadratic control law as shown in (5.2.1), but now K, instead of being a constant, is adaptive, searching for the value K^{opt} from (2.3.3). According to (2.3.3) we can factor $K^{opt} = \rho M^{opt}$, where the air density ρ is measurable, so that we only have to adjust an adaptive gain M searching for M^{opt}. The adaptive control law is

$$T_e^{ref} = \begin{cases} 0 & when \quad \omega_m < 0, \\ \rho M \omega_m^2 & when \quad \omega_m \geq 0. \end{cases} \tag{5.4.1}$$

We add a modulation $\Delta M \cdot \cos(\frac{2\pi}{T}t)$ to M to see its effect on the electrical power $P_e = T_e \omega_m$. The period T of this modulation is much larger than the time constant of the linearization of the system from (5.2.4), in order to eliminate the effect of the inertia. We expect P_e to oscillate in phase with M if $M < M^{opt}$, and we expect P_e to oscillate about 180° out of phase with M if $M > M^{opt}$. To eliminate as much as possible the effect of the random wind, we look at $\frac{P_e}{P_{wind}}$, instead of P_e, where P_{wind} is the available wind power (see (2.3.1)). For this, we need wind speed measurements. An anemometer on the top of the turbine's nacelle or on a separate meteorological tower can provide the wind speed measurements in real time (see [31]). Assuming that the wind speed measurements are reliable, we can use the following update algorithm for M:

$$\begin{aligned} \dot{z}(t) &= -\gamma z(t) + \frac{P_e(t)}{P_{wind}(t)} \cdot \cos(\frac{2\pi}{T}t), \\ \dot{M}_n(t) &= \lambda z(t), \\ M(t) &= M_n^{SZOH}(t) + \Delta M \cdot \cos(\frac{2\pi}{T}t), \end{aligned}$$

where γ is a forgetting factor, λ is a small positive constant, $M_n^{SZOH}(t)$ is the signal $M_n(t)$ processed by a sampler and a zero order hold (SZOH) with the sampling period T_s being an integer multiple of the modulation period T. Some guidelines on the tuning of these parameters will be given in Section 5.5. The block diagram of the algorithm for the adaptation of M is shown in Figure 5.3. Figure 5.4 shows a dynamic saturation block used for chopping off the spikes in the signal $\frac{P_e}{P_{wind}}$, which are due to wind gusts or to moments with $P_{wind} = 0$ (no wind).

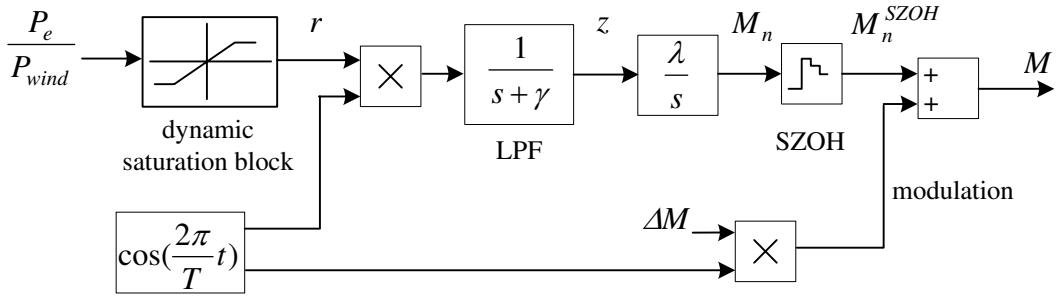

Figure 5.3: The block diagram of updating M. The details of the dynamic saturation block appearing above are shown in Figure 5.4. LPF stands for low pass filter.

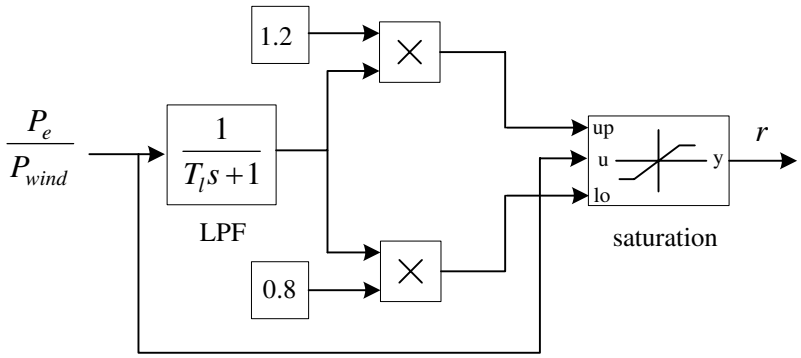

Figure 5.4: The dynamic saturation block used for conditioning the signal $\frac{P_e}{P_{wind}}$. If $\frac{P_e}{P_{wind}}$ has no sudden changes, such as spikes, then the output r of this block is the same as its input. Sudden changes larger than $\pm 20\%$ are cut off by this system. The signal r is fed into the adaptive torque control law. Here $T_l = 5T$. The block marked "saturation" is a saturation with unity gain and adjustable saturation limits.

The signal $\Delta M \cdot \cos(\frac{2\pi}{T}t)$ may be considered as being added to the tracking error of the generator torque, d_u (5.2.2), see Figure 5.2.

If the wind speed is constant, then M_n^{SZOH} converges to M^{opt} (the proof is a bit tedious and we omit it). With a random wind speed, M_n^{SZOH} will not converge, but it will vary in a narrow range around M^{opt}.

This search algorithm for the optimal gain M^{opt} need not run all the time: it may be enough to update M by running this adaptive system for one day every few months. The disturbance introduced to the power grid by this adaptive system (the modulation of M) is very small, see Section 5.5.

5.5 Simulation results

The simulations have been carried out using Matlab/Simulink. The two-mass drive-train model has been used to test the adaptive torque control method. The turbine parameters are taken from a generic $5MW$ offshore wind turbine model (see Table 5.1 and [33]). The damping coefficient b has been taken zero, because it is very small. The electrical subsystems of the wind turbine (DFIG, converters and their controllers) have also been neglected, because we assume that the DFIG with a good rotor current control system responds rapidly and accurately when tracking the reference torque given by the torque controller. The wind speed along the turbine axis (see Figure 5.5) has been generated based on the frequency spectrum proposed by Kaimal (see [52]).

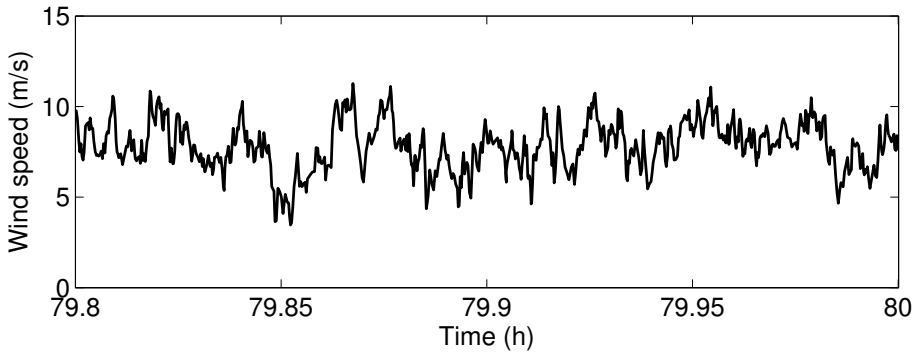

Figure 5.5: A realistic wind speed input ranging from $4m/s$ to $14m/s$ covering the low to medium wind speed region. This is a zoomed plot.

The parameters T, T_s, γ, λ and ΔM in the adaptive torque control law have been chosen based on trial and error. The modulation period T needs to be very large in order

Table 5.1: Nominal physical parameters of the $5MW$ wind turbine

Description	Parameter	Value
Rated turbine power		$5MW$
Number of blades		3
Turbine blade length	R_w	$55m$
Turbine inertia	J_T	$2.225 \cdot 10^7 kgm^2$
Gearbox ratio	n_g	60.88
Generator inertia	J_G	$600kgm^2$
Torsional stiffness	K_s	$7.5 \cdot 10^8 Nm/rad$
Torsional damping	C_s	$100Nms/rad$
Damping coefficient	b	$0kgm^2/s$
Air density	ρ	$1.225kg/m^3$
Grid frequency	f	$50Hz$
No. of pole pairs	n_p	2
Synchronous speed	ω_s	$157.08rad/s$

to eliminate the effect of the turbine inertia, so we chose $T = 2000s$. T_s has to be an integer multiple of T, so we chose $T_s = 4000s$. If we define the forgetting factor to be $\gamma = \frac{2\pi}{T_\gamma}$, then T_γ should be on the order of hours. We took $T_\gamma = 7200s$. λ and ΔM would influence the convergence rate of M. A large λ may cause instability, while a large ΔM would introduce large oscillations into the electrical torque. We chose $\lambda = 10^{-5}$ and $\Delta M = 0.15$.

Our main concerns on the adaptive torque control law are 1) its accuracy and convergence rate; 2) its influence on the power grid. Based on the standard quadratic control law (see (2.3.3)) as well as the simulated C_p curves (see Figure 2.3(b)), we can obtain the optimal gain $M^{opt} = 2.3m^5$. In one of the simulations (see Figure 5.7), we chose the initial value of M to be $1m^5$. This -56.5% deviation from the optimal gain M^{opt} would result in a 15% loss of the electrical power output if the wind speed were constant, equal to its mean value of $8m/s$. By using the adaptive torque control law, after approximately 30 hours, we see that M oscillates around $2.2m^5$ with the modulation amplitude set at $\Delta M = 0.15m^5$. Now, this -4.3% deviation from M^{opt} would only result in a 0.06% loss

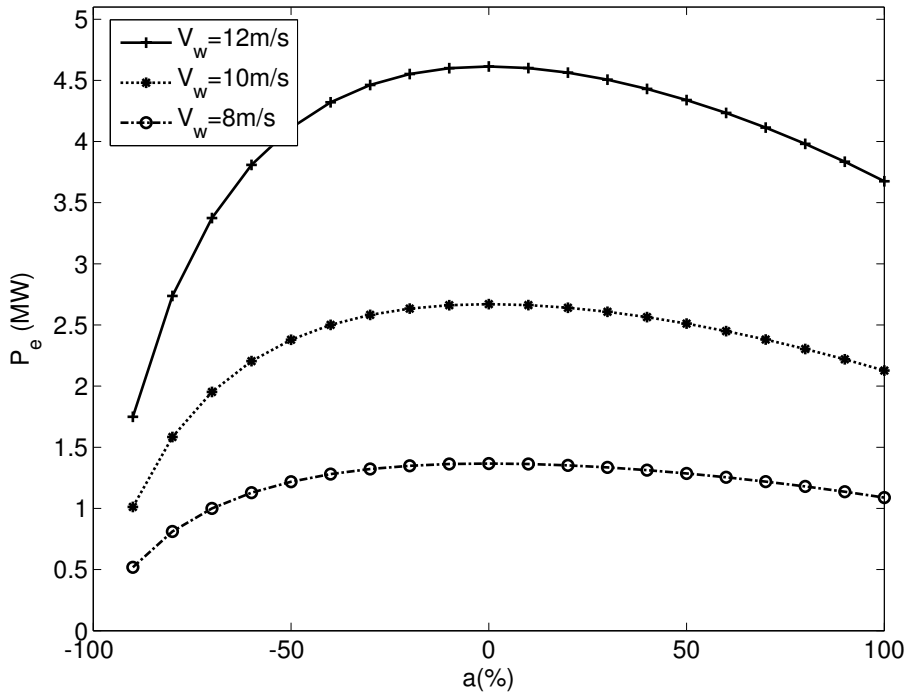

Figure 5.6: The generator power output P_e versus the deviation of M from the optimal gain M^{opt}, for three different wind speeds. Here $a = \frac{M-M^{opt}}{M^{opt}} \cdot 100\%$.

of the electrical power output if the wind speed were equal to the same constant $8m/s$. This is because the plot of the electrical power as a function of M is rather flat, see Figure 5.6. This shows that the adaptive algorithm leads to a high efficiency in wind energy capture. In terms of the influence on the power grid, we can see from Figure 5.8 that the adaptive algorithm does not result in noticeable electrical power oscillations, when compared to the variations due to the random nature of the wind.

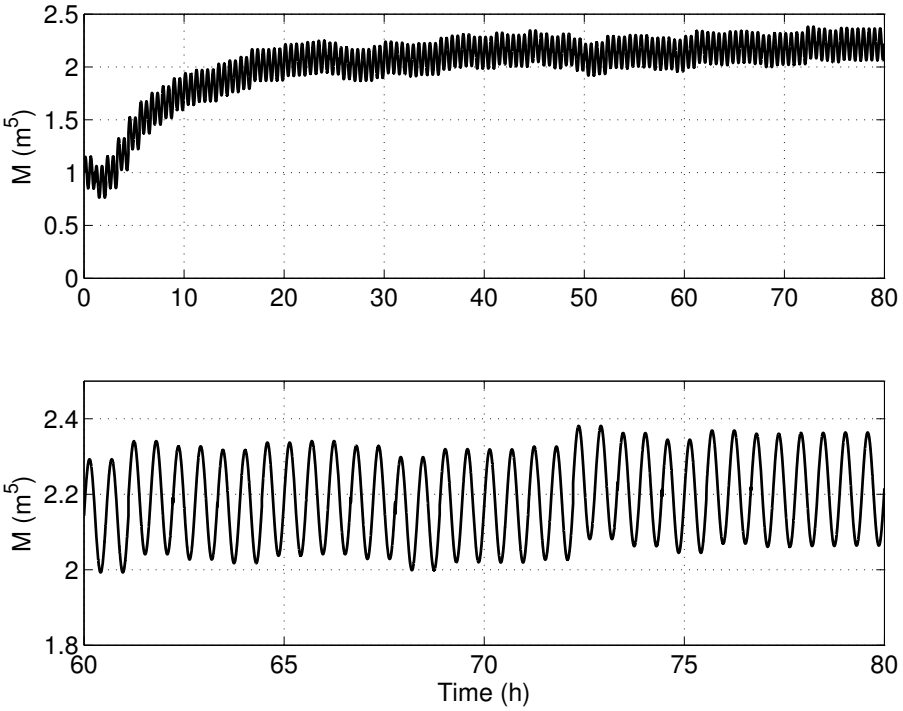

Figure 5.7: The control gain M in the quadratic control law and a zoomed plot. We see that M oscillates around $2.2m^5$ with the modulation amplitude set at $\Delta M = 0.15m^5$. The optimal control gain is $M^{opt} = 2.3m^5$. This -4.3% error in M would result in a 0.06% loss of the electrical power output if the wind speed were constant, equal to its mean value of $8m/s$. This error in M is acceptable from an energy production point of view.

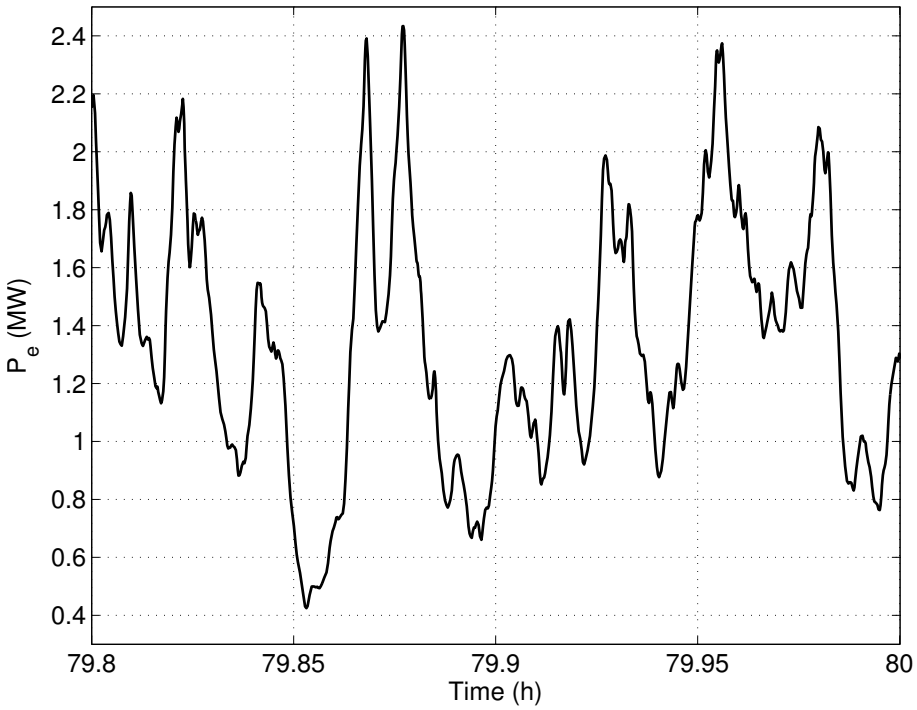

Figure 5.8: The electrical power output with the quadratic torque control law and the adaptation of M, as described in Section 5.4. If we plot the electrical power output with the same random wind speed and with constant $M = M^{opt}$, we get practically the same curve, visually not distinguishable at the scale of the plot. Thus the adaptation algorithm does not result in noticeable electrical power oscillations, when compared to the variations due to the random nature of the wind.

Chapter 6

Conclusions and future works

6.1 Conclusions

In Chapter 3, we propose a two-loop control strategy for a grid-connected wind driven DFIG using LPV technique. In the inner electrical loop containing a DFIG and a rotor-side converter, the LPV control technique has been applied to guarantee quadratic $\mathcal{H}^{\infty}$ performance of the closed-loop system, which represents robust tracking of the rotor current over the entire operating range of the system. The main merits of the LPV control technique are:

- It provides a systematic way of designing controllers for LPV systems, such as DFIG;
- The synthesized controller is given by a simple linear interpolation without the classical interpolation drawbacks;
- The controller is adaptively gain-scheduled using the parameter measurements, so that the plant dynamics are taken into account in real time.
- The online computation of the controller is cheap so that the implementation of the LPV controller using a cheap processor can be an option in industry.

Controller reduction has also been developed based on the truncation of fast modes. The method has significantly reduced the size of the LPV controller's state-dimension.

A frequency support controller has been designed to extract the kinetic energy stored in the turbine blades and contribute to the grid frequency support following loss of network

generation.

In Chapter 4, we have shown that under mild assumptions, a passive nonlinear system which is GAS is also iISS with a very simple (L^1 norm type) integral term. Our main result eliminates the need for finding a Lyapunov function satisfying the estimate (4.1.3) for this class of systems.

In Chapter 5, we have investigated the stability of a variable-speed wind turbine operating in region 2. The closed-loop wind turbine system has been modelled at the mechanical level as a drive-train with the standard quadratic torque controller. We have shown that the turbine system is ISS for the one-mass model and iISS for the two-mass model. This is useful for assessing the robustness of the system with respect to tracking errors of the electrical torque and with respect to small perturbations of the electrical torque introduced in order to identify the optimal control gain of the torque controller.

6.2 Future works

Some possible extensions of the results and techniques presented in this thesis have been identified. They are as follows:

- Future work is required to assess the dynamic performance of the proposed two-loop control strategy in a power network model that combines synchronous and wind farm (WF) generation, see [26, 38] and see Figure 6.1 for such a power network model.

- The frequency support controller proposed in this thesis can be extended to support the secondary frequency control. The idea is that a WF can be controlled to operate with a certain constant reserve capacity in relation to its momentary possible power production capacity. Then the reserved kinetic energy can be released in frequency control action, see [22].

- We aim to develop advanced control strategies for wind turbines that will enable the active suppression of mechanical vibrations of the tower and drive-train, and better grid integration of WFs. The suppression of vibrations would enable lighter, less rigid structures, whereas better grid integration refers to the contribution of WFs

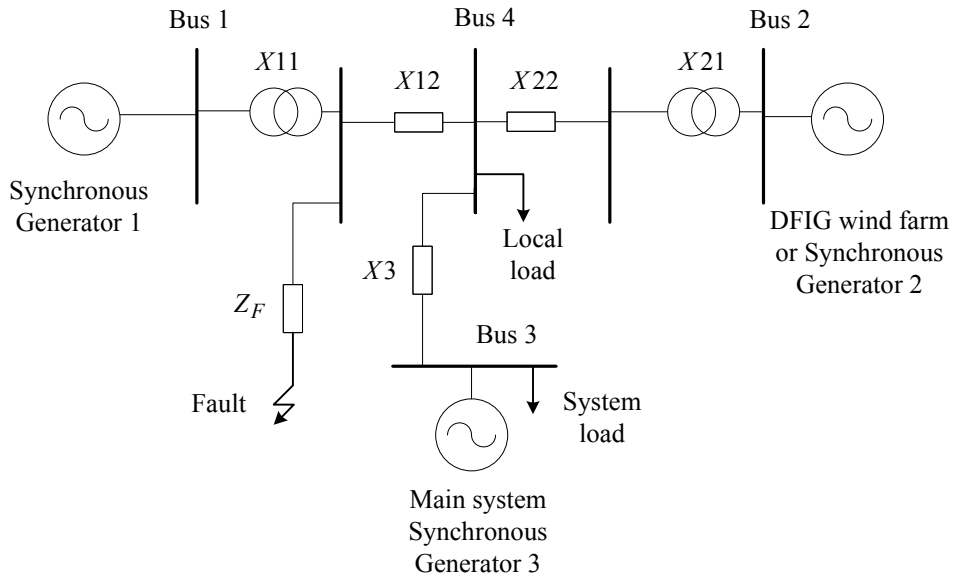

Figure 6.1: Generic network model developed to assess dynamic and transient performances

to voltage support and recovery following network faults, together with improved power system damping to prevent inter-area oscillations. Vibration suppression and grid integration may lead to conflicting requirements, and a proper balance must be sought.

Bibliography

[1] *The Grid Code*. National grid electricity transmission plc. [Online]. Available: http://www.nationalgrid.com.

[2] V. Akhmatov. Variable-speed wind turbines with doubly-fed induction generators. part i: Modelling in dynamic simulation tools. *Wind Energy*, 26(2):85–108, 2002.

[3] D. Angeli, E.D. Sontag, and Y. Wang. A characterization of integral input-to-state stability. *IEEE Trans. on Automatic Control*, 45(6):1082–1097, 2000.

[4] P. Apkarian and R.J. Adams. Advanced gain-scheduling techniques for uncertain sytems. *IEEE Trans. Control Systems Technology*, 6(1):21–32, 1998.

[5] P. Apkarian, P. Gahinet, and G. Becker. Self-scheduled $\mathcal{H}_\infty$ control of linear parameter-varying systems: A design example. *Automatica*, 31:1251–1261, 1995.

[6] S. Bhowmik, R. Spee, and J.H.R. Enslin. Performance optimization for doubly fed wind power generation systems. *IEEE Trans. Ind. Appl.*, 35(4):949–958, 1999.

[7] F.D. Bianchi, R.J. Mantz, and C.F. Christiansen. Gain scheduling control of variable-speed wind energy conversion systems using quasi-LPV models. *Control Engineering Practice*, 13(2):247–255, 2005.

[8] F. Blaabjerg, Z. Chen, and S.B. Kjaer. Power electronics as efficient interface in dispersed power generation systems. *IEEE Trans. Power Electronics*, 19(5):1184–1194, 2004.

[9] E. A. Bossanyi. Wind turbine control for load reduction. *Wind Energy*, 6:229–244, 2003.

[10] T. Burton, D. Sharpe, N. Jenkins, and E. Bossanyi. *Wind Energy Handbook*. John Wiley & Sons Ltd, England, 2001.

[11] BWEA. *Annual Review 2005*. The British Wind Energy Association (BWEA). [Online]. Available: http://www.bwea.com.

[12] C.I. Byrnes, A. Isidori, and J.C. Willems. Passivity, feedback equivalence, and the global stabilization of minimum phase nonlinear systems. *IEEE Trans. Automat. Contr.*, 36(11):1228–1240, 1991.

[13] M. Chilali and P. Gahinet. $\mathcal{H}_\infty$ design with pole placement constraints: an lmi approach. *IEEE Trans. Automatic Control*, 41(3):358–367, 1996.

[14] J.B. Ekanayake, L. Holdsworth, X.G. Wu, and N. Jenkins. Dynamic modeling of doubly-fed induction generator wind turbines. *IEEE Trans. Power Systems*, 18(2):803–809, 2003.

[15] P. Gahinet and P. Apkarian. A linear matrix inequality approach to $\mathcal{H}_\infty$ control. *Int. J. Robust and Nonlinear Control*, 4:421–448, 1994.

[16] P. Gahinet, P. Apkarian, and M. Chilali. Affine parameter-dependent lyapunov functions and real parametric uncertainty. *IEEE Trans. Automatic Control*, 41:436–442, 1996.

[17] GE. $3.6MW$ *offshore series wind turbine brochure*. GE Energy. [Online]. Available: http://www.gewindenergy.com.

[18] K. Glover. All optimal Hankel-norm approximations of linear multivarible sytems and their L^∞-error bounds. *INT. J. Control*, 39(6):1115–1193, 1984.

[19] M. Green and D.J.N. Limebeer. *Linear Robust Control*. Englewood Cliffs, N.J.: Prentice-Hall, 1995.

[20] A.D. Hansen, P. Soerensen, F. Blaabjerg, and J. Becho. Dynamic modeling of wind farm grid interaction. *Wind Engineering*, 26(4):191–208, 2002.

[21] A.D. Hansen, P. Soerensen, F. Iov, and F. Blaabjerg. Control of variable speed wind turbines with doubly-fed induction generators. *Wind Engineering*, 28(4):411–434, 2004.

[22] A.D. Hansen, P. Soerensen, F. Iov, and F. Blaabjerg. Centralised power control of wind farm with doubly-fed induction generators. *Renewable Energy*, 31(7):935–951, 2006.

[23] M.H. Hansen, A. Hansen, T.J. Larsen, S. Seoye, P. Seoensen, and P. Fuglsang. Control design for a pitch-regulated, variable speed wind turbine. Technical report, Riseo National Laboratory, 2005.

[24] S. Heier. *Wind Energy Conversion Systems*. John Wiley and Sons Ltd, Chichester, England, 1998.

[25] D. Hill and P.J. Moylan. The stability of nonlinear dissipative systems. *IEEE Trans. Automat. Contr.*, 21(5):708–711, 1976.

[26] M. Hughes, O. Anaya-Lara, N. Jenkins, and G. Strbac. Control of $DFIG$-based wind generation for power network support. *IEEE Trans. Power Systems*, 20(4):1958–1966, 2005.

[27] I.M. Jaimoukha, H.M.H. El-Zobaidi, D.J.N. Limebeer, and N. Shah. Controller reduction for linear parameter-varying systems with a priori bounds. *Automatica*, 41:273–279, 2005.

[28] Imad M. Jaimoukha. Design of linear multivariable control systems. Lecture Notes, Imperial College London, Department of Electrical and Electronic Engineering, 2003.

[29] B. Jayawardhana, A. R. Teel, and E. P. Ryan. iISS gain of dissipative systems. *The 46th IEEE Conference on Decision and Control*, pages 3835–3840, New Orleans, 2007.

[30] B. Jayawardhana and G. Weiss. LTI internal models for input disturbance regjection for passive nonlinear systems. submitted in 2006.

[31] K.E. Johnson, L.Y. Pao, M.J. Balas, and L.J. Fingersh. Control of variable-speed wind turbines: standard and adaptive techniques for maximizing energy capture. *IEEE Control Systems Magazine*, 26(3):70–81, 2006.

[32] H.K. Khalil. *Nonlinear Systems*. Prentice-Hall. Inc., Upper Saddle River, NJ, third edition, 2000.

[33] T. Krough. $HAWC$ load simulation of generic $5MW$ offshore wind turbine model. Technical report, Riso National Laboratory, Roskilde, 2004.

[34] P. Kundur. *Power System Stability and Control*. McGraw-Hill, 1994.

[35] H. Li, K.L. Shi, and P.G. McLaren. Neural-network-based sensorless maximum wind energy capture with compensated power coefficient. *IEEE Trans. Ind. Appl.*, 41(6):1548–1556, 2005.

[36] Z. Lubosny. *Wind Turbine Operation in Electric Power Systems*. Springer-Verlag, Berlin, 2003.

[37] M.Machmoum, F. Poitiers, C. Darengosse, and A. Queric. Dynamic performances of a doubly-fed induction machine for a variable-speed wind energy generation. *International Conference on Power System Technology, 2002. Proceedings, PowerCon 2002*, 14:2431–2435, 2002.

[38] J. Morren, S. de Haan, W. Kling, and J. Ferreira. Wind turbines emulating inertia and supporting primary frequency control. *IEEE Trans. Power Systems*, 21(1):433–434, 2006.

[39] J. Morren, S.W.H. de Haan, P. Bauer, and J.T.G. Pierik. Comparison of complete and reduced models of a wind turbine with douly-fed induction generator. In *Proc. of the 10th European conference on Power Electronics and applications (EPE)*, Toulouse, Frankrijk, 2003.

[40] P.J. Moylan. Implications of passivity in a class of nonlinear systems. *IEEE Trans. Automat. Contr.*, AC(19):373–381, 1974.

[41] E. Muljadi and C.P. Butterfield. Pitch-controlled variable-speed wind turbine generation. *IEEE Trans. Industry Applications*, 37(1):240–246, 2001.

[42] R. Pena, J.C. Clare, and G.M. Asher. Doubly-fed induction generator using back-to-back pwm converters and its application to variable-speed wind-energy generation. *IEE Proc. Electr. Power Appl.*, 143(3):231–241, 1996.

[43] E. Persson. One-dimensional wind simulation. Technical report, Mathematical Statistics, ChalmersUniversity of Technology, Gothenburg, 1996.

[44] E. Prempain, I. Postlethwaite, and A. Benchaib. A linear parameter variant $\mathcal{H}_\infty$ control design for an induction motor. *Control Engineering Practice*, 10:633–644, 2002.

[45] M. Rasila. Torque and speed control of a pitch regulated wind turbine. Master's thesis, Department of Electric Power Engineering, Chalmers University of Technology, Sweden, 2003.

[46] C. Scherer, P. Gahinet, and M. Chilali. Multiobjective output-feedback control via lmi optimization. *IEEE Trans. Automatic Control*, 42(7):896–911, 1997.

[47] P. Seorensen, A.D. Hansen, T. Lund, and H. Bindner. Reduced models of doubly fed induction generator system for wind turbine simulations. *Wind Energy*, in press.

[48] Y.D. Song, B. Dhinakaran, and X.Y. Bao. Variable speed control a wind turbines using nonlinear and adaptive algorithms. *J. Wing Eng. Ind. Aerodyn.*, 85(3):293–308, 2000.

[49] E.D. Sontag. Smooth stabilization implies coprime factorization. *IEEE Trans. Automat. Contr.*, 34(4):435–443, 1989.

[50] E.D. Sontag. *Mathematical Control Theory: Deterministic Finite Dimensional Systems*. Springer-Verlag, NY, 1990.

[51] E.D. Sontag. Comments on integral variants of ISS. *Syst. Contr. Lett.*, 34:93–100, 1998.

[52] D. A. Spera. *Wind Turbine Technology : Fundamental Concepts of Wind Turbine Engineering*. ASME Press, 1994.

[53] S. Suryanarayanan and A. Dixit. A procedure for the development of control-oriented linear models for horizontal-axis large wind turbines. *Journal of Dynamic Systems, Measurement and Control, ASME*, 129:469–479, 2007.

[54] P. Vas. *Sensorless Vector and Direct Torque Control*. Oxford University Press, 1998.

[55] J.F. Walker and N. Jenkins. *Wind Energy Technology*. John Wiley and Sons Ltd, Chichester, England, 1997.

[56] C. Wang and G. Weiss. The integral input-to-state stability of passive nonlinear systems. *The 46th IEEE Conference on Decision and Control*, pages 3830–3834, New Orleans, 2007.

[57] C. Wang and G. Weiss. Integral input-to-state stability of the drive-train of a wind turbine. *The 46th IEEE Conference on Decision and Control*, pages 6100–6105, New Orleans, 2007.

[58] C. Wang and G. Weiss. Self-scheduled LPV control of a wind driven doubly-fed induction generator. *The 45th IEEE Conference on Decision and Control*, pages 1246–1251, San Diego, 2006.

[59] C. Wang and G. Weiss. The $iISS$ property for passive nonlinear systems. submitted, 2007.

[60] C. Wang and G. Weiss. LPV control of a $DFIG$-based wind turbine with primary grid frequency support. submitted, 2007.

[61] C. Wang and G. Weiss. Stability analysis of the drive-train of a wind turbine with quadratic torque control. submitted, 2007.

[62] J.C. Willems. The generation of Lyapunov function for input-output stable systems. *J. SIAM Contr.*, 9:105–134, 1971.

[63] A.D. Wright and M.J. Balas. Design of controls to attenuate loads in the controls advanced research turbine. *J. of Solar Energy Engineering*, 126:1083–1091, 2004.

[64] K. Zhou, J. Doyle, and K. Glover. *Robust and Optimal Control*. Prentice-Hall International, London, 1996.

Appendix A

Realization of system matrices

A.1 Realization of $\tilde{\mathbf{P}}_j$

Here we derive (3.6.5), the realization of the extended plant for any fixed $\theta = \begin{bmatrix} \omega_s & \omega_r \end{bmatrix}^T$. Denoting $\tilde{A} = A_0 + \omega_s A_1 + \omega_r A_2$, we have from Figure 3.3

$$\begin{aligned}
\tilde{y}_1 &= z = \left[\begin{array}{c|cc} \tilde{A} & B_1 & B_2 \\ \hline C_1 & D_{11} & D_{12} \end{array}\right] \begin{bmatrix} w \\ u \end{bmatrix}, \\
\tilde{y}_2 &= x = \left[\begin{array}{c|cc} \tilde{A} & B_1 & B_2 \\ \hline C_2 & D_{21} & D_{22} \end{array}\right] \begin{bmatrix} w \\ u \end{bmatrix}, \\
\tilde{z}_1 &= W_1 z \\
&= \left[\begin{array}{c|c} A_w & B_w \\ \hline C_w & D_w \end{array}\right] \left[\begin{array}{c|cc} \tilde{A} & B_1 & B_2 \\ \hline C_1 & D_{11} & D_{12} \end{array}\right] \begin{bmatrix} w \\ u \end{bmatrix} \\
&= \left[\begin{array}{cc|cc} \tilde{A} & 0 & B_1 & B_2 \\ B_w C_1 & A_w & B_w D_{11} & B_w D_{12} \\ \hline D_w C_1 & C_w & D_w D_{11} & D_w D_{12} \end{array}\right] \begin{bmatrix} w \\ u \end{bmatrix}, \\
\tilde{z}_2 &= W_u u \\
&= \left[\begin{array}{c|cc} A_u & 0 & B_w \\ \hline C_u & 0 & D_u \end{array}\right] \begin{bmatrix} w \\ u \end{bmatrix}.
\end{aligned}$$

If we combine the above equations, then we obtain (3.6.5).

A.2 Realization of $\mathbf{T}_{zw}$

Here we derive (3.6.6). For any fixed $\theta = \begin{bmatrix} \omega_s & \omega_r \end{bmatrix}^T$, by denoting $\tilde{A} = A_0 + \omega_s A_1 + \omega_r A_2$, we have from Figure 3.3 that $u = \mathbf{C}_K x_K$, where x_K satisfies

$$\dot{x}_K = \mathbf{A}_K x_K + \mathbf{B}_{K1} z + \mathbf{B}_{K2} y.$$

Substituting $u = \mathbf{C}_K x_K$ into (3.5.1), then

$$\begin{aligned} \dot{x} &= \tilde{A}x + B_1 w + B_2 \mathbf{C}_K x_K, \\ z &= C_1 x + D_{11} w + D_{12} \mathbf{C}_K x_K, \\ y &= C_2 x + D_{21} w + D_{22} \mathbf{C}_K x_K. \end{aligned}$$

Furthermore

$$\begin{aligned} \dot{x}_K &= (\mathbf{A}_K + \mathbf{B}_{K1} D_{12} \mathbf{C}_K + \mathbf{B}_{K2} D_{22} \mathbf{C}_K) x_K \\ &\quad + (\mathbf{B}_{K1} C_1 + \mathbf{B}_{K2} C_2) x + (\mathbf{B}_{K1} D_{11} + \mathbf{B}_{K2} D_{21}) w. \end{aligned}$$

Hence, the transfer matrix from w to z for any fixed θ is (3.6.6).

Appendix B

Simulink models

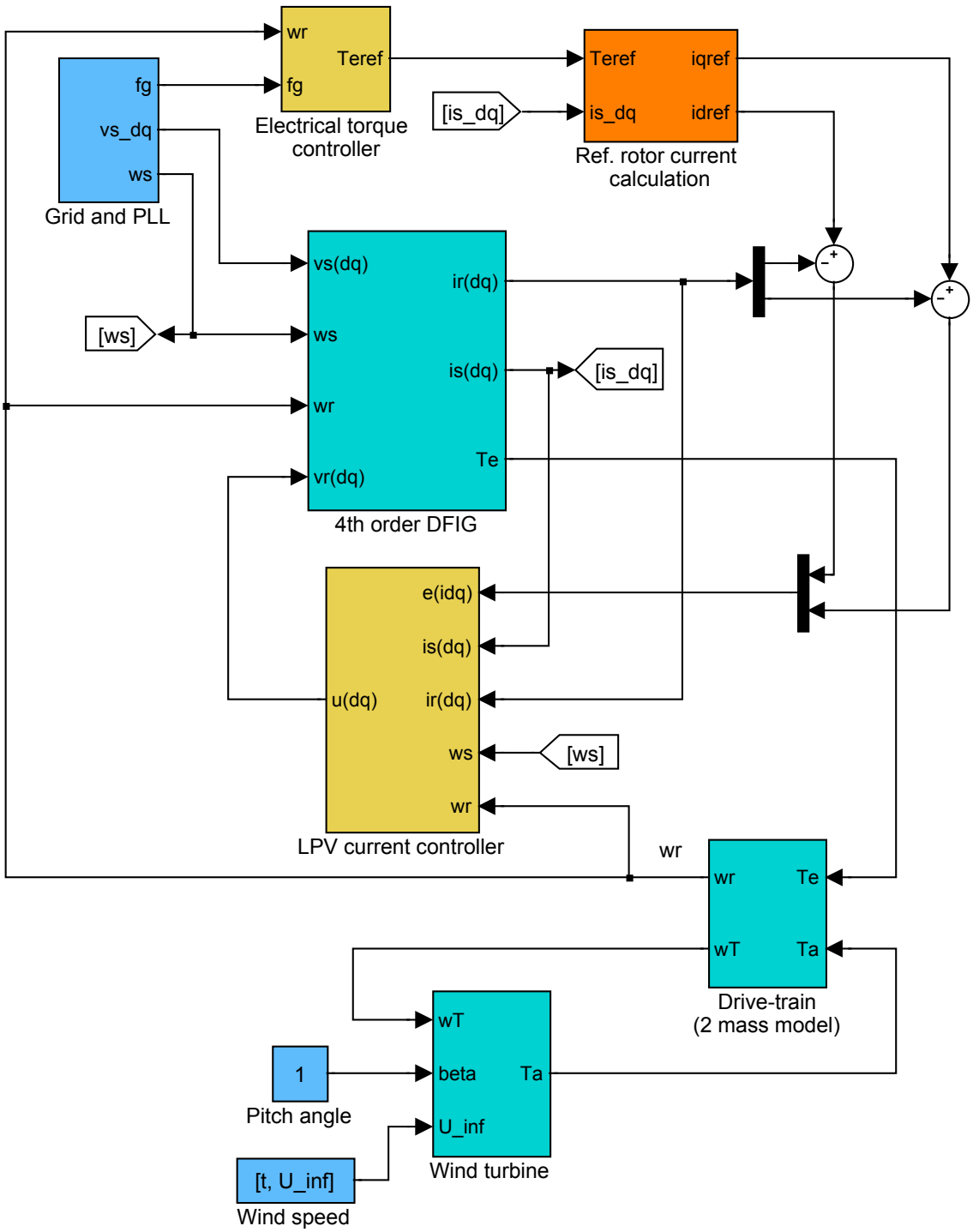

LPV control of a DFIGWT with primary frequency support

Figure B.1: The Simulink implementation of the LPV control of a DFIGWT. The wind turbine block is shown in Figure 2.7. The $4th$ order DFIG block is shown in Figure B.4. The drive-train block is shown in (2.8.2). The grid and PLL block is shown in Figure 3.5. The electrical torque controller block is shown in Figure 3.1. The reference rotor current calculation is shown in (3.6.4). The LPV current controller block is shown in Figure B.2.

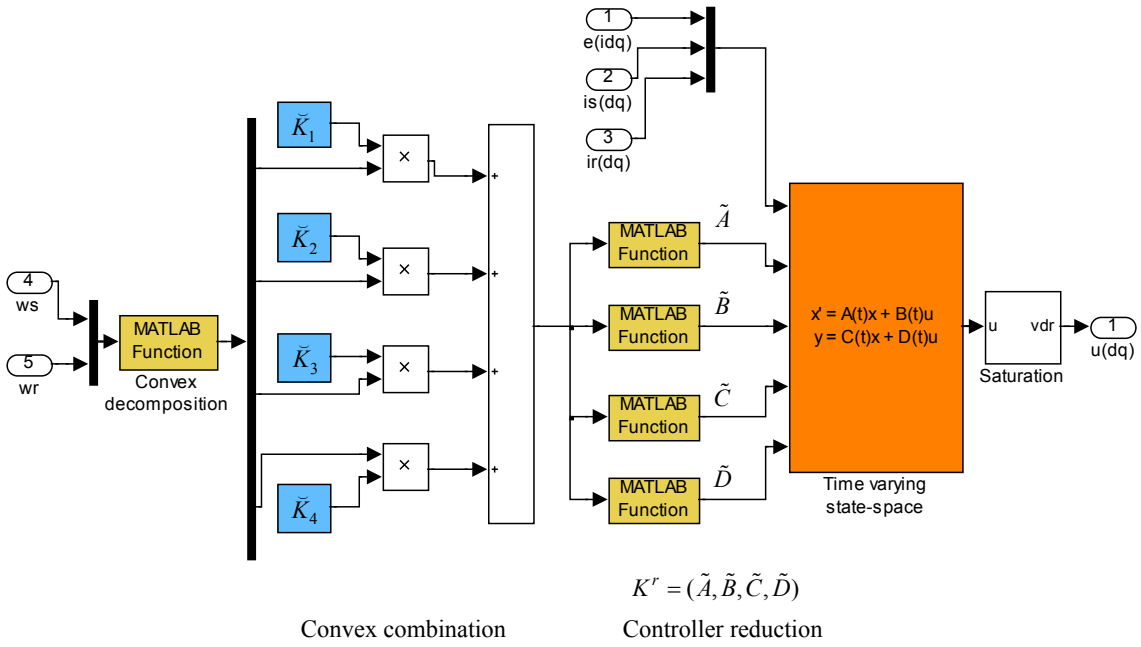

Figure B.2: The Simulink implementation of the LPV controller, including the controller reduction procedure shown in Section 3.4. The vertex controllers $(\breve{K}_1, \breve{K}_2, \breve{K}_3, \breve{K}_4)$ are computed using (3.4.1). The system matrices of the reduced controller $K^r = (\tilde{A}, \tilde{B}, \tilde{C}, \tilde{D})$ are computed using (3.4.3)-(3.4.6). The convex decomposition block is implemented using a Matlab routine: *polydec.m*.

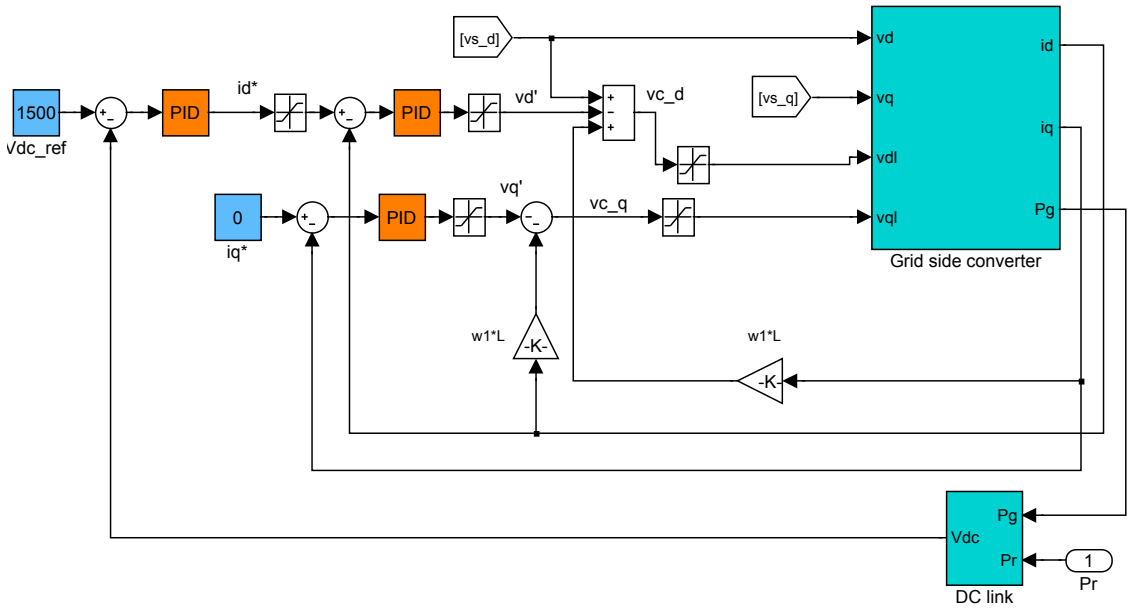

Figure B.3: Vector control of the grid-side converter. The grid side converter block is shown in (2.7.1). The DC-link block is shown in Section 2.7.

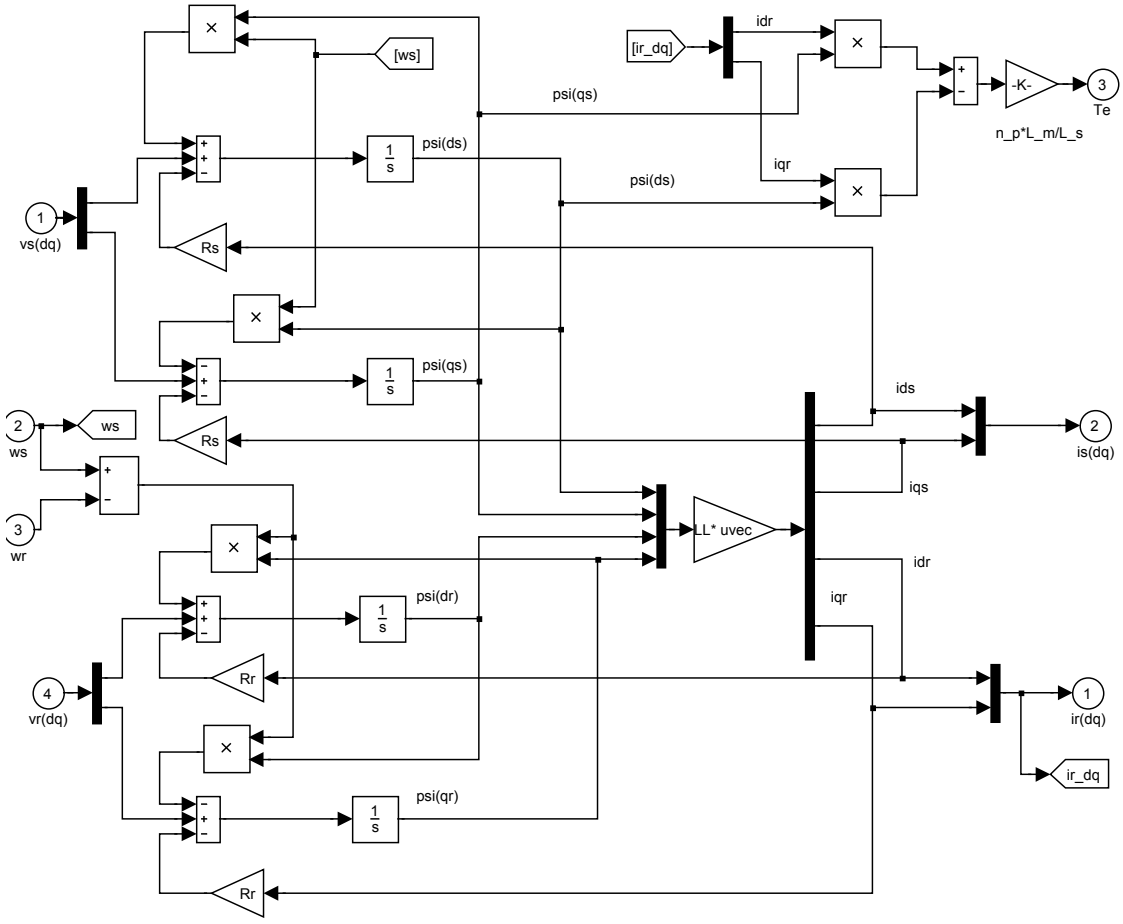

Figure B.4: The Simulink model of the 4^{th} order DFIG.